UNIVERSIDADE DE LISBOA

FACULDADE DE CIÊNCIAS
DEPARTAMENTO DE QUÍMICA E BIOQUÍMICA

Membranes as targets for apoptotic bile acids

JOÃO TIAGO CARVALHO JORDÃO DE MELLO VIEIRA

Dissertação de Mestrado

Mestrado em Bioquímica

2012

UNIVERSIDADE DE LISBOA

FACULDADE DE CIÊNCIAS
DEPARTAMENTO DE QUÍMICA E BIOQUÍMICA

Membranes as targets for apoptotic bile acids

JOÃO TIAGO CARVALHO JORDÃO DE MELLO VIEIRA

Dissertação de Mestrado orientada por

Doutor Fábio Fernandes e Professor Doutor Francisco Pinto

Mestrado em Bioquímica

2012

Agradecimentos

Quero agradecer ao professor Prieto por me ter recebido no seu grupo (Biological Fluorescence Group, CQFM, IST) e por todo o apoio que me deu ao longo deste ano.

Quero agradecer a todos os colegas de laboratório pelo óptimo ambiente de trabalho, em especial à Maria João e à Ana, por todo o apoio, incentivo (leia-se obrigação) e conversa (leia-se distracção). Queria também destacar a prof. Ana Coutinho por ser sempre um pronto-socorro no que tocava às minhas dúvidas.

Este trabalho não seria possível sem as medidas de tempos de vida de fluorescência realizadas pelo Alexander, спасибо, sem as medidas de ITC do Marco Domingues (Biomembranes Group, IMM), obrigado, e sem a síntese dos ácidos biliares derivatizados por S.D. Lucas, R. Moreira, R.E. Castro, C.M.P. Rodrigues (iMed, FFUL), obrigado.

Agradeço à FCT pelo apoio financeiro nos projectos "Relationship between PI(4,5)P2 compartmentalisation and palmitoylated synaptic proteins in membrane model systems and in the plasma membrane of neuron and non-neuron like cells" (PTDC/QUIBIQ/112067/2009) e "Interaction of bile acids with lipid membranes: creating a shield or bursting a bubble" (PTDC/QUI-BIQ/119494/2010).

Não podia deixar de agradecer à Isabel, pela paciência para esperar por mim, destreza para trocar planos à última hora, pela confiança que me restaurava e por me ter apoiado incansavelmente durante este ano. Quero agradecer a todos os meus amigos, por em todas as saídas terem interesse e paciência para me ouvirem a falar meu trabalho. Queria também agradecer à minha família, por nunca duvidarem de mim e das minhas escolhas e me ajudarem sempre em tudo.

Quero agradecer a todos os contribuíram de algum modo a completar este trabalho mas que não foram referidos acima por lapso.

Por último e igualmente importante, obrigado Dr. Fábio Fernandes por ter sido o meu orientador e me ter apoiado, ouvido, corrigido, ensinado, voltado a corrigir, motivado, voltado a ensinar durante este longo mas frutífero ano.

Table of Contents

Agradecimentos i
Resumo v
Summary ix
List of Abbreviations xi
List of Symbols xiii
1. Introduction 1
1.1. Bile acid function, synthesis and chemistry 3
1.2. Bile acid aggregation 6
1.3. Bile acids and apoptosis 8
1.4. Bile acid interaction with lipid membranes 12
1.5. Bile acid as putative modulators of membrane properties and cell signalling 13
2. Materials and methods 15
2.1. Chemicals 17
2.1.1. Reagents 17
2.1.2. Probes 19
2.1.3. Cell culture 19
2.2. Model membrane system preparation 19
2.2.1. Large Unilamellar vesicles (LUVs) 19
2.2.2. Giant Unilamellar vesicles (GUVs) 20
2.2.3. Lipid quantification 20
2.3. Cell membrane labelling and BA incubation 21
2.4. Absorption and fluorescence measurements 21
2.4.1. UV-Vis absorption spectroscopy 21
2.4.2. Steady-state fluorescence spectroscopy 21
2.4.3. Transient-state fluorescence spectroscopy 22
2.4.3.1. Fluorescence decay analysis 23
2.4.4. Partition coefficient determination 25
2.4.5. FRET studies 26
2.5. Confocal fluorescence microscopy 27
2.5.1. Fluorescence lifetime imaging microscopy 28
2.6. Isothermal titration calorimetry (ITC) 28
3. Results 31

3.1. Bile Acid aggregation 33
3.1.1. Critical Micellar Concentration determination 34
3.1.2. Critical Aggregation Concentration 40
3.1.3. DCA-NBD interacts with unlabelled BA 43
3.2. Labelled bile acids and membranes 49
3.2.1. Labelled BA partition 49
3.2.2. The effect of hydrophilic bile acid on DCA-NBD partition 58
3.3. Unlabelled bile acids and labelled-liposomes 60
3.3.1. Bile acid location on model membrane systems 60
3.3.2. The effect of Chol on bile acids 66
3.4. Bile acid effect on live HEK293 cells 76
4. Discussion 79
5. References 85

Resumo

Ácidos biliares (ABs) são derivados do colesterol sintetizados no fígado, cuja função é solubilizar lípidos durante a digestão. Este grupo é composto por vários moléculas que variam no número e posições dos grupos hidroxilo e no seu grupo terminal. Os ácidos biliares são caracterizados consoante a sua hidrofobicidade.

Os ABs hidrófobos (como o ácido deoxicólico, DCA) são activadores de apoptose tanto por via extrínseca, induzindo a activação de receptores de morte, como por via intrínseca, promovendo a libertação de factores pro-apoptóticos dos mitocôndrios. Por outro lado, os ABs hidrófilos (como os ácidos ursodeoxicólico, UDCA, e tauroursodeoxicólico, TUDCA) são inibidores da apoptose, inibindo os eventos acima descritos. No entanto, o mecanismo através do qual os ABs induzem respostas antagónicas ainda não está elucidado. Neste trabalho é posta a hipótese que a membranas celulares constituem o alvo principal na sinalização pró-apoptótica. Adicionalmente, o trabalho segue também três linhas de investigação que tentam esclarecer qual o efeito citoprotector dos ABs hidrófilos:

1) os ABs hidrófilos e hidrófobos interactuam em solução dando origem a um agregado misto que é inócuo para as células;
2) os ABs hidrófilos impedem a partição e interacção dos ABs hidrófobos com membranas;
3) os ABs hidrófilos alteram a dinâmica das membranas celulares impedindo ou revertendo possíveis alterações induzidas por ABs hidrófobos.

Foram utilizados os ABs DCA, UDCA e TUDCA, bem como dois ABs derivados com o grupo fluorescente nitro-2-1,3-benzoxadiazol-4yl (NBD), DCA-NBD e UDCA-NBD.

Em primeiro lugar e com o objectivo de testar o comportamento dos derivados de ABs, a concentração micelar crítica dos ácidos biliares não marcados foi determinada usando como sondas os ABs derivatizados ou Nile Red, uma sonda hidrófoba. Observou-se que tanto os derivados de ABs como o Nile Red detectavam micelas de ABs de forma semelhante. No entanto, a formação de micelas de ABs foi detectada a concentrações mais baixas quando os ABs derivatizados foram utilizados. Isto indica que os ABs derivatizados têm maior afinidade para micelas de AB que outras sondas hidrófobas.

De seguida, o comportamento dos ABs derivatizados foi estudado em solução aquosa. Foi observado que os dois derivados de fluorescentes agregavam em solução aquosa a concentrações superiores a 2 μM. Provou-se que esta agregação é induzida pelo grupo NBD, o que indica que a derivatização, ao retirar à molécula um grupo carregado negativamente, induz agregação. Ainda assim, foi observado que ABs hidrófilos (não marcados) interagem com DCA-NBD na gama de concentrações em que estas moléculas apresentam um efeito citoprotector. Utilizando um modelo matemático, foram ajustadas constantes de agregação aos dados de fluorescência em função da concentração de DCA-NBD na presença e na ausência de ABs

hidrófilos. O modelo recuperou uma constante de agregação de DCA-NBD com ABs hidrófilos na ordem dos 0.002-0.004 μM^{-1}. Estes valores indicam uma interacção muito fraca entre DCA-NBD e UDCA ou TUDCA. Tendo em conta que o DCA-NBD é mais susceptível à formação de agregados que o DCA, podemos concluir que o efeito citoprotector dos ABs hidrófilos não se deve à formação de um complexo inerte hidrófilo/hidrófobo em solução.

A partição dos derivados de ABs para membranas modelo foi também estudada. Para isso foram utilizados dois tipos de vesículas compostas apenas por POPC ou por POPC, colesterol e PSM. Notou-se que tanto DCA-NBD como UDCA-NBD particionavam de forma análoga para vesículas constituídas apenas por POPC e que particionavam com menor eficácia para vesículas contendo uma mistura de POPC, colesterol e PSM (mistura lipídica com coexistência de fases liquido ordenadas, I_o, e desordenadas, I_d). A partição de UDCA-NBD e DCA-NBD foi dramaticamente afectada pela presença de fases ordenadas. Devido à interacção detectada entre DCA-NBD e ABs hidrófilos, a partição do DCA-NBD para vesículas de POPC foi de novo analisada após incubar as vesículas com elevadas concentrações de ABs hidrófilos. Foi observado que a partição do DCA-NBD não era alterada pela presença de ABs hidrófilos.

O efeito de ABs não marcados nas propriedades biofísicas de sistemas modelo de membranas foi também estudado. Neste conjunto de experiências, várias sondas de membrana foram incorporadas nas vesículas, cada uma monitorizando uma propriedade biofísica diferente, desde fluidez de diferentes regiões ao potencial de membrana. Foi observado que a sonda DPH era insensível à presença de ABs mas que a sonda ANEPPDHQ aumentava o seu rendimento quântico na presença destas moléculas. Sendo o DPH (uma sonda de fluidez do interior da membrana) insensível aos ABS e o ANEPPDHQ (uma sonda mais superficial) sensível aos ABs, conclui-se que a possível localização dos ácidos biliares é à superfície da membrana.

Por outro lado, foi observado que o aumento a concentração de colesterol nas membranas não era acompanhado pelo aumento de rigidez na presença de DCA. No entanto, o efeito medido não era inibido por ABs hidrofílos. Foi provado que este efeito não era devido à remoção de colesterol por DCA, pois a sonda dehidroergosterol, um análogo fluorescente do colesterol, não era removido das vesículas pelo AB. Conclui-se portanto que o DCA em concentrações submicelares elimina parcialmente a capacidade do colesterol de rigidificar membranas. Este efeito não é observado em fase I_o. Adicionalmente, foi observado um aumento considerável da área superficial de membranas após incubação com DCA. A exposição de membranas biológicas ao DCA poderá assim resultar numa alteração significativa das suas propriedades biofísicas.

Finalmente, células HEK293 foram incubadas com DCA ou TUDCA ou uma combinação dos dois ABs. As células, marcadas anteriormente com ANEPPDHQ, foram analisadas por FLIM de modo a estudar o efeito dos ABs *in vivo*. Foi observado que o tempo de vida da sonda ANEPPDHQ diminuía após incubação com os ABs. Estes resultados diferem dos obtidos em

sistemas modelo, em que era observado um aumento no tempo de vida desta sonda. Esta discrepância pode ser explicada pela presença de diferentes membranas, com diferentes composições num sistema vivo, ou por um efeito da activação da via apoptótica nas células. É possível que os ABs tenham efeitos diferentes em membranas com composições diferentes, o que explicaria a discrepância observada.

Concluindo, neste estudo foi observado que DCA-NBD e UDCA-NBD agregam em solução aquosa e que particionam de forma semelhante e preferencial para fases l_d. A partição de DCA-NBD não é afectada por ABs hidrófilos. Através de estudos utilizando sondas de membrana, concluiu-se que a posição de ABs em membranas é possivelmente superficial. A observação de que o DCA elimina parcialmente a capacidade do colesterol de rigidificar membranas, foi de particular importância para a elucidação do mecanismo apoptótico destas moléculas. Este poderá assim estar relacionado com uma alteração na organização dos componentes da membrana plasmática, nomeadamente a nível da formação/composição de jangadas lipídicas. Por último, o efeito dos ABs em células foi estudado e é aparentemente diferente do observado em sistemas modelo, indicando que em células vidas, a eliminação parcial do efeito rigidificante do colesterol não é o único efeito na estrutura de membranas biológicas resultante da incubação com ácidos biliares hidrófobos.

Palavras-chave: Espectroscopia de fluorescência, Sistemas modelo de membranas, Apoptose, Jangadas lipídicas, Colesterol

Summary

Bile acids (BAs) are cholesterol derivates synthetized in the liver of humans. Hydrophobic bile acids (BAs) such as deoxycholic acid (DCA) induce cell death via multiple pathways, including the extrinsic pathway of apoptosis, dependent on pro-apoptotic receptor activation in the plasma membrane, and the intrinsic pathway of apoptosis, involving the release of pro-apoptotic factors from mitochondria. In turn, it has been shown that hydrophilic BAs, particularly ursodeoxycholic (UDCA) and tauroursodeoxycholic (TUDCA) acids significantly inhibit most of these events, thereby preventing apoptosis. Still, the mechanisms by which BAs trigger such opposite signaling effects remain unclear. We hypothesize that cellular membranes may constitute a determinant primary target for the modulatory effects of BAs during apoptosis.

In this work, two nitro-2-1,3-benzoxadiazol-4yl (NBD) fluorescent derivatives of DCA and UDCA, namely DCA-NBD and UDCA-NBD were studied. Both DCA-NBD and UDCA-NBD interacted with micellar and pre-micellar aggregates of the unlabeled molecules. Interestingly, unlabeled hydrophilic BAs UDCA and TUDCA interacted weakly with DCA-NBD at pre-micellar concentrations.

In addition, both probes partitioned effectively and in similar extent to model membranes (POPC liposomes) and were sensitive to the presence of cholesterol in the membrane. Although UDCA and TUDCA interacted with DCA-NBD, these interactions did not change DCA-NBD partition properties.

Unlabeled BAs DCA, UDCA and TUDCA were shown to induce changes in the fluorescence properties of superficially-located membrane probes, which indicate a superficial but strong interaction with membranes. Lastly, DCA limited to some extent the rigidifying effect of cholesterol on the lipid membrane. This effect could not be abrogated by hydrophilic BAs and might correlate with the apoptotic effect of hydrophilic BAs on cells.

Lastly, FLIM was performed on ANEPPDHQ-labeled HEK293 cells with different results than in membrane model systems, suggesting that effects on biological membranes are not limited to the inhibition of the cholesterol rigidifying effect.

Keywords: Fluorescence spectroscopy, Model Membrane systems, Apoptosis, Lipid Rafts, Cholesterol

List of Abbreviations

ANEPPDHQ – 1-[2-Hydroxy-3-(N,N-di-methyl-N-hydroxyethyl)ammoniopropyl]-4-[β-[2-(di-n-butylamino)-6-napthyl] vinyl]pyridinium dibromide

Akt – Protein Kinase B

Apaf-1 – Apoptotic Protease Activating Factor 1

BA – Bile Acid

Bax – Bcl-2-associated X Protein

Bcl-2 – B-cell lymphoma 2

CA – Cholic Acid

CDCA – Chenodeoxycholic Acid

Chol – Cholesterol

CMC – Critical Micellar Concentration

DCA – Deoxycholic Acid

DHE - Dehydroergosterol

DMEM – Dulbecco's Modified Eagle Medium

DPH – 1,6-Diphenyl-1,3,5-Hexatriene

DPPE-biotin – 1,2-dipalmitoyl-*sn*-glycero-3-phosphoethanolamine-*N*-biotinyl

FLIM – Fluorescence Lifetime Imaging Microscopy

FRET – Förster Resonance Energy Transfer

GCA – Glicocholic Acid

GCDCA – Glicochenodeoxycholic Acid

GDCA – Glicodeoxycholic Acid

GUDCA – Glicoursodeoxycholic Acid

GUV – Giant Unilamellar Vesicle

HEK293 – Human embryonic kidney cell 293

HPLC – High-Performance Liquid Chromatography

List of Abbreviations

ITC – Isothermal Titration Calorimetry

LCA – Lithocholic Acid

l_d – liquid disordered

l_o – liquid ordered

LUV – Large Unilamellar Vesicle

MAP – Mitogen-Activated Protein

MAPKKK – MAP Kinase Kinase Kinase

N_{agg} – Aggregation number

NF-kB –Nuclear Factor Kappa B

NBD – nitro-2-1,3-benzoxadiazol-4yl

NBD-DPPE – 1,2-dipalmitoyl-*sn*-glycero-3phosphoethanolamine-N-(7-nitro-2-1,3-benzoxadiazol-4yl)

OH – Hydroxyl group

PI3K – Phosphoinositide 3 Kinase

POPC – 1-palmitoyl-2-oleoyl-*sn*-glicero-3-phosphocholine

PSM – *N*-palmitoyl-*D*-erythro-sphingosylphosphorylcholine

Rho-DOPE – 1,2-dioleoyl-*sn*-glycero-3-phosphoethanolamine-*N*-(lissamine rhodamine B sulfonyl)

TCSPT – Time-Correlated Single-Photon Timing

TMA-DPH - 1-(4-Trimethylammoniumphenyl)-6-Phenyl-1,3,5-Hexatriene *p*-Toluenesulfonate

TCA – Taurocholic Acid

TCDCA – Taurochenodeoxycholic Acid

TDCA – Taurodeoxycholic Acid

TUDCA – Tauroursodeoxycholic Acid

UDCA – Ursodeoxycholic Acid

List of Symbols

ε – Extinction coefficient

λ – Wavelength

I_{i} – Fluorescence intensity of i

Abs – Absorbance

$< r >$ - Steady-state fluorescence anisotropy

G – G factor

$I_{\mathrm{i,j}}$ – Fluorescence intensity of component with i excitation and j emission relative to emission axis

r_0 – Anisotropy at time = 0 ns

$< \tau >$ - Mean Fluorescence Lifetime

θ – Rotation diffusion coefficient

$I(t)$ – Fluorescence intensity at time = t ns

I_0 – Fluorescence intensity at time = 0 ns

$\bar{\tau}$ – Lifetime-weighted quantum yield

α_{i} – Pre-exponential factor of component i

$r(t)$ – Fluorescence anisotropy at time=t ns

β_{i} – Initial anisotropy of component i

r_0 – Limiting anisotropy

γ_{i} – Molar volume of i

$[L]$ – Lipid concentration

K_{P} – Partition coefficient

E – FRET efficiency

R_0 – Föster Radius

r – Distance between donor and acceptor molecules

ϕ_{i} – Quantum yield of i

n – Refraction index

κ – Orientational factor

J – Overlap integral between donor emission and acceptor excitation spectra

ρ_{FRET} – FRET contribution on donor decay

σ_{A} – Acceptor density

l – Distantce between plane of donor and acceptor

q_{i} – Heat of titration step i

ΔH – Molar partition enthalpy

$n_{\mathrm{j}}^{\mathrm{i}}$ – Moles of j in titration step i

V_{i} – Volume injected in titration step i

V_{cell} – Volume in cell

q_{dil} – Dilution heat

1. Introduction

1.1.Bile acid function, synthesis and chemistry

Bile acids (BAs) are natural-occurring detergents that solubilize dietary lipids in the intestinal tract and in bile [1]. They are a group of amphipathic molecules and the main product of cholesterol (Chol) metabolism of humans and other vertebrates [2].

The BA group encompasses a great variety of molecules ranging from C27 bile alcohols to C27 bile acids and C24 bile acids [2]. This variety can be explained by the evolution of multiple metabolic pathways that serve to convert Chol, a poorly soluble lipid, to water-soluble, amphipathic molecules [2]. It is accepted that the end products of bile acid synthesis in lower vertebrates are the precursors of end products of bile salt biosynthesis in higher vertebrates [3]. Humans only possess C24 bile acids, the farthest from Chol within the metabolic pathway.

Function

BAs are synthesized in the liver and flow from it, through the bile ducts, into the gallbladder where they are stored along with bilirubin, phospholipids, etc. After a meal, gallbladder is

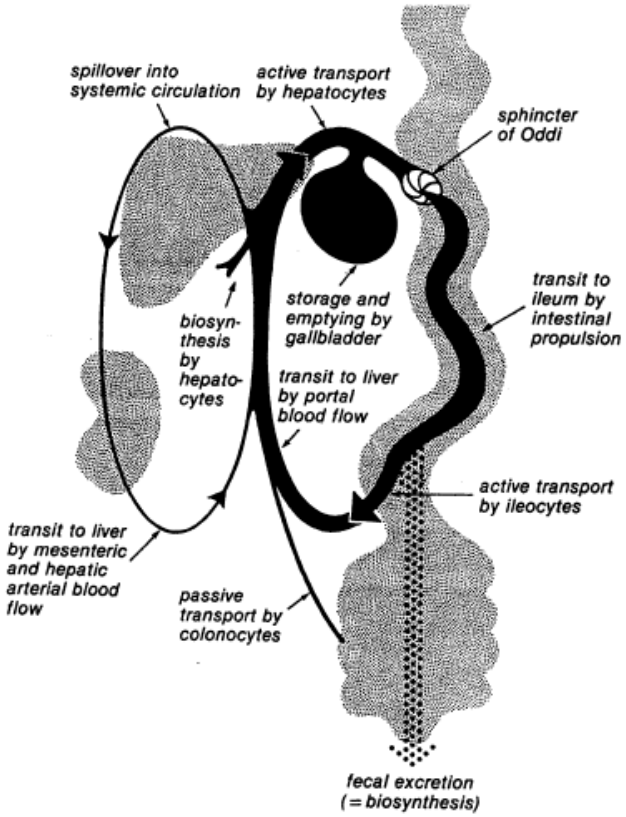

Figure 1-1 - Enterohepatic circulation of bile acids. After being synthesized by hepatocytes, bile acids flow to the gallbladder to be stored. After a meal, the gallbladder is emptied and BAs reach the small intestine, through the Sphincter of Oddi. BAs transit through the small intestine, are absorbed again in the terminal ileum as mixed micelles with fatty acids, phospholipids and cholesterol, and move through the portal vein to the liver were they are mostly recovered. There is some BA spill over onto systemic circulation. Adapted from [2]

emptied and BAs are released in the small intestine at millimolar concentrations. In these conditions BAs aggregate and form mixed micelles with other fats, such as Chol, fatty acids, phospholipids, etc. These aggregates are then absorbed in the small intestine ileum and travel back to the liver through the portal vein. In the liver, BAs are recovered from mixed micelles and the cycle starts again. This process is called enterohepatic circulation (Figure 1-1) [2,4,5].

Synthesis

In humans, BAs synthesized from Chol in the liver are named primary. These are chenodeoxycholic acid (CDCA, Figure 1-2) and cholic acid (CA) [2]. During entherohepatic cycling, primary BAs are exposed to intestinal bacteria enzymes that modify them (e.g., the hydroxyl groups can be epimerized, oxidized or removed) to produce secondary BAs, such as deoxycholic acid (DCA) and lithocholic acid (LCA) [2]. DCA and LCA are the dehydroxylation products of CA and CDCA, respectively [5]. Secondary bile acids can be transformed again by bacteria or by hepatocytes to yield tertiary BAs, as ursodeoxycholic acid (UDCA) [5]. Any BA can be conjugated with taurine or glycine amino acids to yield even more soluble molecules [5]. For example, UDCA can be conjugated with taurine to produce tauroursodexycholic acid (TUDCA). Moreover, BAs interact with nuclear receptors and modulate signalling cascades directly adjusting their own synthesis, uptake and secretion to the body's needs [5].

Most BAs in human bile are conjugated with either glycine or taurine (2:1 ratio) and the quantitative balance is typically 13 CDCA: 12 CA: 7 DCA: 1 UDCA [6]. Human BA pool is an ever-changing environment, depending on diet, lifestyle, age, daytime, etc. [2,3,5].

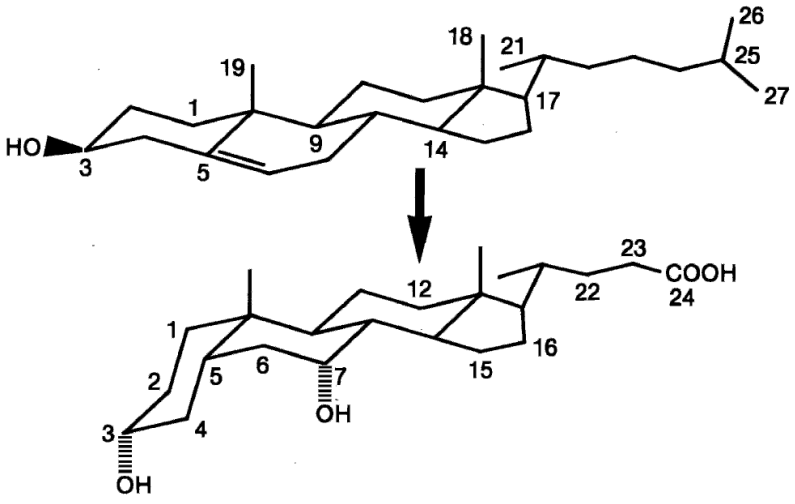

Figure 1-2 - Chemical structure of cholesterol (top) and CDCA, the root C24 bile acid (bottom). Major changes are epimerization of C3, reduction of the double bond between C5 and C6, C7 hydroxylation, beta-oxidation of 8-carbon side chain to a 5-carbon chain. Adapted from [2]

Chemistry

BA structure is based on the tetracyclic steroid ring system, inherited from Chol. Attached to the ring are hydroxyl (-OH) groups that confer an amphipathic character to the molecule. Human BAs differ in number and position of hydroxyl groups as well as in the conjugated amino acid (Figure 1-3, Table 1-1).

They are biologically detergent-like molecules because of their amphipathic nature, possessing both hydrophobic and hydrophilic regions (Figure 1-3) [2]. The most used classification of BA is their hydrophobicity, which is directly related to the number and position of -OH groups [1]. This was derived by reverse-phase High-Performance Liquid Chromatography (HPLC) capacity factor, i.e. partition between the octanol stationary phase and an aqueous mobile phase [7]. Hydrophobicity followed the sequence DCA>CDCA>CA>UDCA, being DCA the most hydrophobic and UDCA the most hydrophilic [1]. Conjugation reduces hydrophobicity but the *relative hydrophobicity order* was the same [1].

As carboxylic acids, most bile acids have a pK_a of 5, meaning their carboxyl group will be deprotonated at physiological pH since intestinal pH is around 7 [3]. Taurine conjugation adds a sulphide group that lowers the molecules pK_a to ≈1 while glycine conjugation lowers pK_a to ≈3, improving both acidity and solubilisation ability [3] as BAs are better emulsifiers in their salt form [5].

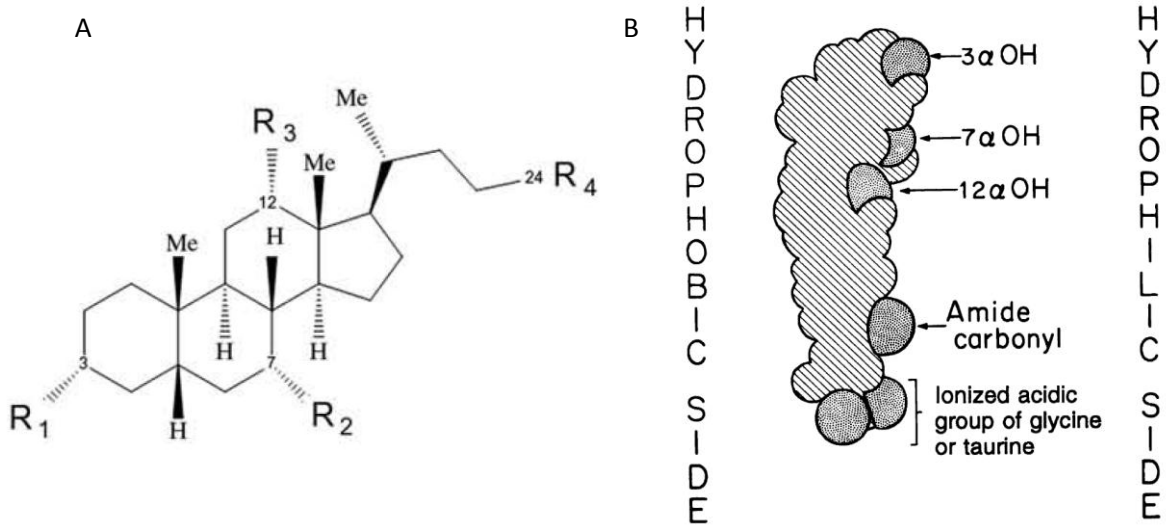

Figure 1-3 – (A) Chemical structure of typical bile acids. R_1-R_3 can be either -OH or -H. R4 can be carboxylic acid, taurine or glycine aminoacids. (B) Space filling model of a typical conjugated bile salts contrasting the 3 hydroxyl groups. The molecule possesses both hydrophobic (left) and hydrophilic (right) sides. Adapted from [2,8]

Table 1-1 - Chemical composition of several bile acids according to Figure 1-3

Bile acid name	Abbrev.	R1	R2	R3	R4
Cholic	CA	OH	OH	OH	COOH
Deoxycholic	DCA	OH	H	OH	COOH
Chenodeoxycholic	CDCA	OH	OH	H	COOH
Ursodeoxycholic	UDCA	OH	OH (epimerized)	H	COOH
Lithocholic	LCA	OH	H	H	COOH
Glicocholic	GCA	OH	OH	OH	$CONHCH_2COOH$
Taurocholic	TCA	OH	OH	OH	$NHCH_2CH_2SO_3H$
Glicodeoxycholic	GDCA	OH	H	OH	$CONHCH_2COOH$
Taurodeoxycholic	TDCA	OH	H	OH	$NHCH_2CH_2SO_3H$
Glicochenodeoxycholic	GCDCA	OH	OH	H	$CONHCH_2COOH$
Taurochenodeoxycholic	TCDCA	OH	OH	H	$NHCH_2CH_2SO_3H$
Glicoursodeoxycholic	GUDCA	OH	OH (epimerized)	H	$CONHCH_2COOH$
Tauroursodeoxycholic	TUDCA	OH	OH (epimerized)	H	$NHCH_2CH_2SO_3H$

1.2.Bile acid aggregation

Bile acids were the subject of extensive study in the 70s and 80s due to the discovery of anti-inflammatory steroid cortisone. Most were readily synthesized by the end of the 70s and their chemical properties were studied in numerous papers. The goal was to connect each chemical structure to a physico-chemical behavioural difference (BA history reviewed in [3]).

BA do not aggregate as typical amphiphiles

Classic amphiphiles have a clear separation between hydrophobic and hydrophilic domains and aggregates are normally associated so that the hydrophobic part is protected from water inside the aggregate, leaving the hydrophilic structure to interact with water [8]. Conversely, BAs have a facial structure with a rigid steroid ring separating the hydrophobic and hydrophilic sides (Figure 1-3) [8]. Also, the presence of hydroxyl and acidic groups allows for the formation of intermolecular hydrogen bonds [8]. Furthermore, the presence of an ionized side chain leads to repulsive interactions between BAs [8]. As consequence of their molecular structure, BA aggregation in aqueous solutions is quite different from classic amphiphiles because it is driven by *both* the hydrophobic effect and intermolecular hydrogen bonding [8]. Hence, BA aggregation and is dependent on the molecular structure of the BA.

BA aggregation models

BA aggregation is temperature, pH and ionic strength dependent [6,9–13]. Likewise, the more hydrophobic the BA is, the greater the tendency it has to aggregate [9]. Furthermore, conjugated BAs aggregate more easily than unconjugated BAs [6,11].

When studying the aggregation pattern of amphiphiles, the most important parameter is the critical micellar concentration (CMC), which is the concentration at which a solute molecules start to form micelles [8]. However, for BAs the CMC is not a clear value, depending on detection method [13].

In the 1979s, Small devised a model to describe BA aggregation [14] (Figure 1-4A). He postulated that BAs exist in aqueous solution in three species, *monomer*, *primary micelles* and *secondary micelles*. After reaching a certain concentration, CMC1, *monomers*, aggregate as a consequence of the hydrophobic effect to form *primary micelles*, which were detectable by light-scattering. BAs in *primary micelles* aggregate with their hydrophobic face turned to the centre of the aggregate and their hydrophilic side to the outside. Increasing the concentration of BA to the CMC2 value, these *primary micelles* polymerized due to hydrogen bonding leading to a "string-of-pearls aggregate", the *secondary micelle*.

Small proposed that the hydrophobic effect is the sole force behind aggregation at low BA concentration [14]. This model is generally accepted for bile acids aggregation and several papers describe bile acid aggregation using a two-phase model [6,10,11,15]. Nevertheless, controversy has risen due to the crystallization of a DCA *helical micelle* which had all hydrophobic faces turned outward, facing the solvent, and the polar groups facing the inside, resembling an inverted micelle [16] (Figure 1-4B). The thermodynamic rational for this inverted micelle is that the hydrogen bonding in the centre of the aggregate outweighs the hydrophobic effect [17]. While these two models dispute micellar structures, the idea that *only one* model is able to explain the aggregation behaviour of *every* BA is perhaps excessively ambitious.

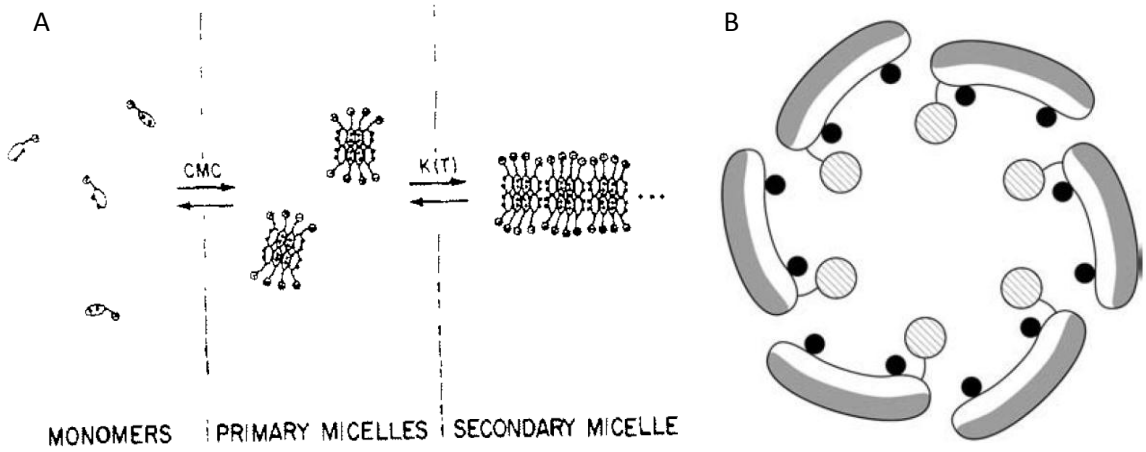

Figure 1-4 - Schematic representations of bile acid aggregates. (A) Primary-secondary hypothesis for BA aggregation proposed by Small 1979 [14]**. (B) Helical micelle of deoxycholic acid seen from top. Adapted from** [8,14]

Submicellar aggregation of BAs

The disparity between recovered CMC values for BAs is due to the small aggregate size. In fact, the aggregation number (total number of molecules in the aggregate, N_{agg}) of BAs in micelles is small ($2 \leq N_{\mathrm{agg}} \leq 15$) comparing with classic amphiphiles ($N_{\mathrm{agg}} \geq 50$) [6,9]. Actually, the aggregation number increases in a concentration-dependent fashion, which means that aggregate size is increasing in a stepwise fashion as BA concentration increases [9,10]. Oddly enough, the aggregation constant for the formation of an even-numbered aggregated is larger than that for a neighbouring odd-numbered aggregate. This means that micelles with an even number of molecules are more stable than micelles with an odd number of molecules [9].

Such low aggregation number render pre-micellar aggregates *imperceptible* to most detection methods, yet, BAs are very likely aggregated at sub-micellar concentrations (in even-numbered aggregates, Figure 1-5) to better reduce the exposed hydrophobic part.

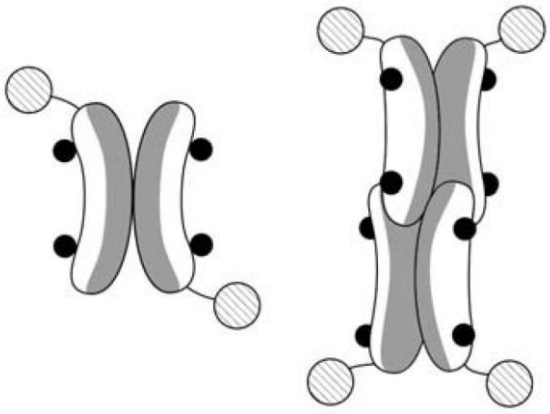

Figure 1-5 - Schematic representation of different models for submicellar aggregates of BAs. Adapted from [8]

1.3.Bile acids and apoptosis

When enterohepathic circulation is obstructed, BA concentration in the liver greatly increases and cholestasis happens [5]. Although cholestasis can have a myriad of causes, from cirrhosis to liver or pancreatic carcinoma, the result is always the same: obstruction of normal bile flow, resulting in BA accumulation in the liver [5]. Hepatocyte cellular and mitochondrial membranes are in danger of BA-solubilisation and liver damage can be severe if cholestasis is left untreated [5]. Interestingly, BA concentration never reaches the levels required for membrane solubilisation, remaining well below the CMC. Nevertheless, cell death is the major consequence of cholestasis [5]. Only in the 1990s were BAs revealed to induce cell death by apoptosis and not by membrane solubilisation [18].

Apoptosis

Apoptosis is a programed and ordered cell death; this process is genetically conserved throughout evolution and allows for the removal of abnormal growing cells. Apoptosis can be induced by drugs, radiation, infection or growth factor deprivation as well as by cytotoxic T cells [19]. Major research is being conducted on trying to force malignant cells to enter apoptosis, providing a safer and more direct cancer therapy [19–21]. An apoptotic cell suffers various transformations: chromatin condensation and DNA hydrolysis, cytoplasmic shrinkage, membrane blebbing and, ultimately, the formation of apoptotic vesicles containing organelles and parts of the nucleus [20]. These vesicles are phagocytized by macrophages, clearing the tissue from debris [20].

Apoptosis can be induced by two entangled pathways: the intrinsic and the extrinsic pathway (Figure 1-6). Both are heavily dependent on transcription factor p53, a major player in deciding cell fate as it enhances the expression of pro-apoptotic proteins Bcl-2-associated X Proten (Bax), Bad, Noxa, Puma, Apoptic Protease activating Factor 1 (Apaf-1) and Caspases, a family of proteases termed *executioners* that are at the centre of apoptosis induction [20,22].

The intrinsic, or mitochondrial, pathway is a consequence of stresses that converge on mitochondria and that can lead to membrane permeabilization, release of apoptogenic proteins, specifically cytochrome *c*, and disruption of the mitochondrial membrane potential [20] (Figure 1-6). All these changes lead to caspase activation and ultimately cell death [20]. Two pro-apoptotic proteins Bax and Bad, are greatly linked to apoptosis activation via mitochondria as they undergo a conformational change and oligomerize in the mitochondrial membrane. There, they form pores, disrupting the mitochondrial membrane potential and releasing cytochrome *c* to the cytosol [20,23–25].

The extrinsic pathway, or death receptor pathway, is triggered by ligand:death-receptor interaction, e.g. Fas-ligand:Fas [26]. This interaction leads to caspase activation which, depending on the cell type, might be enough for apoptosis induction (Figure 1-6). For instance, in hepatocytes, the mitochondrial pathway needs to endorse the pro-apoptotic signal from death-receptors for apoptosis to happen [20].

Both pathways lead to cytochrome *c* release and apoptosome formation. This enormous protein complex is essential for apoptosis and it is formed by cytochrome *c*, Apaf-1 and Caspase-9 [26] (Figure 1-6).

Apoptosis can be stopped if pro-survival signals can stop the apoptotic signal. Pro-survival signals include growth factors and cytokines and several membrane proteins [27]. The most important anti-apoptotic response is through Phosphoinositide 3 Kinase (PI3K) and Protein Kinase B (Akt) or the MAP (Mitogen-Associated Protein)-family of kinases, these proteins can directly inhibit caspases and thus prevent apoptosis [27]. Akt can also inactivate the apoptotic Bad protein and activate Nuclear Factor-kappa B (NF-kB) [28]. Transcription factor NF-kB, reverts Bax and Bad effects on mitochondria through the expression of proteins from the Bcl family, namely B-cell lymphoma 2 (Bcl-2) [25] (Figure 1-6).

Different BA, different apoptotic behaviour

Hydrophobic BAs, such as DCA and LCA, activate cell death receptors in a ligand independent manner [29]; promote p53, EF2-1 and Cyclin D1 expression [23]; induce oxidative damage [30], promote Bax translocation to mitochondria [31] and mitochondrial dysfunction [24,30] (Figure 1-6). All these modifications are sufficient for Caspase-6 activation which leads to a signalling cascade, leading to further caspase activation and apoptosis induction [20,23] (Figure 1-6).

On the other hand, hydrophilic BAs prevent reactive oxygen species formation [24], Bax translocation to mitochondrial membrane [25], mitochondrial dysfunction [30] and death-receptor induced apoptosis [32], ultimately inhibiting apoptosis (Figure 1-7). Furthermore, hydrophilic BAs activate pro-survival proteins such as PI3K, Akt and MAP Kinase Kinase Kinase (MAPKKK) [33]. It has also been shown that UDCA translocates the nucleus of hepatocytes via nuclear steroid receptors [34], such as glucocorticoids receptors, and affects gene expression and enhances p53 degradation [35] (Figure 1-7). Furthermore, both pro-apoptotic proteins Cyclin D1 and EF2-1 have their expression levels decreased by UDCA or TUDCA incubation [35,36], even in the presence of pro-apoptotic DCA [23]. Also, TUDCA has been linked with relieving endoplasmic reticulum stress, another apoptosis-inducing signal, functioning as a

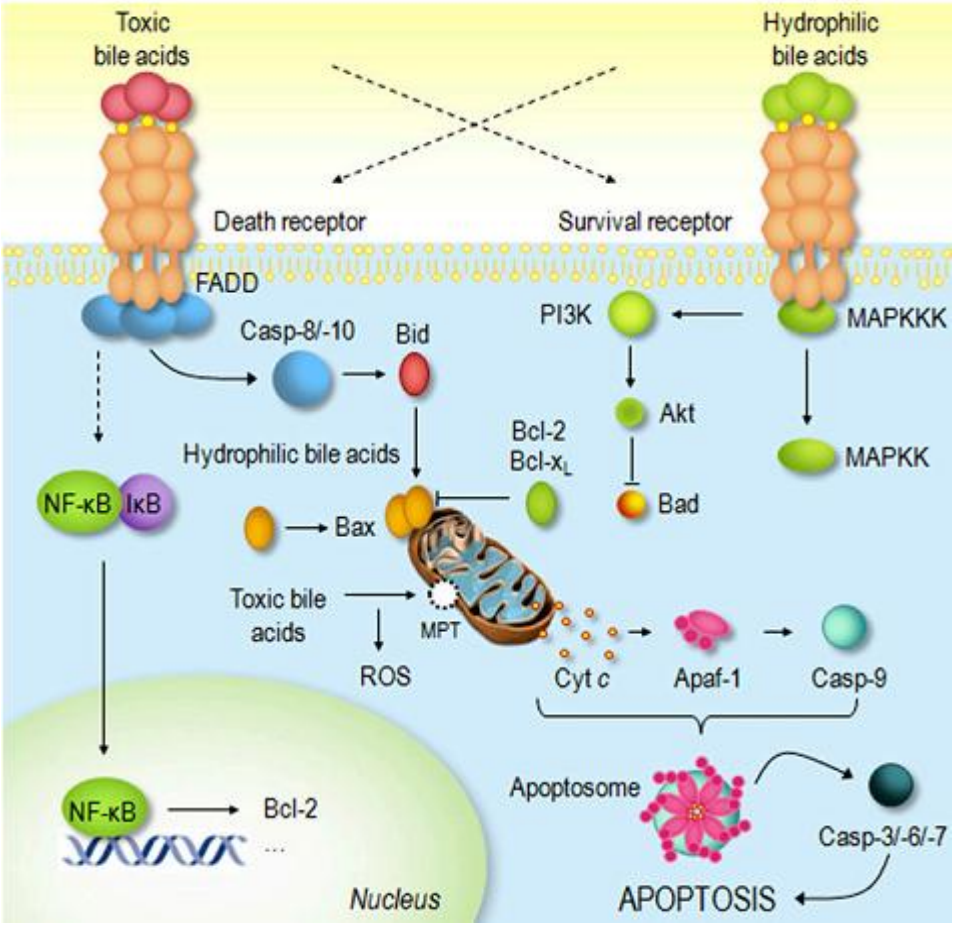

Figure 1-6 - Schematic representation of apoptosis induction through the extrinsic pathway, via death-receptor, or through the intrinsic pathway. Death-receptors activate caspases which are also activated by loss in mitochondrial integrity. The end result of both pathways is the formation of the apoptosome and apoptosis. Mechanisms for apoptosis prevention are also shown, from NF-kB-induced Bcl-2 expression to mitochondrial protection. Adapted from [22]

chaperone, inhibiting Caspase 12 activation [37].

Interestingly, the epithelial cells of the bile ducts and gallbladder, cholangiocytes, are in contact with high concentrations of BAs at all times [5]. These cells have developed evolutionary survival procedures to prevent BA apoptotic damage (Figure 1-6). In *normal conditions*, cholangiocytes express pro-survival proteins, for instance Bcl-2 and PI3K, as well as trigger mechanisms to inhibit apoptosis such as NF-κB activation and p53 cytoplasmic sequestration [5].

In summary, hydrophobic BAs promote apoptosis while hydrophilic BAs prevent apoptosis induced by hydrophobic BAs along with other apoptosis-inducing agents.

Apoptosis and lipid rafts

Lipid rafts are compartmentalisations within the plasma membrane driven by immiscibility between membrane components [21,38]. They are more rigid than the rest of the membrane as a consequence of a higher Chol and sphingolipids concentration [38]. These domains are called rafts since they were imagined as rigid domains *floating* in a fluid sea-like membrane [38]. In fact, lipid rafts are heterogeneous and highly dynamic structures, varying in lipid and protein composition [38]. They provide signalling platforms *in vivo*, capable of activating several cellular

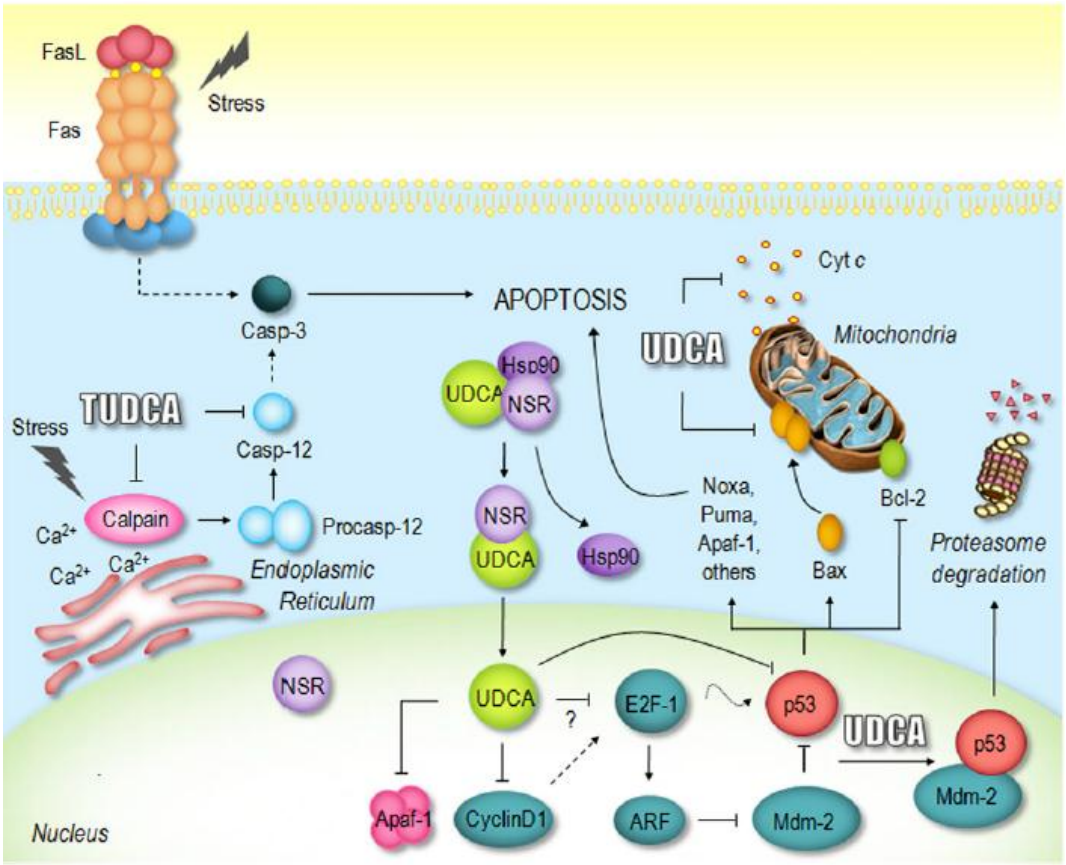

Figure 1-7 - Schematic representation of apoptotic prevention by hydrophilic bile acids UDCA and TUDCA. UDCA prevents cytochrome *c* release and Bax translocation to mitochondrial membrane. UDCA, also inhibits Cyclin D1, E2F-1 and p53 while promoting p53 degradation. TUDCA relieves ER stress, also inhibiting Caspase 12. Adapted from [20]

processes, specifically apoptosis [21].

For example, for the extrinsic pathway of apoptosis to have impact, the death-receptor Fas must be oligomerized and distributed to lipid rafts [39]. Recent studies have shown that ceramide, a degradation product of sphingomyelin and lipid raft component, has the ability to increase Fas oligomerization and activate apoptosis in a Fas-ligand-independent fashion [40]. Likewise, a recent anti-tumour drug, edelfosine, has been related with Fas translation to lipid rafts and consequent apoptosis induction [41,42]. Other pro-apoptotic membrane receptors, CD20 and CD5, can be activated without their specific ligand, as consequence of oligomerization by raft formation/fusion [43,44]. However, several Chol-depletion studies have shown a direct link between Chol deprivation, i.e. raft collapse, and apoptosis [19,45].

1.4.Bile acid interaction with lipid membranes

BAs are known to interact and partition to lipid membranes [46–51]. This interaction is stronger has the membrane Chol levels decrease [46]. Still, hydrophobic BAs are less affected by Chol membrane concentration than hydrophilic BAs [46]. It was also proposed that any BA could displace another BA from model membranes and that this effect was enhanced by Chol [46].

BAs have long been implicated in the dissolution of gallstones (Chol-rich depositions in the gallbladder). Patients with these depositions often take oral supplements of UDCA, however this particular BA has been shown to be a poor Chol solubiliser, whereas hydrophobic BAs, namely DCA, interact more efficiently with Chol [52].

Güldütuna and colleagues have proposed that UDCA mimicked Chol, increasing membrane order and rigidity as well as decreasing partition of other BAs to model membrane systems [47]. This study even claimed that UDCA position in membranes systems is identical to Chol, intercalated between other lipids [47] (Figure 1-8). Chol and UDCA would compete for the same position in the membrane. In this way, the effect of Chol in BA partition would be a consequence of BA displacement from the membrane. Permeabilization studies showed that hydrophobic BAs increase the membrane permeability and that UDCA could prevent this effect [47]. Hydrophobic BA-induced membrane permeabilization was also shown to happen in mitochondrial membrane, which was again prevented by UDCA [48].

Further studies involving BA position in membrane have asserted that taurine-conjugated hydrophilic BA are probably placed adhering to the membrane surface whereas taurine-conjugated hydrophobic BA could be inserted into the membrane interior [50].

Remarkably, BAs were shown to partition greatly to sphingolipid-rich membranes [51] and alter their packing [49]. Also, BAs were shown to partition to membrane and alter membrane properties, such as fluidity, and permeability to small ions and proteins, and that hydrophilic BAs protect membranes from the effects of hydrophobic BAs [47,48,53].

However, there is still a variety of questions concerning BA interaction with membranes: do all hydrophobic BAs intercalate phospholipids? Is hydrophilic BA interaction only superficial? Do they interact as monomers or as oligomers?

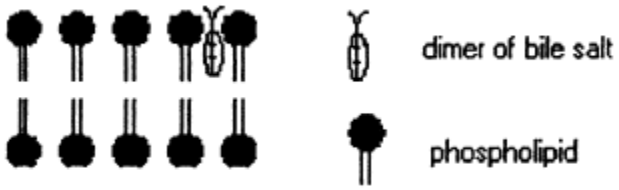

Figure 1-8 – Model for BA aggregation according to Guldutuna [47]**. BA dimer would intercalate the phospholipids in the membranes, only leaving its carboxyl tail on the membrane/water interface**

1.5. Bile acid as putative modulators of membrane properties and cell signalling

The plasma and mithocondrial membranes are, arguably, the most important organelle of the cell: membranes control a variety of signalling cascades, are docking sites for several enzymes, maintain concentration and hydroelectric gradients, etc. They are the entrance and exit points of the cell. Membranes are now seen as complex structures, composed of microdomains, e.g. lipid rafts, with different protein and lipid composition. Membrane domain composition might influence cell signalling and fate, e.g. aggregation of lipid rafts has been shown to concentrate apoptotic molecules increasing death receptor-ligand interaction [39,43,45].

From previous results concerning hydrophilic-hydrophobic BA interaction [46–48] two hypotheses were proposed: either BAs interact in solution, possibly aggregating, and this prevents partition to membranes; or partitioned-BAs alter membrane properties that prevent further BAs partition. Several studies have been published supporting the second hypothesis, suggesting a membrane-altering-effect for BAs [47–49]. The main argument is that this membrane-displacement effect is dependent on membrane composition and is maintained when vesicles are separated from buffer containing first BAs.

Given the effect of BAs on death receptor activation in the plasma membrane [29], it is possible that BA-induced apoptosis is achieved through alterations of the plasma membrane structure. In fact, the apoptotic effects of hydrophobic BAs are suppressed upon Chol depletion and DCA has been shown to induce a significant change in both concentration and distribution of Chol in the plasma membrane [54,55]. On the other hand, a hydrophilic BA did not exhibit this effect suggesting that BAs may have different effects on lipid membranes depending on their molecular properties [54].

Objective

The hypothesis of this work is that BAs act by changing membrane biophysical properties. The main objective is to determine the mechanism by which hydrophobic induces apoptosis and clarify the cytoprotective role of hydrophilic BAs.

Three putative mechanisms for the cytoprotective role of hydrophilic BAs will be studied here: (1) hydrophilic BAs interact with hydrophobic BAs chemically, forming an innocuous, membrane-*unaffecting*, non-apoptotic species, (2) hydrophilic BAs can decrease hydrophobic BAs partition to lipid membranes, (3) hydrophilic BAs can counter the membrane altering effect of hydrophobic BAs. Any of these mechanisms would result in a prevention of membrane compromise, leading to cell survival.

The work will be divided into four parts, each concerning with different approaches. First, labelled BA behaviour in aqueous solution will be assessed. Then labelled BA partition to model membrane system will be quantified. Unlabelled BA effect on membrane biophysical parameters will be observed. Lastly, unlabelled BA influence on live cells will be monitored.

2. Materials and methods

2.1.Chemicals

2.1.1. Reagents

To better study the effect of hydrophobic and hydrophilic BAs on cells, DCA, UDCA and TUDCA were chosen because of more frequent use in biological studies (Figure 2-1). Also, fluorescent derivates of DCA and UDCA with nitro-2-1,3-benzoxa.diazol-4yl (NBD) fluorophore were prepared by the Medical Research Group from the iMed, a research unit from Faculdade de Farmácia, Universidade de Lisboa (FFUL) (Figure 2-2).

1-palmitoyl-2-oleoyl-*sn*-glicero-3-phosphocholine (POPC), *N*-palmitoyl-*D*-erythro-sphingosylphosphorylcholine (PSM) and 1,2-dipalmitoyl-*sn*-glycero-3-phosphoethanolamine-*N*-

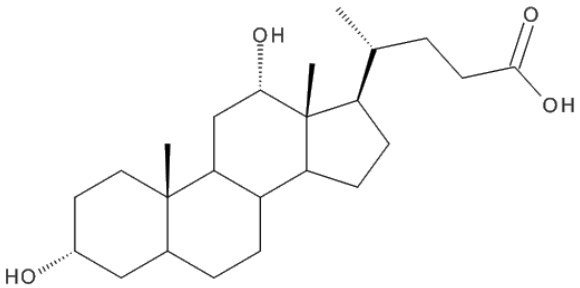

Deoxycholic acid (DCA)

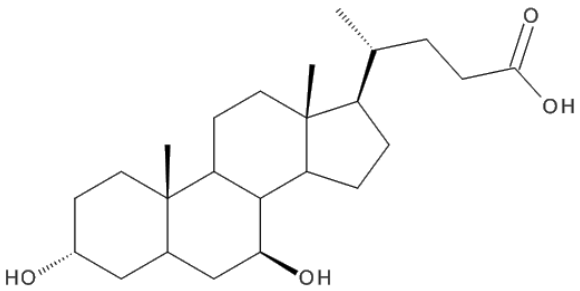

Ursodeoxycholic acid (UDCA)

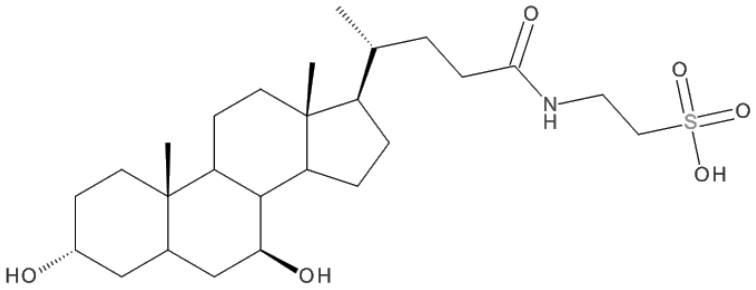

Tauroursodeoxycholic acid (TUDCA)

Figure 2-1- Chemical structures of deoxycholic acid (DCA - top), ursodeoxycholic acid (UDCA - middle) and tauroursodeoxycholic acid (TUDCA - bottom). Notice how the only difference between DCA and UDCA is the position of the –OH groups: DCA is hydroxylated in carbons 3 and 12 whereas UDCA and TUDCA are hydroxylated in carbons 3 and 7. TUDCA is the taurine-conjugated version of UDCA.

biotinyl (DPPE-biotin) were purchased from Avanti Polar Lipids (Alabaster, AL, USA) and cholesterol (Chol) from Sigma-Aldrich (St. Louis MO, USA), All lipids were kept in Uvasol grade chloroform (Sigma-Aldrich)

Unlabelled bile acids deoxycholic acid and tauroursodeoxycholic acid were purchased in sodium salt form from Sigma-Aldrich. Ursodeoxycholic acid sodium salt was purchased from Santa Cruz Biotechnologies (Santa Cruz, CA).

HEPES, Sodium chloride (NaCl), avidin and poly-L-lysine were purchased from Sigma-Aldrich. Perchloric acid and ammonium heptamolybdate were purchased from Merck (Darmstadt, Germany), ascorbic acid from VWR (Radnor, PA) and sucrose from Fluka (Buchs, Switzerland).

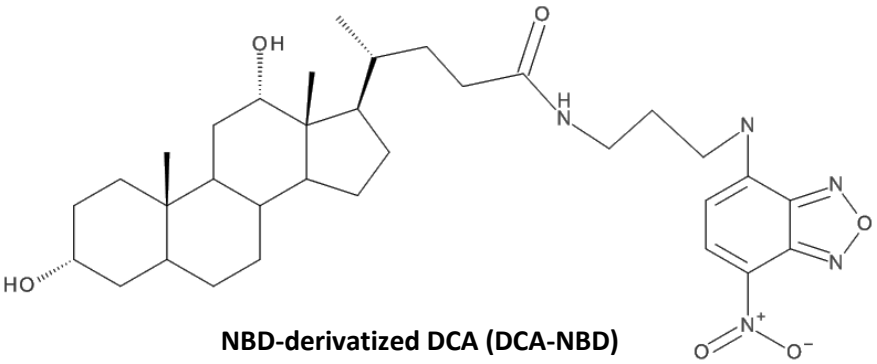

NBD-derivatized DCA (DCA-NBD)

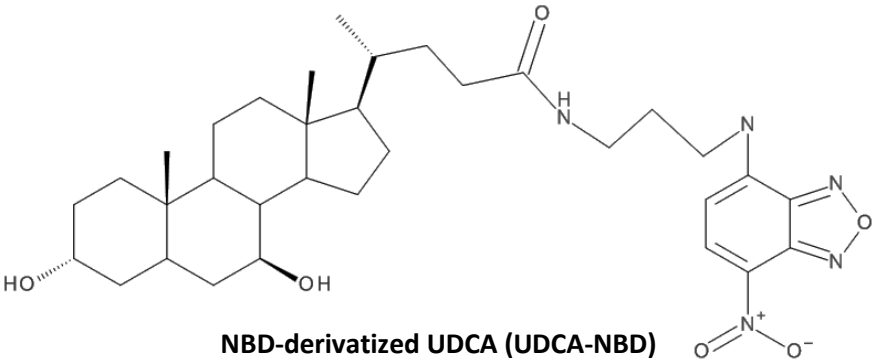

NBD-derivatized UDCA (UDCA-NBD)

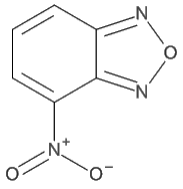

Nitrobenzoxadiazole (NBD)

Figure 2-2 - Chemical structures of NBD-derivatized deoxycholic acid (DCA-NBD - top), NBD-derivatized ursodeoxycholic acid (UDCA-NBD - middle), nitrobenzoxadiazole (NBD - bottom). Note that labeled BA lose the carboxyl groups and its negative charge and yield a longer side chain with a zwitterionic group attached.

2.1.2. Probes

Nile Red, 1,6-Diphenyl-1,3,5-Hexatriene (DPH), 1-(4-Trimethylammoniumphenyl)-6-Phenyl-1,3,5-Hexatriene *p*-Toluenesulfonate (TMA-DPH) and 1-[2-Hydroxy-3-(N,N-di-methyl-N-hydroxyethyl)ammoniopropyl]-4-[β-[2-(di-n-butylamino)-6-napthyl] vinyl]pyridinium dibromide (ANEPPDHQ) were purchased from Invitrogen (Carlsbad, CA, USA). 1,2-dioleoyl-*sn*-glycero-3-phosphoethanolamine-*N*-(lissamine rhodamine B sulfonyl) (Rho-DOPE) and 1,2-dipalmitoyl-*sn*-glycero-3phosphoethanolamine-N-(7-nitro-2-1,3-benzoxa.diazol-4yl) (NBD-DPPE) were obtained from Avanti Polar Lipids.

The following probes were used in this project. Probe concentrations were determined spectrophotometrically, from absorbance data and published absorption coefficients (Table 2-1). Probes were kept in UVasol-grade solvents at -26ºC.

Table 2-1 – Summary of probe characteristics. Excitation/absorbance (exc/abs) and emission (em) maximum wavelengths are shown. Extinction coefficients and solvent used for concentration determination and storage are shown.

Probe	ε_{max} ($M^{-1}.cm^{-1}$)	Ref	$\lambda_{max}^{exc/abs}$ (nm)	λ_{max}^{em} (nm)	Solvent
DCA-NBD	21×10^3	[56]	458	525-535	Methanol
UDCA-NBD	21×10^3	[56]	458	525-535	Methanol
Nile Red	45×10^3	[57]	552	636	Methanol
DPH	80.6×10^3	[58]	355	420	Chloroform
TMA-DPH	53×10^3	[58]	355	420	Chloroform
ANEPPDHQ	36×10^3	[57]	460	Sil0	Chloroform
Rho-DOPE	95×10^3	[56]	559	585	Chloroform
NBD-DPPE	21×10^3	[56]	458	525-535	Chloroform

2.1.3. Cell culture

Human embryonic kidney 293 cells (HEK293) were used. These were grown in flasks and maintained in Dulbecco's Modified Eagle Medium (DMEM) (Gibco, Carlsbad, CA) with 10% fetal calf serum and 1% penicillin-streptomycin at 37ºC in a humidified atmosphere with 5% CO_2.

2.2.Model membrane system preparation

2.2.1. Large Unilamellar vesicles (LUVs)

Required volumes of lipid and fluorescent probe stock solutions were mixed in chloroform and dried under a flow of dry nitrogen gas (N_2). Last traces of solvent were removed overnight under vacuum. Multilamellar vesicles were then obtained through solubilisation in HEPES buffer (10 mM HEPES, 150 mM NaCl at pH 7.4, prepared in MillQ water) followed by 6 freeze-thaw cycles. Thawing temperature used was always above the melting temperature of

the lipid with the highest melting temperature in the mixture. LUVs were produced by extrusion through a polycarbonate filters with 100 nm orifices (Whatman, USA) on a mini-extruder (Avanti). The lipid mixture was extruded at least 31 times. LUVs were kept at room temperature and in the dark until being used, at most for 48 hours after being prepared.

2.2.2. Giant Unilamellar vesicles (GUVs)

Required volumes of lipid and fluorescent probe stock solutions were mixed in chloroform to a final lipid concentration of 1 mM. This mixture was supplemented with 1 nM of biotinylated lipid DPPE-biotin. 2 µL of this solution were spread over each of the 4 faces of a pair of Platinum electrodes, which were dried in vacuum for about 15-30 minutes. Electrodes were the placed in 1 mL of a pre-heated 200 mM sucrose solution, in MilliQ water, and connected to signal generator for 1h15min. Electroformation occurred at a temperature over the melting temperature of the lipid with the highest melting temperature in the lipid mixture [59].

After electroformation, electrodes were shaken to release GUVs from electrodes and 150 µL of GUV solution were transferred to an eight-well µ-Slide from Ibidi (Munich, Germany). A fraction of pipette tip had to be cut, enlarging tip diameter, in order to prevent GUV collapse during pipetting. µ-Slide had been previously incubated overnight with 0,1 mg/mL avidin and had been extensively washed with MilliQ water to remove excess avidin. Avidin binds to biotin from biotinylated lipids guaranteeing GUV immobilization in the bottom of the slide. Each well was filled with 250 µL of buffer. Buffer osmolarity was adjusted using an A0300 Osmometer from Knauer (Berlin, Germany) to match the osmolarity of the 200 mM Sucrose solution (±5%) so as to prevent GUVs from bursting due to osmotic pressure. GUVs were left to equilibrate in the slides for 30min before measurements.

2.2.3. Lipid quantification

Phospholipid concentration, namely POPC, PSM and biotinylated lipid concentration, was assessed using a methodology described elsewhere [60]. Briefly, this method is based on the determination of inorganic phosphate obtained after acid hydrolysis, using perchloric acid, from phospholipids at 200ºC. Released phosphate reacted with ammonium heptamolibdate yielding phosphomolybdic acid, which is reduced by ascorbic acid to a blue compound, spectrophotometrically detectable at 815nm.

Chol concentration in stock solution was determined gravimetrically with a high-precision scale. Empty vials were weighted in and then filled with a certain volume of Chol stock solution. Chloroform, was evaporated using nitrogen gas and kept in vacuum overnight to ensure complete solvent evaporation. Vials with Chol film were weighted and Chol mass was determined by the difference in masses from registered weights.

2.3.Cell membrane labelling and BA incubation

Cells were seeded in eight-well µ-Slides from Idibi at 20 000 cells per well to achieve approximately 80% confluence. Slides were precoated with poly-L-lysine.

Di-4-ANEPPDHQ was used for plasma membrane labelling to a final concentration of 10 µM in Phosphate Buffered Saline solution (Gibco). Cells were incubated for 30min with probe solution and then washed with DMEM. Cells were then incubated for another 30min with either 100 µM of DCA or TUDCA or TUDCA followed by DCA in DMEM. Cells were not washed after this treatment.

DCA-NBD and UDCA-NBD were added to a final concentration of 20 µM to unlabelled cells and incubated for 30min before imaging.

2.4.Absorption and fluorescence measurements

2.4.1. UV-Vis absorption spectroscopy

UV-Vis absorption spectra were performed in a Shimadzu UVPC-3100 spectrophotometer (Shimadzu, Kyoto, Japan). For probe concentration determination, 1cm×0.4cm Hellma quartz cuvettes were used and absorption coefficients considered for each probe are shown in Table 2-1. For phospholipid concentration determination 1 cm×1 cm Hellma quartz cuvettes were used.

2.4.2. Steady-state fluorescence spectroscopy

Fluorescence steady-state measurements were performed in a SLM-Aminco 8110 Series 2 spectrofluorimeter (Rochster, NY) with double excitation and emission monochromators (MC-400, Rochster, NY), in right-angle geometry. Light source was a 450-watt Xe arc lamp and the reference was a Rhodamine B quantum counter solution. Temperature was controlled by a thermostated cuvette holder and magnetic stirring was used.

Typically, measurements were made with 4 and 16 nm bandwidth, for excitation and emission respectively. Polarization of excitation and emission light was achieved using Glan-Thompson polarizers. Excitation and emission polarizers were positioned at 0º and 54.7º angles respectively. Both 1 cm×1 cm and 0.5 cm×0.5 cm Hellma quartz cuvettes were used in this study. Fluorescence intensities are calculated through integration of the obtained spectrum.

When using high fluorophore concentrations inner-filter effects must be considered. Fluorescence intensity is proportional to the intensity of the exciting light, when using mixture with high absorbance at the exciting wavelength, the intensity of the exciting light will vary in the optic path [61]. This will lead to an *apparent* decrease in fluorescence which can be corrected using the following formula [62]:

$$I_{corr} = I_{obs} \times 2.303 \times \frac{Abs}{1 - 10^{-Abs}} \quad \textbf{Eq. 1}$$

Fluorophore absorbance is calculated using fluorophore concentration and the extinction coefficient present in Table 2-1. This correction is only valid if $I_{corr} < 3 \times I_{obs}$, which was always observed.

Background fluorescence intensity was subtracted using a solution containing either unlabelled vesicles and/or unlabelled bile acids. Excitation and emission spectra were corrected for different instrumental response, due to inherent lamp and monochromator characteristics, as well as wavelength-dependent photomultiplier sensitivity.

Fluorescence anisotropy measurements are based on the quantification of the depolarization of fluorescence after excitation of fluorophores with polarized light. In this way, fluorescence anisotropy is very sensitive to the rotational dynamic of the fluorophore. Steady-state anisotropies were determined according to the following equation (Eq. 2, [61]):

$$< r >= \frac{I_{\mathrm{VV}} - G.I_{\mathrm{VH}}}{I_{\mathrm{VV}} + 2.G.I_{\mathrm{VH}}} \quad \textbf{Eq. 2}$$

where the different intensities, I_{ij}, are the steady-state vertical and horizontal components of the fluorescence emission with vertical excitation, I_{VV} and I_{VH} respectively, and horizontal excitation, I_{HV} and I_{HH} respectively, to the emission axis. The latter pair of components is used to calculate the G factor ($G = I_{\mathrm{HV}}/I_{\mathrm{HH}}$), which is a correction for the different sensitivity of the optics in the spectrofluorimeter to polarized light.

Fluorescence anisotropy is highly dependent on the lifetime of the fluorophore. The main driving force behind depolarization is its rotational diffusion. Consequently, if the fluorophore has free motion and remains on the excited state for a large amount of time, its fluorescence anisotropy will be close to zero. Now, if the lifetime is decreased, fluorescence anisotropy will be higher since the fluorophore will not have as much time to rotate. The relationship between fluorescence lifetime and anisotropy is described by the Perrin equation (Eq. 3, [61]):

$$< r >= \frac{r_0}{1 + {< \tau >}/{\theta}} \quad \textbf{Eq. 3}$$

where r_0 is the fundamental anisotropy of the fluorophore, $< \tau >$ is the average lifetime the fluorophore spends in the excited state and θ is the rotational diffusion coefficient.

2.4.3. Transient-state fluorescence spectroscopy

Fluorescence decays were obtained with the Time-Correlated Single-Photon Timing technique (TCSPT). A laser pulse excites the sample and starts a voltage ramp, which is stopped when a sample-emitted photon is detected. The measured voltage is proportional to the time between sample excitation and photon detection. The excitation laser is fired at a high

repetition rate and experimental conditions are adjusted so that, for each excitation pulse, there is less than 1% probability of detecting a photon. Sequentially, a multichannel analyser converts the voltage to a temporal channel, using an analogue-digital converter. Through the accumulation of several pulses it is possible to acquire a histogram of photon counts as a function of elapsed time since sample excitation.

The fluorescence intensity decays were obtained with excitation and emission polarizers at 0º and 54,7º respectively. Anisotropy decays were obtained alternating emission polarizer position between 0º (vertical) and 90º (horizontal) degrees, keeping the excitation polarizer in the vertical position. Light was completely depolarized after passing through the polarizers. In this way no correction factor was needed, and detected light was proportional to emitted light. Fluorescence anisotropy is calculated using a simplified version of the previous equation (Eq. 4, [61]):

$$< r > (t) = \frac{I_{\mathrm{VV}}(t) - I_{\mathrm{VH}}(t)}{I_{\mathrm{VV}}(t) + 2.I_{\mathrm{VH}}(t)} \qquad \textbf{Eq. 4}$$

Excitation pulses were produced by a Ti-Sapphire solid state laser system (used for 460 nm excitation) or a frequency-doubled cavity-dumped dye laser of DCM (Coherent 701-2) (used for 340 nm excitation). Emission wavelengths were selected using a Jobin Yvon HR320 monochromator (Horiba Jobin Ivon Inc.). The excitation pulse profile was obtained using a scattering Ludox mixture, an aqueous solution of colloidal silica (Sigma-Aldrich). Decay curves were stored in 1024 channels and the used time-scale varied according to experimental conditions, from 9.76 to 48.8 ps/ch. The number of counts in the peak channels of the sample decay and instrumental response function were 20 000 to 50 000 respectively. 0.5 cm×0.5 cm Hellma quartz cuvettes were used and samples were always under magnetic stirring. All measurements were performed at room temperature.

2.4.3.1. Fluorescence decay analysis

Consider the fluorescence intensity of a sample through time, at $t = 0$ s, immediately after the excitation pulse, the fluorescence intensity is maximum and decreases through time at an exponential rate. For monoexponential decays, this process can be described by the following equation (Eq. 5, [61]):

$$I(t) = I_0 \exp(^{-t}/_{\tau}) \qquad \textbf{Eq. 5}$$

where I_0 is the fluorescence intensity immediately after excitation and τ is the average time the fluorophore remains on the excited state.

For more complex decays, a sum of exponentials has to be used to describe the decay. Consequently, the intensity decay of a fluorophore is given by (Eq. 6, [61]):

$$I(t) = \sum_{i=1}^{n} \alpha_{\mathrm{i}} \exp(^{-t}/_{\tau_i}) \qquad \textbf{Eq. 6}$$

where α_i and τ_i, are the pre-exponential factors and lifetime of the ith component.

The association between steady-state fluorescence intensity and its decay, $I(t)$, is given by (Eq. 7, [61]):

$$I \propto \int_0^\infty I(t)dt \qquad \textbf{Eq. 7}$$

Solving Eq. 7 with the general decay equation (Eq. 6) we reach a parameter, $\bar{\tau}$, which is called lifetime-weighted quantum yield (Eq. 8, [61]).

$$I \propto \sum_{i=1}^{n} \alpha_i \tau_i = \bar{\tau} \qquad \textbf{Eq. 8}$$

The lifetime-weighted quantum yield of a fluorophore is proportional to fluorophore quantum yield.

The average lifetime of a fluorophore exhibiting a multi-exponential decay is calculated by the following equation (Eq. 9, [61]):

$$< \tau >= \frac{\int_0^\infty t.I(t)dt}{\int_0^\infty I(t)dt} = \frac{\sum_i^n \alpha_i \tau_i^2}{\sum_i^n \alpha_i \tau_i} = \frac{\sum_i^n \alpha_i \tau_i^2}{\bar{\tau}} \qquad \textbf{Eq. 9}$$

To analyse the decays obtained by TCSPT one must consider that they do not directly represent the fluorescence emission kinetics of a sample excited with an infinitesimal-timed pulse. The excitation pulse lasts for several picoseconds and the experimental curves, $I_{\exp}(t)$, are distorted by the finitesimal duration of the pulse. In this way, the decay law is convoluted with the pulse function and $I_{\exp}(t)$ by the following equation (Eq. 10, [61]):

$$I_{\exp}(t) = \int_{t'=0}^{t} L(t') \times I(t-t')dt = L \otimes I \qquad \textbf{Eq. 10}$$

Decay curves were analysed with TRFA (version 1.4) from Scientific Software Technologies Centre (Belarusian State University). Briefly, this programs fits the previous equation (Eq. 10) to the experimentally obtained decay, $I_{\exp}(t)$, using the empirically obtained instrumental response curve, $L(t)$, and recovers the decay law, $I(t)$ from optimizing α_i and τ_i values. A non-linear regression by the least-squared method based on Marquardt algorithm [63] was employed. Fits were accepted when χ_2 value was lower than 1.4 and weighted residuals and autocorrelation plots were randomly distributed around 0.

Fluorescence anisotropy decays

Time-resolved fluorescence anisotropy is calculated by Eq. 4. The fluorescence anisotropy decay can be described by a sum of exponentials, described in the following equation (Eq. 11, [61]):

$$r(t) = \sum_{i=1}^{n} \beta_{\mathrm{i}} \exp(-{}^{t}/_{\theta_{\mathrm{i}}}) + r_{\infty} \qquad \textbf{Eq. 11}$$

Where β_{i} and θ_{i} represent the initial anisotropy and rotational diffusion coefficient of the ith component of the decay. The r_{∞} parameter represents the limiting anisotropy of a sample, which can be a sign of restricted depolarization. The utility of this parameter will be discussed further below. Note that $(\sum_{\mathrm{i}}^{n} \beta_{\mathrm{i}}) + r_{\infty} = r(0)$.

Obtained decays were also analysed in TRFA but in a more complex manner. Firstly, the signal from both components was adjusted to a global intensity decay, $I_{exp}(t)$, by solving the following system of equations for $I_{\mathrm{exp}}(t)$ (Eq. 12, [61]):

$$\begin{cases} I_{\mathrm{VV}}^{\mathrm{exp}}(t) = \dfrac{I_{\mathrm{exp}}(t)}{3}\left[1 + 2.r_{\mathrm{exp}}(t)\right] \\ I_{\mathrm{VH}}^{\mathrm{exp}}(t) = \dfrac{I_{\mathrm{exp}}(t)}{3}\left[1 - r_{\mathrm{exp}}(t)\right] \end{cases} \qquad \textbf{Eq. 12}$$

First, α_{i} and τ_{i} values were recovered from fitted $I_{\mathrm{exp}}(t)$ curves as described above. Then a $r_{\mathrm{theoretical}}(t)$ curve was fitted to the $r_{\mathrm{exp}}(t)$ curve optimizing α_{i}, β_{i} and θ_{i} and r_{∞} values while maintaining fixed the τ_i values recovered from the first fit. Once again, a nonlinear regression by the least-squares method based on the Marquardt algorithm was employed [63]. The criteria for accepting fits were the same as for non-polarized fluorescent decays.

2.4.4. Partition coefficient determination

To determine partition coefficients to vesicles as a function of lipid concentration [64] the following equation was fitted to the partition data (Eq. 13):

$$I = \frac{I_{\mathrm{w}} + K_{\mathrm{p}}\gamma_{\mathrm{L}}[L]I_{\mathrm{L}}}{1 + K_{\mathrm{p}}\gamma_{\mathrm{L}}[L]} \qquad \textbf{Eq. 13}$$

where I_{w} and I_{L} is probe fluorescence intensity in solution or in the lipid membrane, respectively; K_{P} is the partition coefficient and γ_{L} is lipid molar volume, which is assumed to be 0.75 dm^3mol^{-1}. I_{w} is assumed to be the intensity obtained in the absence of lipid. I_{L} and K_{P} were optimized using the least-square method with Origin8 (OriginLab, Northampton, MA, USA).

2.4.5. FRET studies

Theory

Förster resonance energy transfer (FRET) occurs when an excited fluorophore (termed donor) transfers energy to a fluorophore in the ground-state (termed acceptor) in a non-radiative, long range dipole-dipole coupling mechanism. For FRET to occur, three conditions ought to be verified: donor emission spectrum must overlap with acceptor excitation spectrum; donor and acceptor molecules must be in proximity (typically <100 Å apart); donor emission and acceptor excitation momenta must not be perpendicular to each other.

FRET efficiency, E, ranges from 0 to 1 and is the standard parameter for comparing FRET experiments. In case of FRET to a single acceptor, it is dependent on the sixth power of the quotient between the distance, r, between the two fluorophores and the Förster radius (R_0) of the donor-acceptor pair, the distance upon which $E = 50\%$ (Eq. 14, [61]).

$$E = \frac{1}{1 + \left(\frac{r}{R_0}\right)^6} \qquad \textbf{Eq. 14}$$

The Förster radius is calculated for each donor/acceptor pair through the following equation (Eq. 15, [61]):

$$R_0^6 = 8{,}79 \times 10^{-5} \times n^{-4} \times \phi_{\mathrm{D}} \times \kappa^2 \times J \ (R_0 \text{ in Å}^6) \qquad \textbf{Eq. 15}$$

where n is the refraction index, Q_{D} is the donor quantum yield in the absence of the acceptor, κ is the orientational factor, dictated by the relative orientation of donor emission and acceptor excitation momenta. J is the overlap integral between donor emission and acceptor excitation spectra and is described by the following equation (Eq. 16, [61]):

$$J = \int_0^\infty I_{\mathrm{D}}(\lambda)\varepsilon_{\mathrm{A}}(\lambda)\lambda^4 d\lambda \ \ (\lambda \text{ in nm}) \qquad \textbf{Eq. 16}$$

Several artefacts must be taken into account when designing and interpreting FRET results, as FRET efficiencies are strongly dependent on R_0, that is influenced by several parameters.

Obtaining FRET efficiencies

Energy transfer is a dark process that cannot be measured directly, one can only measure the end result, either acceptor sensitized-fluorescence or loss of donor fluorescence. Several complications are involved in FRET efficiencies calculation through acceptor emission, e.g., results need to be corrected, namely direct acceptor excitation and fluorescence upon donor excitation, and the differences in extinction coefficients between donors and acceptors must be accounted for. On the other hand, loss of donor fluorescence is a fairly simple and immediate way of calculating FRET efficiencies. Donor quantum yield decreases in the presence

of the acceptor and this can be quantified either by changes in steady-state fluorescence intensity, I, or donor lifetime, τ (Eq. 17, [61]):

$$E = 1 - \frac{\phi_{\mathrm{DA}}}{\phi_{\mathrm{D}}} = 1 - \frac{I_{\mathrm{DA}}}{I_{\mathrm{D}}} = 1 - \frac{\tau_{\mathrm{DA}}}{\tau_{\mathrm{D}}} \qquad \textbf{Eq. 17}$$

where the D and DA indexes represent donor alone or in the presence of the acceptor, respectively. In the FRET experiments present in this study, FRET efficiencies were calculated using the decrease in fluorescence lifetime and intensity of the donor molecule, NBD-DPPE, in the presence of the acceptor, Rhodamine-DOPE. NBD lifetime decay was acquired from photons with 500-530 nm in order to avoid contamination from acceptor fluorescence. R_0 for the NBD-DPPE/Rho-DOPE FRET pair was determined by Eq. 15 and Eq. 16 to be approximately 50 Å.

Estimating FRET efficiencies

It is possible to calculate an expected FRET efficiency value, assuming a random distribution of donor and acceptor molecules. Since membrane thickness is smaller than R_0 (40 to 50 Å, respectively), energy transfer can occur between both donors and acceptors in the same membrane leaflet (in-plane) or donors and acceptors in opposing leaflets (out-of-plane).

The donor decay law of the donor in the presence of the acceptor becomes (Eq. 18, Eq. 19 and Eq. 20, [56]):

$$i_{\mathrm{DA}}(t) = i_{\mathrm{D}}(t) \times \rho_{\mathrm{FRET}} \qquad \textbf{Eq. 18}$$

$$\rho_{\mathrm{FRET}} = \exp(-2 \times \sigma_{\mathrm{A}} \times \pi \times l^2 \times \int_0^1 \frac{1 - \exp(-t \times b^3 \times \alpha^6)}{\alpha^3} d\alpha) \qquad \textbf{Eq. 19}$$

$$b = (R_0^2/l)^2 \times \sqrt[3]{\tau_{\mathrm{D}}} \qquad \textbf{Eq. 20}$$

where σ_{A} is the acceptor density in each bilayer leaflet, and l is the distance between the plane of donor and acceptors. In the calculation of the surface density of acceptors, an area per molecule of 66.4, 47.8 and 37.7 $\mathrm{Å}^2$ for POPC, PSM and Chol, respectively, were considered.

2.5.Confocal fluorescence microscopy

All measurements were performed on a Leica TCS SP5 (Leica Microsystems CMS GmbH, Manheim, Germany) inverted confocal microscope (DMI6000). Excitation lines provided by an argon laser were focused into the sample by an apochromatic water immersion objective (63x, NA 1.2; Zeiss, Jena Germany). A 111.4 µm diameter pinhole in front of the image plane blocked out-of-focus signals.

Essentially, only two fluorophores were visualized by confocal microscopy: NBD, in DCA-NBD, UDCA-NBD or DPPE-NBD, and Rhodamine, in Rho-DOPE. The NBD group was excited at 458

nm and emission was collected between 480-570 nm. Rhodamine was excited at 514 nm and emission was collected between 570-620 nm.

GUV and cell images

XY slices separated by 0.4 µm along the z-axis were obtained at 200 or 400 Hz. 2d maximum intensity projections were constructed using the maximum intensity projection method [65]. Every slice was acquired in two different channels using the excitation and emission described above. Images were treated with ImageJ software (Wayne Rasband NIH, USA).

For I_d percentage determination, two maximum intensity projections of a GUV were obtained, the top and bottom hemispheres. The I_d percentage was the ration between the Rhodamine area in the two hemispheres and the total GUV area (Eq. 21):

$$f_{\mathrm{ld}} = \frac{A_{\mathrm{Rho}}(top) + A_{\mathrm{Rho}}(bottom)}{A_{\mathrm{GUV}}(top) + A_{\mathrm{GUV}}(bottom)} \qquad \textbf{Eq. 21}$$

where f_{ld} is the fraction of I_d in the GUV and $A_{\mathrm{i}}(hemisphere)$ the area of i in a given hemisphere determined with ImageJ software.

2.5.1. Fluorescence lifetime imaging microscopy

The microscope was coupled with a Ti-Sa multiphoton laser that allowed Fluorescence Lifetime Imaging Microscopy (FLIM). This technique is the imaging counterpart to the transient state fluorescence spectroscopy. Using the TCSPT methodology, samples were excited at 840nm using two-photon excitation that efficiently excited di-4-ANEPPDHQ. Full frame TCSPT histograms were recorded for 60s, with an open pinhole and fluorescence emission was selected using a 535/85 band-pass filter. The instrumental response curve was obtained through the measurement of the second-harmonic generation from urea crystals, using the same excitation wavelength. FLIM data analysis was performed with SPCImage software (Becker & Hickl) and the methodology was identical to the one employed for macroscopic time-resolved fluorescence decay analysis.

2.6.Isothermal titration calorimetry (ITC)

Titration was performed on a VP-ITC instrument from MicroCal (Northampton, MA) at 25ºC, injection speed of 0.5 µL/s, stirring speed 459 rpm and reference power 10 µcal/s. The first injection of 2 µL was disregarded to account for diffusion from/into the syringe tip during the equilibration period, still, the injected amount was taken into account in the calculations. The

titration proceeded with additions of 5 µL of injectant per step. All solutions had been previously degased for 15min.

The obtained thermogram was integrated using the data analysis software Origin 7.0 as modified by MicroCal to deal with ITC experiments. Concentrations in the cell were calculated, taking into account the volume that overflows the cell due to the addition of solution from the syringe considering that overflow is faster than mixing, meaning that the composition of the solution leaving the cell is the equilibrium composition before the addition. The predicted heat evolved in titration step i is calculated by Eq. 22:

$$q_{\mathrm{i}} = \Delta H \times \left(n^{\mathrm{i}}_{\mathrm{BA-Lipid}} - n^{\mathrm{i-1}}_{\mathrm{BA-Lipid}} \times \left(1 - \frac{V_{\mathrm{i}}}{V_{\mathrm{cell}}}\right)\right) + q_{\mathrm{dil}} \qquad \textbf{Eq. 22}$$

where ΔH is the molar partition enthalpy, $n^{\mathrm{i}}_{\mathrm{BA-Lipid}}$ is the number of moles of BA bound to the lipid after injection i, V_{i} is the volume injected, V_{cell} the volume of the cell and q_{dil} the dilution heat [66].

3. Results

3.1.Bile Acid aggregation

The first part of this thesis will focus on the aggregation of BAs in buffer. The first goal of this section is to establish if labelled BAs are good mimics of unlabelled BA. The second goal is to characterize the submicellar aggregation pattern of the labelled BAs and to test if it the aggregation pattern of DCA-NBD is affected by interaction with hydrophilic BAs at submicellar concentrations.

Fluorescence emission and excitation spectra in aqueous solution were obtained for the two labelled BAs, DCA-NBD and UDCA-NBD. The labelled BAs present identical excitation and emission spectra in buffer (Figure 3-1). The excitation maximum is at 480nm and both labelled BAs present a *local* excitation maximum at 340nm, corresponding to a π→π* transition, typical of the NBD fluorophore [67]. Fluorescence emission spectra have a maximum at about 540nm. This value changes in accordance to the polarity of the NBD environment [67]. Additionally, the NBD fluorophore presents significantly lower quantum yields in aqueous solutions that when in more hydrophobic environments, such as liposomes or organic solvents [67].

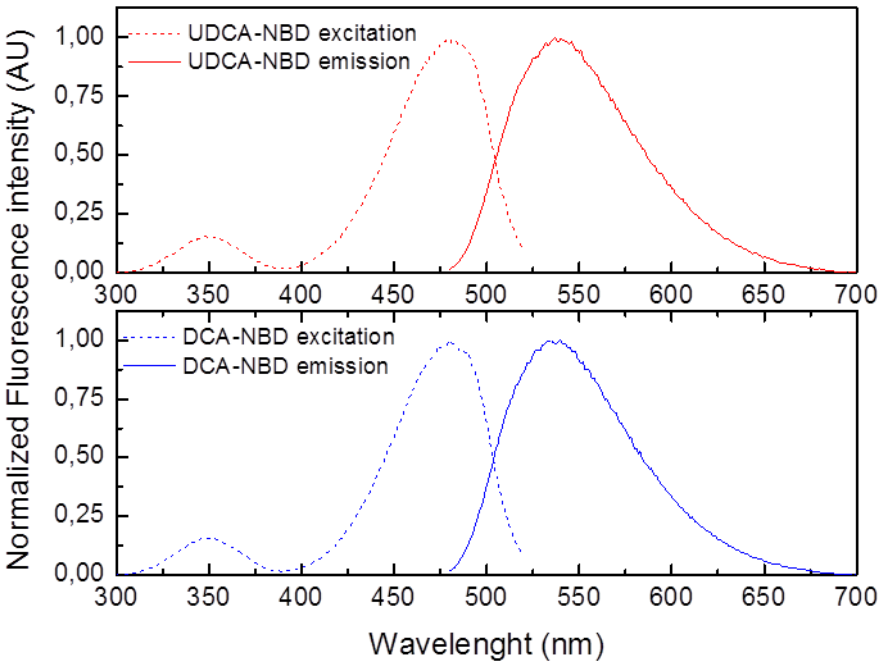

Figure 3-1 – Fluorescence emission and excitation spectra from DCA-NBD (blue) and UDCA-NBD (red) in HEPES buffer. For the excitation spectra (dashed), fluorescence emission was recovered at 540nm. For emission spectra (full), excitation was conducted at 460nm. Spectra were normalized to the maximum intensity.

3.1.1. Critical Micellar Concentration determination

Critical micellar concentration (CMC) is the concentration at which micelles of solute start to form. To determine if labelled BAs are good mimics of their respective BA, the CMCs of DCA and UDCA were determined using both DCA-NBD or UDCA-NBD and the hydrophobic probe Nile Red. This hydrophobic probe exhibits preferential partition to apolar environments, such as micelles and will be used as a control to determine if the labelled BAs present readily partition to micelles of unlabelled BAs.

To obtain micelles of BAs, volumes of each BA stock solution were stepwise added to a cuvette with 2 µM pf the respective labelled BA or Nile Red. Probe fluorescence emission spectra and fluorescence anisotropy were recorded as a function of total BA concentration.

DCA micellization

For DCA micellization studies, DCA was added to a 2 µM DCA-NBD solution; from 5 µM up to ≈ 10 mM total BA. An increase in fluorescence intensity and anisotropy is observed when DCA concentration reaches the 3 mM (Figure 3-2A). Fluorescence intensity and anisotropy plateau at a DCA concentration of 7 mM. Note that, the fluorescence intensity and anisotropy variations occur at the same DCA concentrations. This increase in fluorescence intensity can be associated with micelle formation as micelles sequester the NBD group from the solvent into a more apolar surrounding. This is complemented by a shift in the emission spectra of DCA-NBD to lower wavelengths (Figure 3-2B). An increase in the anisotropy of DCA-NBD is also indicative of DCA-NBD incorporation in DCA micelles, since micelles have a slower rotational diffusion than free DCA-NBD, which leads to less fluorescence depolarization of the probe.

From Figure 3-2A, three states of aggregation can be assigned to the results. Firstly, a premicellar state is assumed from 5 µM up to 2 mM, since there is no change in DCA-NBD signal. Above 2 mM of DCA, DCA-NBD quantum yield increases, which is indicator of DCA micelle formation, as discussed above. At concentrations over 6 mM, DCA-NBD signal is again constant, and it is assumed that all DCA-NBD is already incorporated in micelles. The CMC value for DCA can be calculated by the intersection between the tendency lines from the first and second state, premicellar and micelle formation [6]. Considering the fluorescence intensity signal (Figure 3-2A), the CMC value obtained is 2.5 mM. For the anisotropy signal, the mathematical treatment is the same and the CMC values retrieved is almost identical, 2.3 mM.

DCA was also stepwise added to a 2 µM solution of Nile Red. With Nile Red, a more gradual increase in fluorescence intensity is observed (Figure 3-3). Due to a very low fluorescence intensity signal of Nile Red in the absence of micelles, fluorescence emission anisotropy cannot be used to detect the CMC value, as errors associated with the measurements were very high. Although the shape of the curve is similar, the quantum yield of Nile Red is less sensitive to DCA micelle formation, leading to a CMC value of 3.3 mM. Additionally, total incorporation of Nile Red to DCA micelles is not achieved at 10 mM. The higher sensitivity of DCA-NBD to DCA micelle formation is indicative of a higher buffer to DCA micelle partition coefficient ($K_P(m,w)$). In fact while Nile Red is still not fully incorporated in micelles at 10 mM

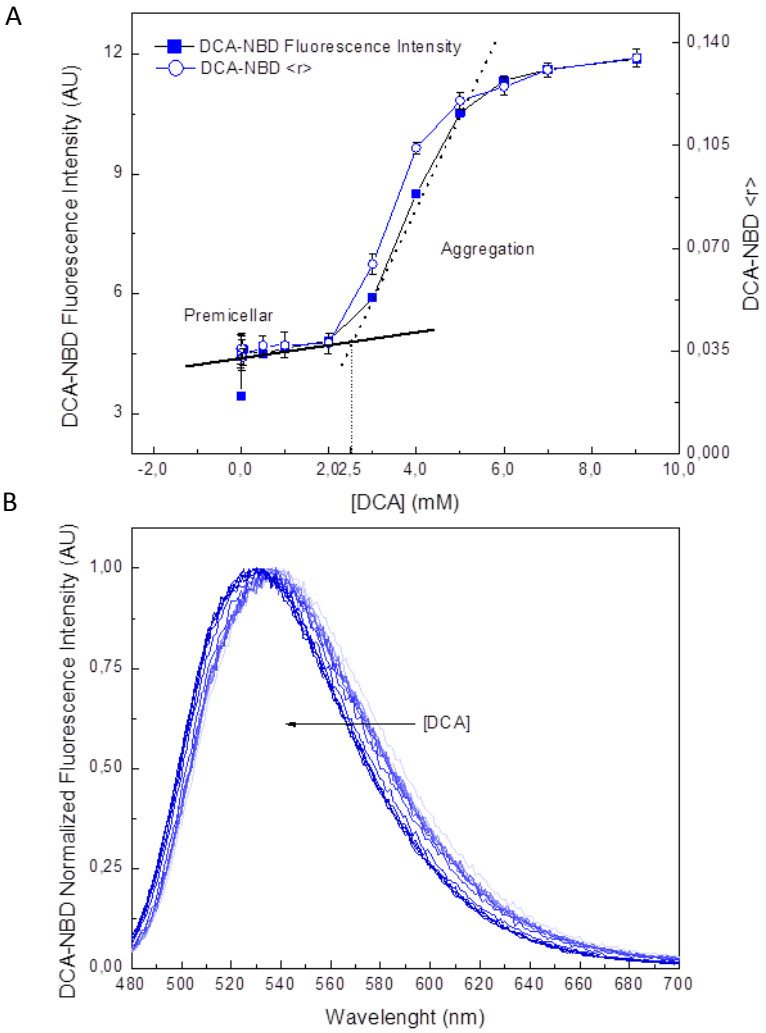

Figure 3-2 - DCA-NBD fluorescence emission intensities, anisotropies (A) and normalized emission spectra (B) as a function of DCA concentration. DCA was stepwise added to 2 µM of probe solution, fluorescence emission spectra were recorded. (A) DCA-NBD fluorescence emission intensity (closed squares) and anisotropy (open circles) as a function of total DCA concentration. Full black line represents the trend of the premicellar fluorescence intensity signal and black dashed line represents the trend upon micelle formation. Intersection between the two black lines is at 2.5 mM as shown by the black dotted line. (B) DCA-NBD emission spectra at several DCA concentrations, as shown by the tendency arrow. Spectra were normalized to value at maximum intensity. DCA-NBD was excited at 460 nm and emission was recovered between 480-700 nm, anisotropy was measured at 540nm. Fluorescence intensities were corrected for sample dilution.

DCA, DCA-NBD achieves this at 6-7 mM DCA.

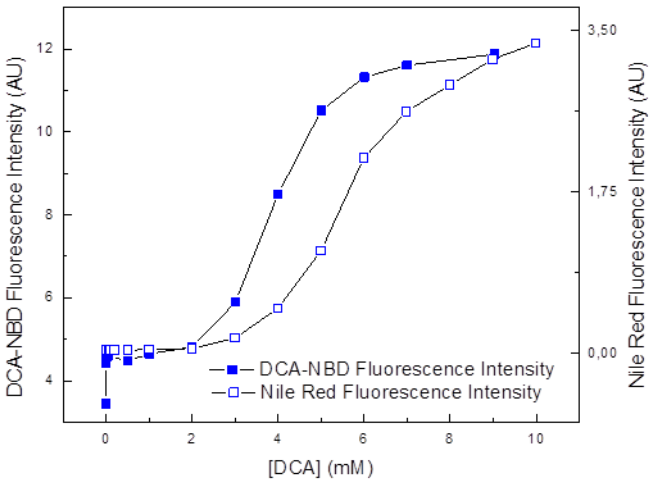

Figure 3-3 - Nile Red (open squares) and DCA-NBD (closed squares) fluorescence intensity as a function of total DCA concentration. DCA was stepwise added to 2 µM of probe solution, and fluorescence emission spectra were recorded. DCA-NBD was excited at 460 nm and emission was recovered between 480-700 nm; Nile Red was excited at 530nm and emission was recovered between 550-750 nm. Fluorescence intensities were corrected for samples dilution.

UDCA micellization

For UDCA micellization studies, UDCA was added to a 2 µM UDCA-NBD solution; from 5 µM up to ≈ 15 mM total BA. An increase in fluorescence intensity and anisotropy is observed for UDCA concentrations over 0.5 mM (Figure 3-4A). The increase in fluorescence intensity and anisotropy correlates with UDCA aggregate formation and is also accompanied by a blue-shift of the emission spectra (Figure 3-4B).

Nevertheless, this behaviour is distinct from what was seen with DCA. In this case, UDCA-NBD is sensitive to much smaller concentrations of UDCA (≈0.5 mM). Up to this concentration the sample is likely in a monomeric state. Above this concentration, the quantum yield of UDCA-NBD progressively increases until a plateau is reached around 7 mM UDCA and increases again around 9 mM UDCA.

Given that the reported values for the CMC of UDCA are within 7 to 10 mM [6,10,13], it is likely that the increase of UDCA-NBD quantum yield at low UDCA concentration corresponds to the interaction of the probe with premicellar aggregates (primary aggregates) of the BA. In this case, UDCA forms a type of aggregate which somehow shields UDCA-NBD from the solvent. A critical premicellar aggregate concentration value of 0.5 mM can be recovered from the profile (Figure 3-4A).

These aggregates increase in number and over 9 mM, large micelles are formed as typically reported in the literature. This final structure transition in aggregate properties, shields even more efficiently UDCA-NBD from the solvent. This transition is possibly associated with the formation of larger aggregates (secondary aggregates or micelles). These results fit the model for BA aggregation in a two-step fashion, proposed by Small [14].

The fluorescence intensity behaviour of Nile Red is similar to UDCA-NBD (Figure 3-5). However, the quantum yield of UDCA-NBD is also significantly more sensitive to BA

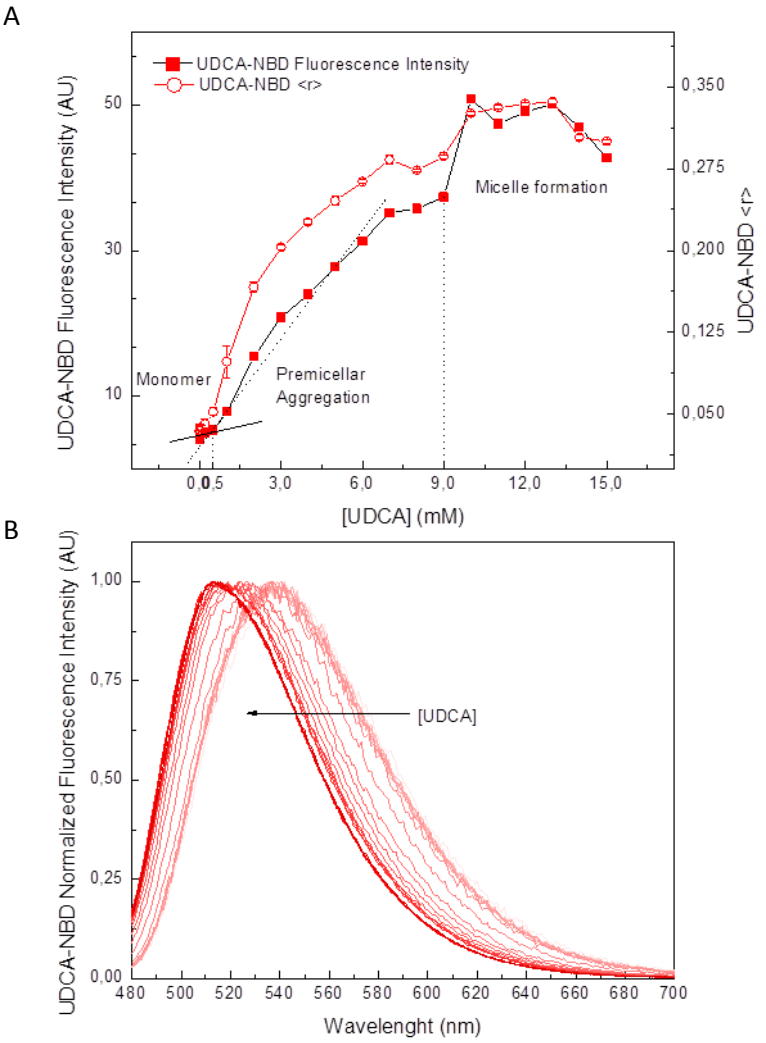

Figure 3-4 - UDCA-NBD fluorescence emission intensities, anisotropies (A) and normalized emission spectra (B) as a function of UDCA concentration. UDCA was stepwise added to 2 µM of probe solution, fluorescence emission spectra were recorded. UDCA-NBD was excited at 460 nm and emission was recovered between 480-700 nm. Fluorescence anisotropy was measured at 540nm. Fluorescence intensities were corrected for sample dilution. (A) UDCA-NBD fluorescence emission intensity (closed squares) and anisotropy (open circles) as a function of total UDCA concentration. Full black line represents the trend of the monomer fluorescence intensity signal and black dashed line represents the trend upon premicellar aggregate formation. Intersection between the two black lines is at 0.5 mM as shown by black dotted line. (B) UDCA-NBD emission spectra at several UDCA concentrations, as shown by the tendency arrow. Spectra were normalized to the value at maximum intensity.

concentration than Nile Red.

Interestingly, both probes were sensitive to the formation of premicellar or primary aggregates of UDCA, whereas these were undetected with DCA. Since DCA is in fact more hydrophobic than UDCA, it is highly unlikely that premicellar aggregates are not formed for this BA [6]. In this way, neither DCA-NBD nor Nile Red interact with DCA premicellar structures or these present significant structural differences to premicellar aggregates of UDCA. In fact, as observed from Figure 3-4B, formation of UDCA micelles is accompanied by a notable blue shift of UDCA-NBD fluorescence. This blue shift in the fluorescence emission spectra is more significant than the observed for DCA-NBD in DCA micelles (Figure 3-2B), confirming that the micelle aggregates are structurally different for these two BAs. In the case of DCA, after binding of DCA-NBD to a putative premicellar DCA aggregate, the NBD fluorophore remains fully exposed to the polar solvent, and fluorescence characteristics are unchanged.

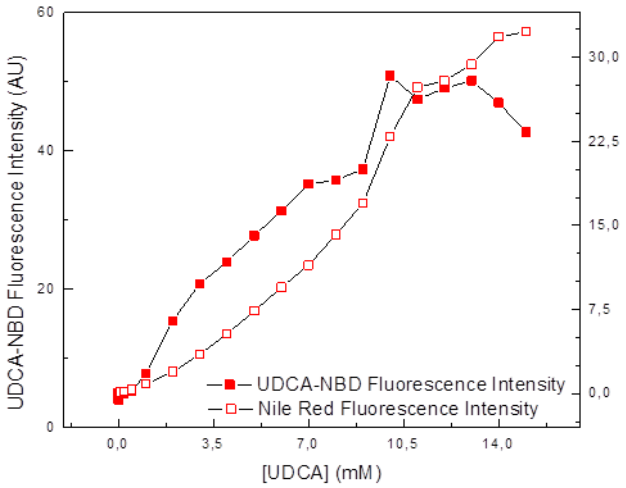

Figure 3-5 Nile Red (open squares) and UDCA-NBD (red squares) fluorescence intensity as a function of total UDCA concentration. UDCA was stepwise added to 2 µM of probe solution, and fluorescence emission spectra were recorded. UDCA-NBD was excited at 460 nm and emission was recovered between 480-700 nm; Nile Red was excited at 530nm and emission was recovered between 550-750 nm. Fluorescence intensities were corrected for samples dilution.

TUDCA micellization

TUDCA micelle formation was also studied with Nile Red, TUDCA was stepwise added to buffer containing 2 µM of Nile Red, from 5 µM to 15 mM and fluorescence emission was recorded. Nile Red fluorescence intensity was stable until 0.5 mM, and above this concentration it increased, reaching a plateau around 2 mM (Figure 3-6). Around 4 mM TUDCA, Nile Red quantum yield becomes highly sensitive to BA concentration and fluorescence intensity increased several fold. Much like UDCA; its unconjugated version, TUDCA apparently presents a two-phase behaviour with two CMCs recovered, 0.5 mM and 5 mM, corresponding to the onsets of premicellar and micellar aggregate formation.

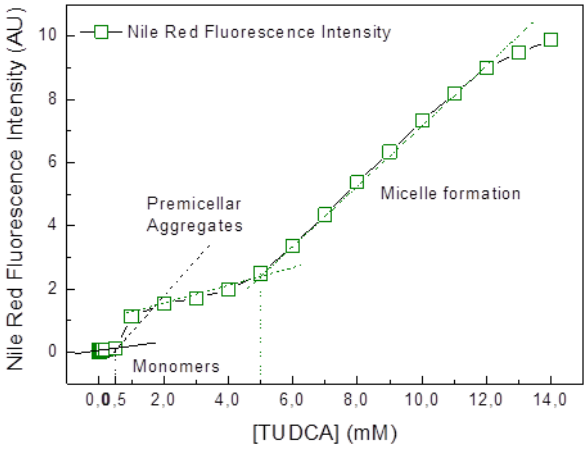

Figure 3-6 – Nile Red fluorescence emission intensities as a function of TUDCA concentration. TUDCA was stepwise added to 2 µM of Nile Red solution, fluorescence emission spectra were recorded. Lines represent the trend of the premicellar fluorescence intensity signal (full black), premicellar aggregates formation (black dashed), premicellar fluorescence intensity signal (green dotted) and micelle formation (green dashed). Intersection between the two black lines is at 0.5 mM as shown by black dotted line. Intersection between the two green lines is at 5 mM as shown by the green dotted line. Nile Red was excited at 530nm and emission was recovered between 550-750 nm. Fluorescence intensities were corrected for sample dilution.

Literature comparison

In Table 3-1, all CMCs determined above are shown, along with the values taken from the literature. CMC values varied significantly depending on the method used for micelle detection. The main difference between this study and others is that, for UDCA and TUDCA, a two-step aggregation pattern was observed.

Table 3-1 - Critical micellar concentration values for DCA, UDCA and TUDCA. Values were recovered from labelled BA or Nile Red fluorescence intensity or anisotropy curves

Bile Acid	Probe	CMC1 (mM)		CMC2 (mM)		CMC from Literature (mM)
		Φ	<r>	Φ	<r>	
DCA	DCA-NBD	2.5	2.3	-	-	2.4-4.5 [10–13,15]
	Nile Red	3.3	-			
UDCA	UDCA-NBD	0.5	0.4	9.0	8.9	7-10 [6,10,13]
	Nile Red	1.0	-	12.5	-	
TUDCA	Nile Red	0.5	-	4.7	-	2-7 [6,9,10,13,14]

The CMC value recovered for DCA is in the range from previously reported values. The 1st CMC value for both TUDCA and UDCA is approximately the same which would suggest that the first step of aggregation is independent of the taurine aminoacid. The 2nd CMC value is coherent with the notion that conjugation reduces the CMC values. Both 2nd CMC values for

UDCA and TUDCA are in the range of reported values, which possibly indicates that previous studies are only detecting the second type of UDCA and TUDCA aggregate.

The behaviour from UDCA and DCA is markedly different. For UDCA there is a gradual increase in fluorescence intensity and anisotropy from the first CMC and then after the second CMC only a short increase is perceived, whereas for DCA there is a slight increase in intensity and anisotropy after the only CMC. This might imply that the aggregation mechanisms are different for these two molecules.

The goal of these studies was to assess whether labelled BA effectively interact with unlabelled BAs and determine the onsets of premicellar aggregation. However, as discussed in the case of DCA, premicellar aggregates of this BA are possibly undetectable with this methodology. Taking that into account, a new methodology was devised to tackle this issue.

3.1.2. Critical Aggregation Concentration

In order to determine if a submicellar aggregation constant could be recovered for DCA as well, labelled BAs were added stepwise to a buffer solution and fluorescence emission spectra and anisotropy were recorded as a function of labelled BA concentration.

When DCA-NBD concentration is above 2 μM, a linear relationship between fluorescence intensity and concentration is no longer observed (Figure 3-7A). This also happens for UDCA-NBD, again over 2 μM (Figure 3-7C). The deviation from a linear behaviour means that there is formation of a species with an inferior quantum yield. This species can be aggregated DCA-NBD or UDCA-NBD. The anisotropy of neither DCA-NBD nor UDCA-NBD changes in the concentration range shown and is very small, almost zero (Figure 3-7, B and D). Anisotropy insensitivity to aggregate formation is because aggregates are *dark* or possess a very low quantum yield (they do not fluoresce and do not contribute to fluorescence anisotropy), or have an identical rotational diffusion coefficient as monomers. Additionally, in the case of aggregation, an increase in fluorescence emission anisotropy could be mitigated by fluorescence depolarization through energy migration (HomoFRET) [61].

The lifetime of labelled BAs decreases when concentration increases (Figure 3-8A). This rules out the formation of only fully *dark* aggregates (since lifetime-weighted quantum-yield would be insensitive to these species), and favours the formation of at least a fraction of aggregates with a *lower-than-monomer* quantum yield. Anisotropy decays do not change with a concentration increase (Figure 3-8B).

To test if this aggregation is due to the presence of the NBD group, a 1:1 mixture containing both labelled BA and unlabelled BA was prepared and added stepwise to buffer solution. NBD emission spectra and anisotropy were measured as function of probe concentration. If aggregation is dependent on NBD group, the overall look of the curve should be similar to the one obtained with only labelled molecule. If aggregation is based on interaction between native parts of the molecules, the curve should have the same aspect but a loss of linearity should occur for higher concentrations of labelled BA.

For DCA, almost the same profile is obtained when using the 1:1 mixture (Figure 3-7A), which means that aggregation occurs mainly between DCA-NBD monomers. As previously seen, anisotropy of DCA-NBD was invariant in the concentration range studied.

On the other hand, a great difference exists between the *pure* UDCA-NBD curve and the *mixed* UDCA-NBD curve (Figure 3-7B). With the 1:1 mixture aggregation again occurs at 2 µM; however, the intensity of the curve is higher. This means that UDCA-NBD is interacting with unlabelled UDCA and aggregation between UDCA-NBD molecules is disrupted.

Clearly labelled BAs aggregate at submicellar concentration. However, the aggregation onset was observed at much smaller concentrations than what was observed in the previous study. The differences obtained between fluorescence emission profiles with *pure* labelled BAs and *mixtures* of labelled and unlabelled BAs shows increased efficiency for labelled BA aggregation when compared to the unlabelled species.

The aggregation number of these aggregates is something these results cannot decipher.

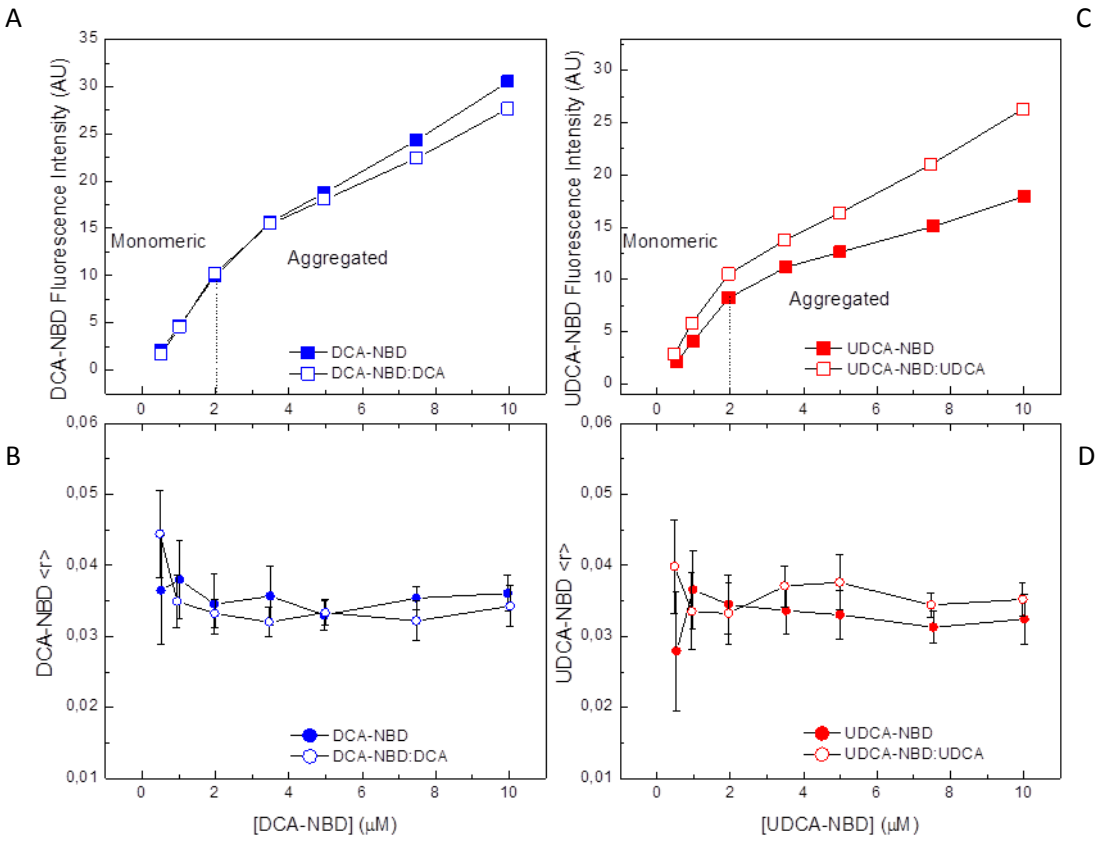

Figure 3-7 – Labelled BA fluorescence intensity emission (A, C) and anisotropy (B, D) as a function of concentration. Labelled BA only (closed symbol) or a 1:1 mixture of BA:Labelled BA (open symbol) were stepwise added to buffer and fluorescence emission spectra and anisotropy was registered. Intensity values obtained were corrected for inner-filter effects (Eq. 1). Labelled BAs were excited at 460 nm and fluorescence emission was recovered between 480-700 nm, fluorescence anisotropy was measured at 540nm. (A, B) DCA-NBD and UDCA-NBD corrected fluorescence intensity as a function of concentration, respectively. (C, D) DCA-NBD and UDCA-NBDF fluorescence anisotropy as a function of concentration, respectively.

Since anisotropies are not affected by aggregation, the aggregate number is probably small. Considering that the formation of even-numbered aggregates of BAs is more favourable [9], the observed aggregates are probably made from 2 or 4 monomers. In Figure 3-9 possible BA aggregates are represented. For quenching to happen, the NBD group would have to be in close proximity with another NBD. Notice in the first dimer how the NBD groups are apart from each other. In the second dimer, a NBD group from one of the BA in the dimer would the in close proximity with a NBD group from the other BA. This might account for the fluorescence quenching. If it is assumed that the top terminal groups do not affect the ones on the bottom, a tetramer would be indistinguishable from the second dimer (Figure 3-9). This only goes to show that the stoichiometry of the aggregate is not accessible from our results.

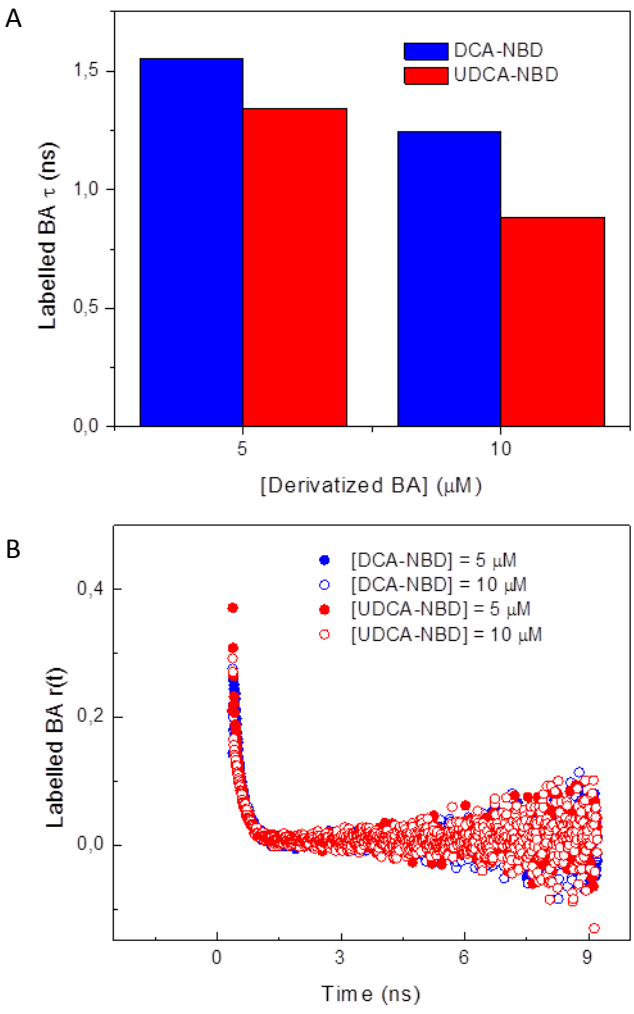

Figure 3-8 – Fluorescence lifetime-weighted quantum yield (A) and fluorescence anisotropy decays (B) of DCA-NBD and UDCA-NBD (blue and red, respectively) at 5 and 10 μM concentrations (closed and open circles, respectively). Labeled BA were excited at 340nm and emission was recovered at 540nm.

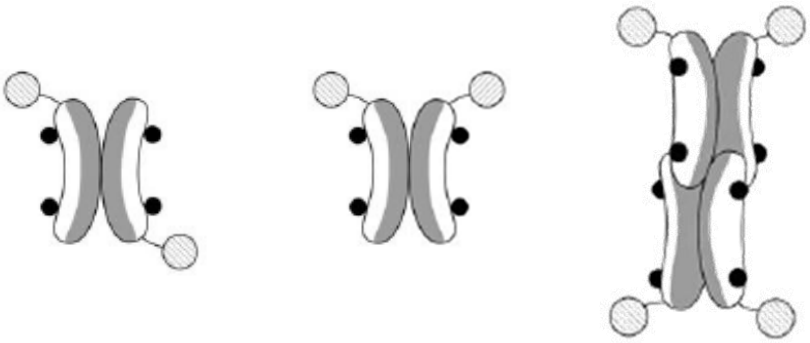

Figure 3-9 - Schematic representation of bile acid aggregates. Adapted from [8]

3.1.3. DCA-NBD interacts with unlabelled BA

One hypothesis for the cytotoxic role of DCA is its aggregation state; possibly DCA aggregates are toxic to cells. As well, hydrophilic BAs might create a hydrophobic:hydrophilic species that is less apoptotic-prone. To look for an interaction, 100 µM of UDCA and TUDCA were added to 2 µM of DCA-NBD. This concentration was chosen since as shown in Figure 3-7 no aggregation is expected for the labelled BA. Fluorescence emission intensity was recorded as a function of time.

When DCA-NBD is added to buffer, its fluorescence intensity decreases slowly (Figure 3-10). This indicates that DCA-NBD is aggregating already at 2 µM, although the decrease in fluorescence is only between 5 and 10%, and as such, aggregation should be very limited (see below). After the addition of 100 µM of hydrophilic BAs UDCA or TUDCA, the intensity of DCA-NBD changes significantly, indicating an interaction between DCA-NBD and hydrophilic BAs.

The formation of a DCA-NBD:UDCA aggregate leads to a decrease in fluorescence while the aggregate formed with TUDCA has a higher fluorescence signal. This might be explained by the quenching effect of the carboxyl group. When a DCA-NBD:UDCA complex is formed, the carboxyl group from UDCA is in proximity with the NBD group from DCA-NBD, possibly quenching its fluorescence. TUDCA, on the other hand, contains no carboxyl group, and the sulphate group is further apart from the steroid ring due to a longer side-chain. Possibly, this longer side chain does not affect the NBD group, bringing forth a DCA-NBD:TUDCA species that is more fluorescent than DCA-NBD.

In order to test if DCA-NBD interaction with hydrophilic BAs is able to change the aggregation state of DCA-NBD, the aforementioned aggregation profiles for DCA-NBD were repeated by adding labelled DCA to a 100 µM solution of either UDCA; TUDCA or DCA.

The presence of unlabelled BAs leads to an increase in DCA-NBD fluorescence intensity at concentrations of labelled BA higher than 4 µM (Figure 3-10C). This is an indication that the unlabelled BAs disrupt the formation of DCA-NBD aggregates to some extent. Possibly, since significant aggregate formation is only detected over 2 µM of labelled BA, partial disruption of DCA-NBD aggregate is only effective above this concentration.

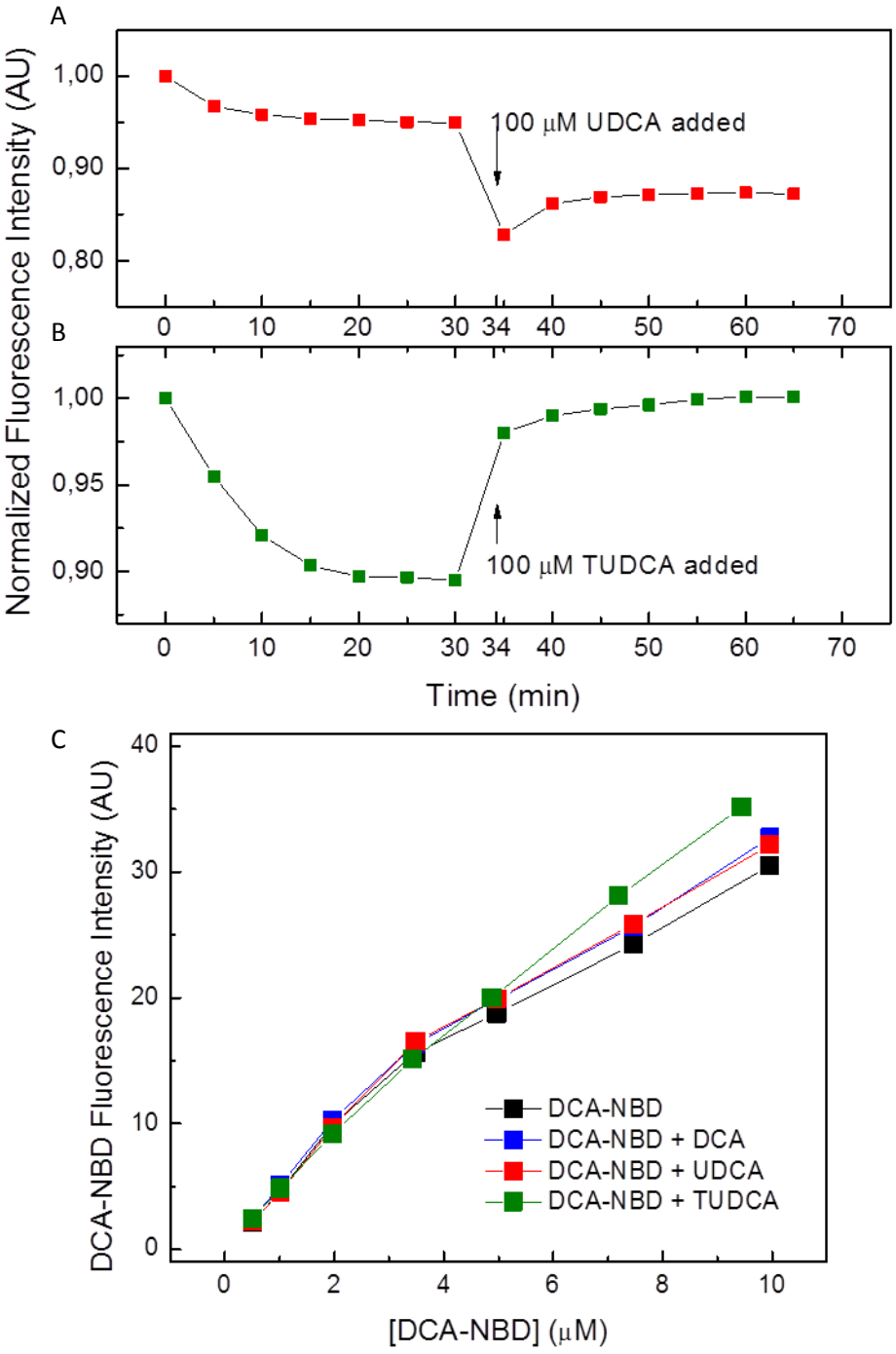

Figure 3-10 - DCA-NBD fluorescence intensity as a function of time in the presence or absence of 100 µM UDCA (A) and TUDCA (B) and aggregation profiles of DCA-NBD in the absence or presence of unlabelled DCA, UDCA and TUDCA (C). (A, B) 2 µM of DCA-NBD were incubated for 30min in the absence of hydrophilic BA. At 34min, 100 µM of UDCA (A) or TUDCA (B) were added. DCA-NBD was excited at 460nm and fluorescnce emission intensity was measured between 480-580nm, every 5min. Fluorescence intensisty is normalized for intensity at t=0min. (C) DCA-NBD was stepwise added to a buffer solution without any BA (black), or containing 100 µM of DCA (blue), or UDCA (red) or TUDCA (green). DCA-NBD was excited at 460nm and fluorescence emission intensity was recorded from 480-700nm and corrected for inner-filter effects.

Aggregation model

From these curves a simple model was developed to clarify the DCA-NBD aggregation state. In this model, monomeric DCA-NBD, mDCA*, can either interact with himself, aggregating and generating aggDCA*, or interact with unlabelled BA, forming a BA:DCA-NBD complex, BA-DCA* (Figure 3-11, Eq. 23).

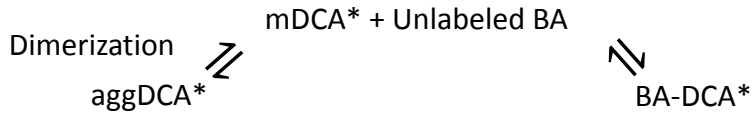

Figure 3-11 - Model for DCA-NBD interactions. Monomeric DCA-NBD (mDCA*) can either dimerize to form aggregated DCA-NBD (aggDCA*) or interact with unlabelled BA to form a BA:DCA-NBD complex (BA-DCA*)

Some assumptions are made in this model. First, since the exact stoichiometry of aggregation is unknown, the reaction mDCA*⇆aggDCA* is assumed to be a dimerization. Secondly, it is assumed that only monomeric DCA-NBD can interact with unlabelled BA.

$$[DCA^*{}_{Total}] = [mDCA^*] + 2.[aggDCA^*] + [BA - DCA^*] \quad \textbf{Eq. 23}$$

To fit the model into our data, the measured fluorescence signal is assumed to be the sum of the signal from each constituent (Eq. 24).

$$I(DCA^*{}_{Total}) = I_{mDCA*}.[mDCA^*] + I_{aggDCA*}.[aggDCA^*] + I_{BA-DCA*}.[BA - DCA^*] \quad \textbf{Eq. 24}$$

DCA-NBD only

First, the fit was made on the curve that contained only DCA-NBD. In this case no BA-DCA* was considered so the model consisted only of DCA* aggregation (Figure 3-11). In this case the observed signal is defined by (Eq. 25):

$$I(DCA^*{}_{Total}) = I_{mDCA*}.[mDCA^*] + I_{aggDCA*}.[aggDCA^*] \quad \textbf{Eq. 25}$$

$[mDCA^*]$ can be calculated through the dimerization constant (Eq. 26), with $[mDCA^*] = [DCA^*{}_{Total}] - 2 \times [aggDCA^*]$ (Eq. 24):

$$K_{dimer} = \frac{[aggDCA^*]}{[mDCA^*]^2} = \frac{[aggDCA^*]}{([DCA^*{}_{Total}] - 2.[aggDCA^*])^2} \quad \textbf{Eq. 26}$$

Solving the previous equation to $[mDCA^*]$ (Eq. 27):

$$[aggDCA^*] = \frac{-\sqrt[2]{8.K_{dimer}.[DCA^*{}_{Total}]+1}+4.K_{dimer}.[DCA^*{}_{Total}]+1}{8.K_{dimer}} \quad \textbf{Eq. 27}$$

Substituting in Eq. 24, results in (Eq. 28):

$$I(DCA^*{}_{Total}) = I_{mDCA*}.\left([DCA^*{}_{Total}] - 2.\frac{-\sqrt[2]{8.K_{dimer}.[DCA^*{}_{Total}]+1}+4.K_{dimer}.[DCA^*{}_{Total}]+1}{8.K_{dimer}}\right) + I_{aggDCA*}.\left(\frac{-\sqrt[2]{8.K_{dimer}.[DCA^*{}_{Total}]+1}+4.K_{dimer}.[DCA^*{}_{Total}]+1}{8.K_{dimer}}\right) \quad \textbf{Eq. 28}$$

The fit (Figure 3-12A) yielded an $I_{aggDCA*} = 0$ (Table 3-2), which indicates that the DCA* aggregates are non-fluorescent (*dark).* The model also retrieved a dimerization constant of $0{,}121\ \mu M^{-1}$(Table 3-2). Fit was achieved through the least square methodology. Weighting for the inverse of DCA-NBD concentration is included to achieve a higher confidence of the fit result at lower concentrations. Goodness of the fit was judged by the sum of the weighted residuals.

DCA, UDCA and TUDCA curves

Now, considering the two equilibriums simultaneously (Figure 3-11, Eq. 24), $[mDCA^*]$ can be calculated from each equilibria (Eq. 29, Eq. 30):

$$K_{dimer} = \frac{[aggDCA^*]}{[mDCA^*]^2} \Leftrightarrow [mDCA^*] = \pm\sqrt{\frac{[aggDCA^*]}{K_{dimer}}} \quad \textbf{Eq. 29}$$

$$K_{BA} = \frac{[BA-DCA^*]}{[mDCA^*].[BA_{Total}]} \Leftrightarrow [mDCA^*] = \frac{[BA-DCA^*]}{K_{BA}.[BA_{Total}]} \quad \textbf{Eq. 30}$$

where $[BA_{Free}] = [BA_{Total}]$, since $[BA_{Total}] \gg [mDCA^*]$ (Eq. 30). From these equations we obtain (Eq. 31):

$$\pm\sqrt{\frac{[aggDCA^*]}{K_{dimer}}} = \frac{[BA-DCA^*]}{K_{BA}.[BA_{Total}]} \quad \textbf{Eq. 31}$$

Isolating $[aggDCA^*]$ yields (Eq. 32):

$$[aggDCA^*] = \frac{[BA-DCA^*]^2.K_{dimer}}{K_{BA}{}^2.[BA_{Total}]^2} \quad \textbf{Eq. 32}$$

Substituting $[mDCA^*]$ (Eq. 30) and $[aggDCA^*]$ (Eq. 32) on the overall equation (Eq. 23) creates (Eq. 33):

$$[DCA^*{}_{Total}] = \frac{[BA - DCA^*]}{K_{BA}.[BA_{Total}]} + 2.\frac{[BA - DCA^*]^2.K_{dimer}}{{K_{BA}}^2.[BA_{Total}]^2} + [BA - DCA^*] \quad \textbf{Eq. 33}$$

Solving Eq. 33 to $[BA - DCA^*]$ (Eq. 34):

$$[BA - DCA^*] = \frac{[BA_{Total}].K_{BA}.\sqrt{8.K_{dimer}.[DCA^*{}_{Total}] + {K_{BA}}^2.[BA_{Total}]^2 + 2.K_{BA}.[BA_{Total}] + 1}}{4 \times K_{dimer}} - \frac{[BA_{Total}]^2.{K_{BA}}^2 + [BA_{Total}].K_{BA}}{4 \times K_{dimer}} \quad \textbf{Eq. 34}$$

The signal equation (Eq. 24) is obtained by replacing $[BA - DCA^*]$ in the following equation (Eq. 35):

$$I(DCA^*{}_{Total}) = I_{mDCA*}.\frac{[BA - DCA^*]}{K_{BA}.[BA_{Total}]} + I_{aggDCA*}.\frac{[BA - DCA^*]^2.K_{dimer}}{{K_{BA}}^2.[BA_{Total}]^2} + I_{BA-DCA*}.[BA - DCA^*] \quad \textbf{Eq. 35}$$

This equation was fitted to the data obtained with UDCA, TUDCA and DCA (Figure 3-12B-D). Previously determined values for K_{dimer}, $I_{aggDCA*}$ and I_{mDCA*} were fixed during the fit procedure. Additionally, further fitting restrictions were considered, namely that $I_{TUDCA-DCA*} \geq I_{mDCA*}$ and $I_{UDCA-DCA*} = I_{DCA-DCA*} \leq I_{mDCA*}$ as previously observed (Figure 3-10).

The model retrieved small equilibrium constants for the interaction with unlabelled BAs, one order of magnitude lower than the DCA-NBD dimerization constant (Table 3-2).

Table 3-2 - Parameters recovered for the interaction between DCA-NBD and other BAs.

Species	Interaction constant (μM^{-1})	Φ/Φ_{mDCA*}
mDCA*	-	1
aggDCA*	0.121	0
DCA-DCA*	0.004	0.55
UDCA-DCA*	0.004	0.55
TUDCA-DCA*	0.002	1

The constructed model presents one limitation, as only a dimerization step is considered in the aggregation of DCA-NBD, which is a simplification of the real behaviour of the molecule. The model retrieved an intensity signal for aggDCA* equal to zero. This would mean that the aggregates are *dark* and do not contribute to neither lifetime nor anisotropy. According to our previous results this is not absolutely true, suggesting a presence of a small population of aggregated DCA-NBD with a quantum yield higher than 0.

The model retrieved a DCA-NBD dimerization constant one order of magnitude higher than any other interaction constant. This means that DCA-NBD interacts weakly with other BA, including DCA. This is probably a consequence of charge neutralization in DCA-NBD, which removes electrostatic repulsive forces between negatively charged BAs. In this way BA-NBD are not ideal mimics of BA behaviour in solution, and we can assume the recovered values for DCA-NBD/BAs dimerization constants as the upper bound limits to the DCA-BA interaction. As such, although DCA could exhibit similar affinities for DCA itself and hydrophobic BAs (Figure 3-10), we can easily conclude from the recovered equilibrium constants (with unlabelled BAs), that in the range of BA concentration used in apoptotic studies (around 100 µM of both apoptotic and antiapoptotic BAs), the fraction of DCA in hydrophobic dimers would change from 34% to 23% in the absence or presence of hydrophilic BAs respectively. These are the upper bounds for these species assuming the aggregation constant (0.004 μM^{-1}) from Table 3-2, and as can be easily recognizable, this difference is not expected to translate into a significant change in BA activity.

The main conclusion obtained from this model is that DCA is only marginally aggregated at apoptotic concentrations and hydrophilic BAs are not expected to dramatically change the fraction of DCA in hydrophobic aggregates. This would indicate that the cytoprotective role of hydrophilic BAs is not obtained through direct interactions with DCA in solution.

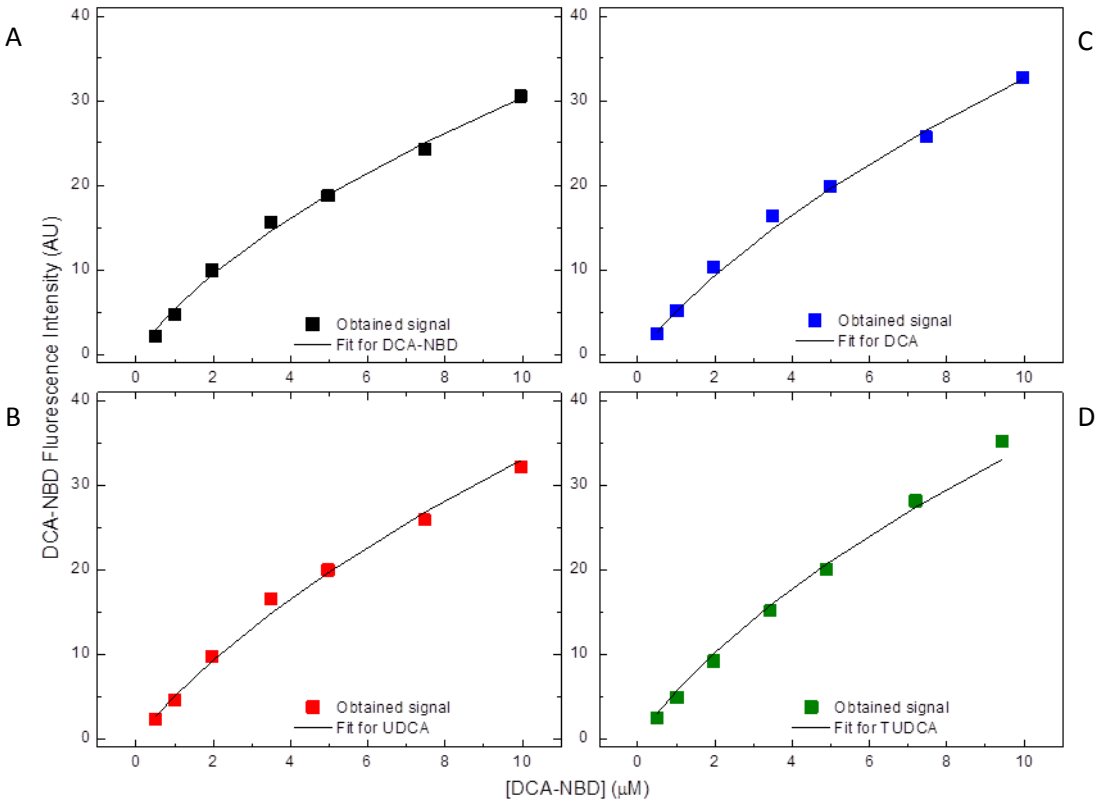

Figure 3-12 – DCA-NBD aggregation profiles and its fits obtained with the model for DCA-NBD aggregation. DCA-NBD aggregation in the absence of unlabelled BAs (A), or with 100 µM of DCA (B) UDCA (C) and TUDCA (D). Squares represent DCA-NBD fluorescence intensity (values obtained in Figure 3-10) and lines represent fitted curves with proper parameters (Table 3-2). DCA-NBD was excited at 460 and fluorescence emission measured at 480-700m.

3.2.Labelled bile acids and membranes

Since the cytoprotective role of hydrophilic BAs does not appear to be associated with solubilisation of DCA aggregates in solution, the focus will now be on the interaction of BAs with lipid membranes. The first goal is to characterize and quantify BA partition to lipid membranes with different compositions. Also, possible effects of hydrophilic BAs on DCA-NBD membrane partition at submicellar concentrations will be evaluated.

For the formation of all model membrane systems, the required amounts of POPC, Chol and PSM were used. The correct lipid concentrations for each lipid phase were taken from the phase diagram for this ternary system (Figure 3-13) [68].

3.2.1. Labelled BA partition

To assess probe partition to lipid membranes, the concentration of lipid vesicles is varied, while labelled BA concentration is kept constant at 2 µM. Labelled BA was added to the lipid vesicles and left to incubate for approximately 30min after which labelled BA fluorescence intensity and anisotropy were measured as a function of liposome concentration. After obtaining the partition curves, partition coefficients values, K_P, can be recovered through the fitting of the Eq. 13 to the data. Fitting was conducted assuming that the fluorescence emission signal in water was the signal obtained for [POPC] = 0, while values for K_P and I_L (subscript L for

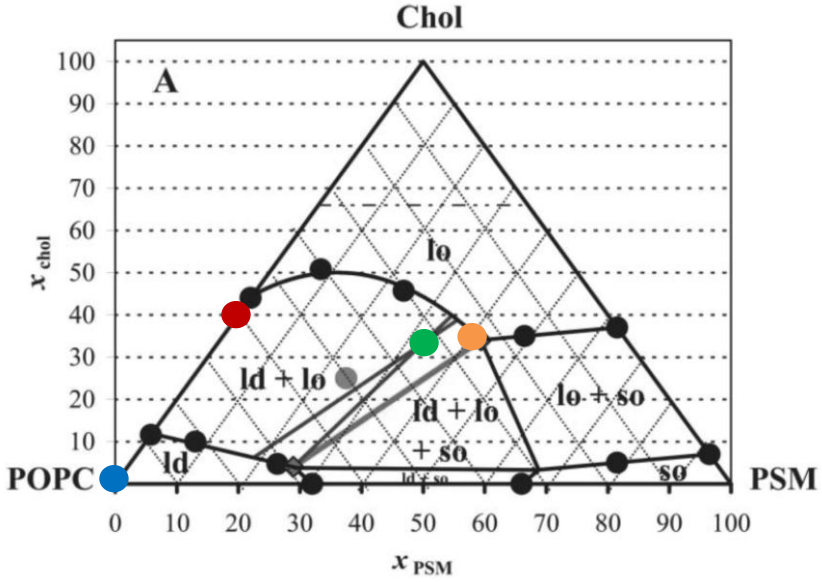

Figure 3-13 - POPC/Cholesterol/Sphingomyelin phase diagram at 23ºC. The coloured circles represent experimental conditions. Blue circle represents 100% POPC, which is in the liquid disordered (l_d) phase. Orange circle represents liquid ordered (l_o)–only vesicles, corresponding to the *lo* phase. Red and green circles represents cholesterol-rich liposomes and GUV composition, respectively, located in the region of l_d and l_o phase coexistence. Circle coordinates (POPC:Chol:PSM relative concentrations) are 100:0:0, 60:40:0, 33:33:33 and 25:35:40 for blue, red, green and orange circles respectively.

lipid) were obtained by the least-squared methodology. K_P values for membrane/water partition correspond to a quantified evaluation on the affinity of a particular molecule for lipid membranes. The affinity for lipid membranes is of great relevance in determining the pharmacological effects of a number of drugs [69]. In order to analyse membrane partition behaviour of fluorescently labelled BAs, three systems will be used. Firstly, partition to POPC-only vesicles will be assessed. Then partition to l_o-only vesicles will be quantified. To complement the aforementioned studies, imaging of DCA-NBD and UDCA-NBD in GUVs with l_o and l_d phase coexistence will be conducted.

Labelled BA partition to POPC vesicles

Labelled BA fluorescence intensity and fluorescence anisotropy increased as a function of lipid concentration for both labelled BAs (Figure 3-14). This is accompanied by a blue-shift in the emission spectra of both probes (Figure 3-15).

Recovered partitions coefficients were similar for both labelled BAs (Table 3-3). K_P from anisotropy curves were one fourth of K_P obtained from intensities. The apparent contradiction between these K_P's can be explained by the existence of Homo-FRET. When NBD molecules are sufficiently close, energy transfer can occur between them. This does not result in an intensity decrease, because molecules are identical, but in an anisotropy decrease, since the donor and acceptor molecules would have different positions in the membrane and their emission momentum would be oriented differently, leading to a less polarized emission. For high K_P's, when POPC concentration is low, fluorophore density in membrane is very high. This would lead to an increase in Homo-FRET, which would decrease as POPC concentration increases. This effect would lower anisotropy values at low POPC concentrations and would wear off for high POPC concentrations. Hence, through the anisotropy curve, labelled BA partition is underestimated, and for this reason, K_P's were always obtained from steady-state fluorescence intensities.

The anisotropy decays when lipid concentration is highest are significantly different from anisotropy decays obtained only in buffer (Figure 3-8, Figure 3-16). Namely, the fluorophore does not depolarize completely, hinting that its motion is hindered by the membrane. This means that the fluorophore does not possess a spherical, complete, liberty of motion but can only move in a restricted volume. This dynamics was modelled by Kinosita as a *wobbling-in-cone* [70]. In this model, rotation of this molecule beyond the limits of this cone is assumed to be energetically impossible. The opening, or angle, of the cone can be retrieved from the anisotropy decays through (Eq. 36):

$$r_\infty/r_0 = \left[\frac{1}{2} \times \cos\theta_{cone} \times (1 + \cos\theta_{cone})\right]^2 \qquad \textbf{Eq. 36}$$

where r_∞ is the limiting anisotropy value, r_0 is the anisotropy at time 0 ns and θ_{cone} the value of the cone angle. Values vary between 0° ($r_\infty = r_0$, no rotation during the excited state) to 90° ($r_\infty = 0$, complete depolarization during the excited state). Results obtained for DCA- and UDCA-NBD are identical, 63° and 64°, respectively (Table 3-3) and suggest that both molecules present a very similar location within the lipid membranes. Additionally, and comparing to the

published values of NBD cone angles for rotation (36-50º) obtained for a phospholipid anchored NBD (NBD-DPPE) also in l_d bilayers [71], it can be concluded that the labelled BAs are still significantly mobile. This means that NBD groups are possibly not anchored within the acyl-chains, since this would result in significantly lower rotational dynamics as seen for NBD-DPPE. These values can be compared since the average lifetimes obtained for DCA-NBD and UDCA-NBD are almost identical to the $< \tau >$ of NBD-DPPE in the same study (6.1-7.1 ns) [71].

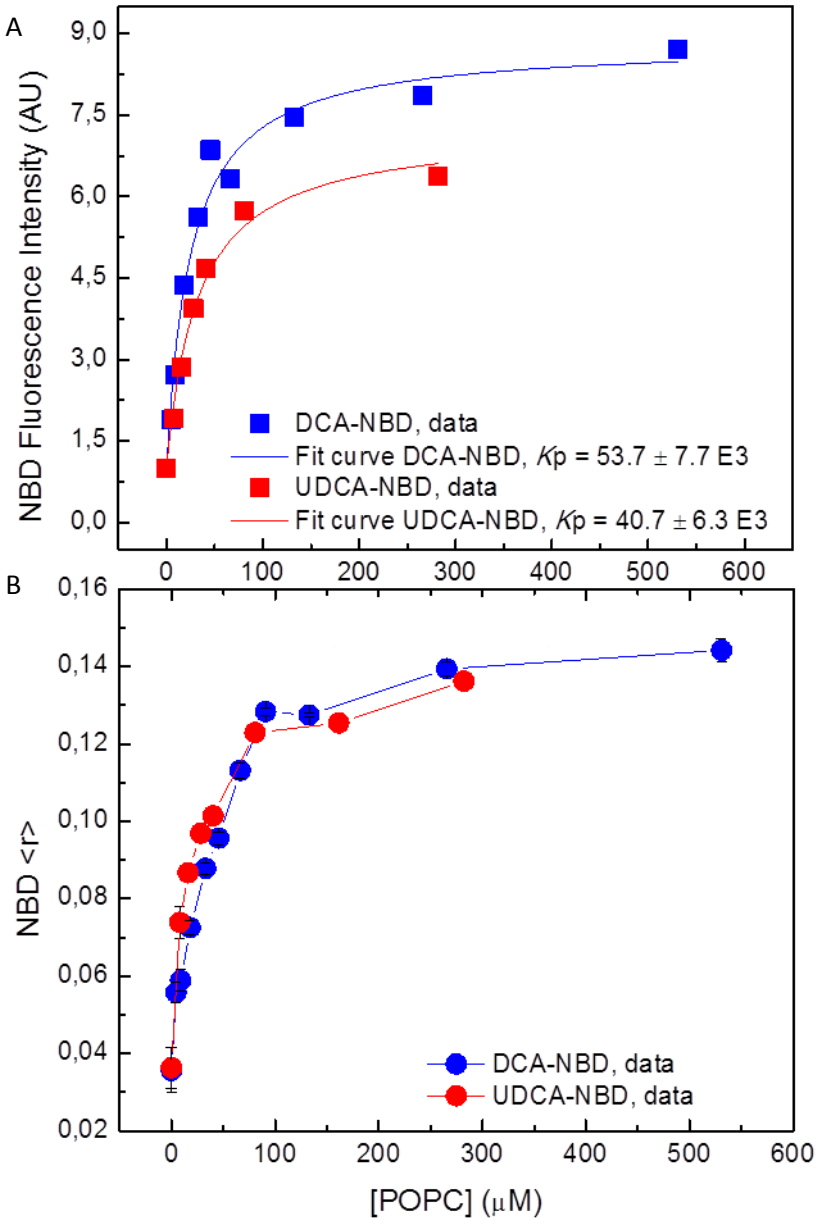

Figure 3-14 - Fluorescence intensity (A) and anisotropy (B) for DCA-NBD (blue) and UDCA-NBD (red) as a function of POPC concentration. Experimental points are displayed as squares (intensities, A) and circles (anisotropies, B). Fits are displayed by curves (same colour code) using the K_P values shown in the legend. Labelled BAs were excited at 460nm; fluorescence intensities were measured between 480-700nm and anisotropy was measured at 540nm. 2 μM of DCA-NBD were used. Fluorescence intensity values were normalized to the value at [POPC] = 0 μM.

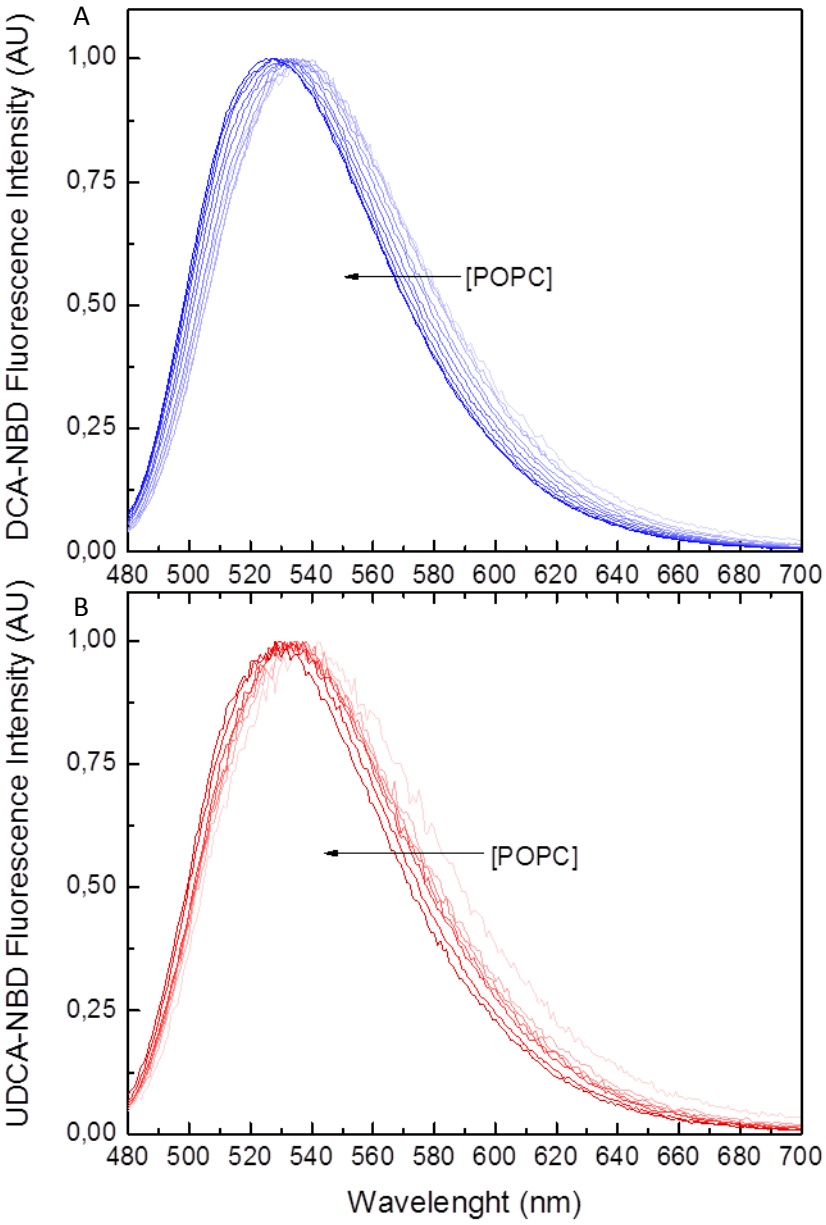

Figure 3-15 – Fluorescence emission spectra of DCA-NBD (A) and UDCA-NBD (B) shift to lower wavelengths when POPC concentration increases. POPC concrentration is indicated by the tendency arrow. Labelled BAs were excited at 460nm; fluorescence intensities were measured between 480-700nm and anisotropy was measured at 540nm.

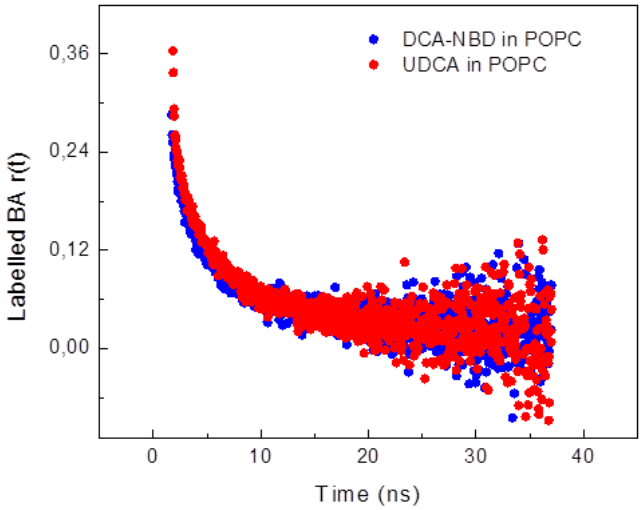

Figure 3-16 - Fluorescence anisotropy decays of DCA-NBD (blue) and UDCA-NBD (red) in POPC vesicles. 2 µM of labelled BAs were added to POPC vesicles, were excited at 340nm and fluorescence anisotropy was recovered at 540nm.

Labelled BA partition to Chol-rich vesicles

Next, the partition of labelled BAs was assessed to liposomes with a composition of POPC, Chol and PSM so that only a liquid ordered (l_o) phase is formed (Figure 3-13). This phase is characterized by a lower degree of acyl-chain dynamics and similar lateral diffusion as the liquid disordered phase [68].

Labelled BA fluorescence intensity and anisotropy increase as a function of lipid concentration for both labelled BAs (Figure 3-17). This is accompanied by a blue-shift in the emission spectra of both probes (results not shown).

For l_o vesicles, DCA-NBD partitions more effectively than UDCA-NBD. This is evident in the partition curves (Figure 3-17) and recovered parameters (Table 3-3). The K_P obtained from anisotropies in this experiment are much more alike the K_P from intensities. This is due to a lower partition and hence lower NBD densities for low lipid concentration. In these conditions, energy migration is no longer significant and partition curves present identical shapes for both anisotropies and fluorescence intensities.

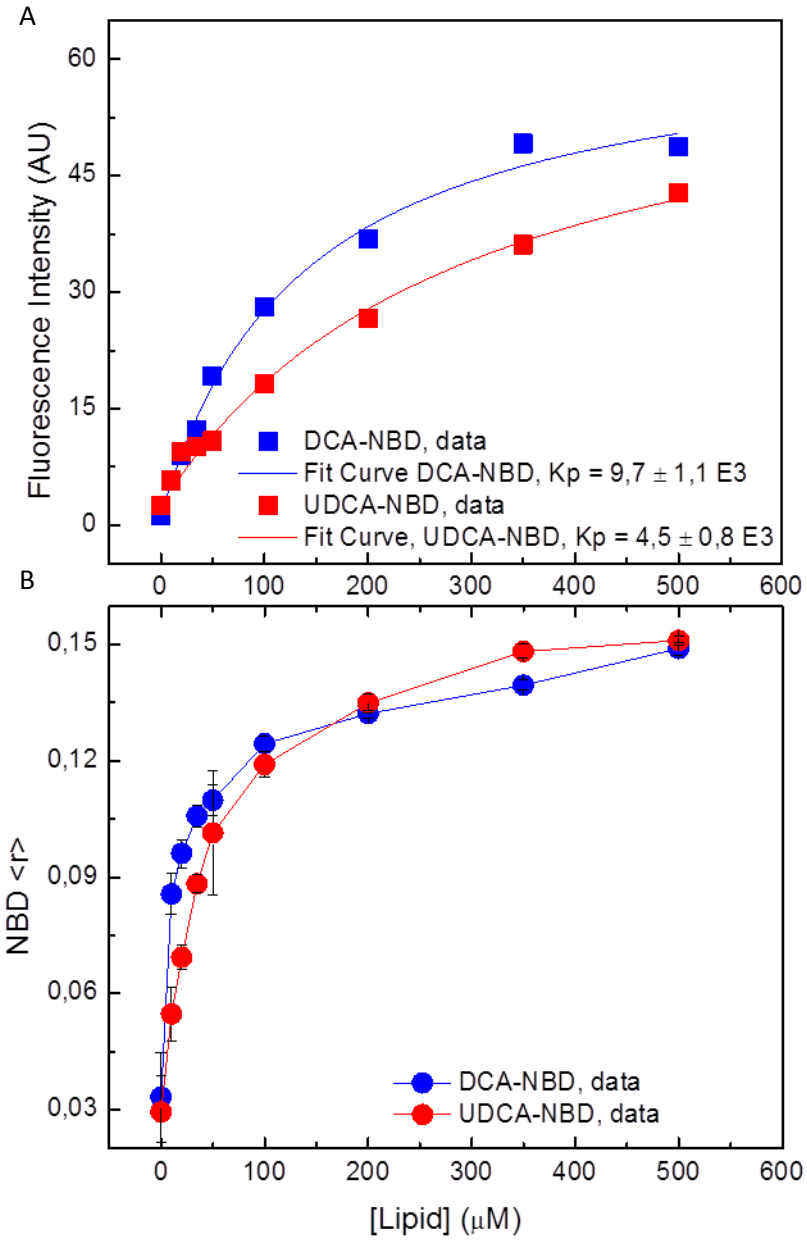

Figure 3-17 – Fluorescence emission intensity (A) and anisotropy (B) for DCA-NBD (blue) and UDCA-NBD (red) as a function of lipid concentration. Experimental points are displayed as squares (intensities, A) and circles (anisotropies, B). Fits are displayed by curves (same colour code) using the K_P values in legend. Labelled BAs were excited at 460nm, fluorescence intensities were measured between 480-700nm and anisotropy was measured at 540nm. 2 μM of DCA-NBD were used, and l_o vesicles were formed using 25% POPC: 35% Chol: 40% PSM (mol/mol). Fluorescence intensity values were normalized to the value at [Lipid] = 0 μM.

Comparing partitions, $K_P(l_d,l_o)$

Having a K_P for l_d and another for l_o, a $K_P(l_d,l_o)$ can be calculated. This $K_P(l_d,l_o)$, is the ratio between $K_P(l_d)$ and $K_P(l_o)$, and reflects the relative affinity of labelled BAs to the l_d and l_o lipid membrane phases (Eq. 37). For this calculation it was assumed that labelled BA would partition equally to POPC-only-l_d phase and a POPC:Chol:SM-l_d phase.

$$K_P(l_d, l_o) = \frac{K_P(l_d)}{K_P(l_o)} \qquad \textbf{Eq. 37}$$

The obtained $K_P(l_d,l_o)$ shows that if there is phase coexistence, labelled BA would preferably partition to the l_d phase (Table 3-3). This is in agreement with previous results, that showed that taurine-conjugated BA partition less to Chol-rich membranes and also that the most hydrophobic BAs were less affected by higher membrane order [46].

One interesting result is that the fluorescence anisotropy of both labelled BAs in the lipid membrane is similar for both l_d and l_o membrane phases (Table 3-3). The main distinction between l_d and l_o phase is their rigidity, being l_o the more rigid of the two. It appears that the rotational dynamics of the NBD group is insensitive to rigidity of the phase they are partitioning to. This suggests that the NBD group in BA-NBD is not on the inside of the membrane but at the lipid/water interface.

Table 3-3 – Partition coefficients and labelled BA fluorescence lifetimes, steady-state anisotropies and rotation cone angles (according to [70] **in lipid membranes.**

Labelled BA	*Lipid phase*	K_P (10^3)	$K_P(l_d,l_o)$	$\langle r \rangle_L$	θ (°)	$\bar{\tau}_L$ (ns)	$\langle \tau_L \rangle$ (ns)
DCA-NBD	l_d	53.9±7.7	5.5±1.0	0.15	63	5.4	6.6
	l_o	9.7±1.1		0.14	-	-	-
UDCA-NBD	l_d	40.9±6.3	9.1±2.2	0.14	64	5.3	6.7
	l_o	4.5±0.8		0.16	-	-	-

To have a better appreciation of the different partition to l_d and l_o phase, GUVs with phase coexistence were electroformed. In this way, the preferable partition of labelled BA can be observed. In this experiment, Rhodamine-DOPE (Rho-DOPE, Table 2-1) was used to label the l_d phase within the GUVs. The l_o phase within the GUVs could not be labelled since this typically requires NBD-DPPE, which would interfere with the signal from NBD-labelled BA.

GUV z-stack images were taken to construct 2D maximum intensity projections (Figure 3-18). Since GUVs are spherical, 2D projections appear as a circle. l_o phase is unlabelled and shows up as dark regions in the projection.

Once again, a clear l_d preference is observed as the signal from the NBD channel co-localizes with the signal from the Rhodamine channel (Figure 3-18). The overlay is merely a superimposition of images from both channels and is meant to serve as a guide.

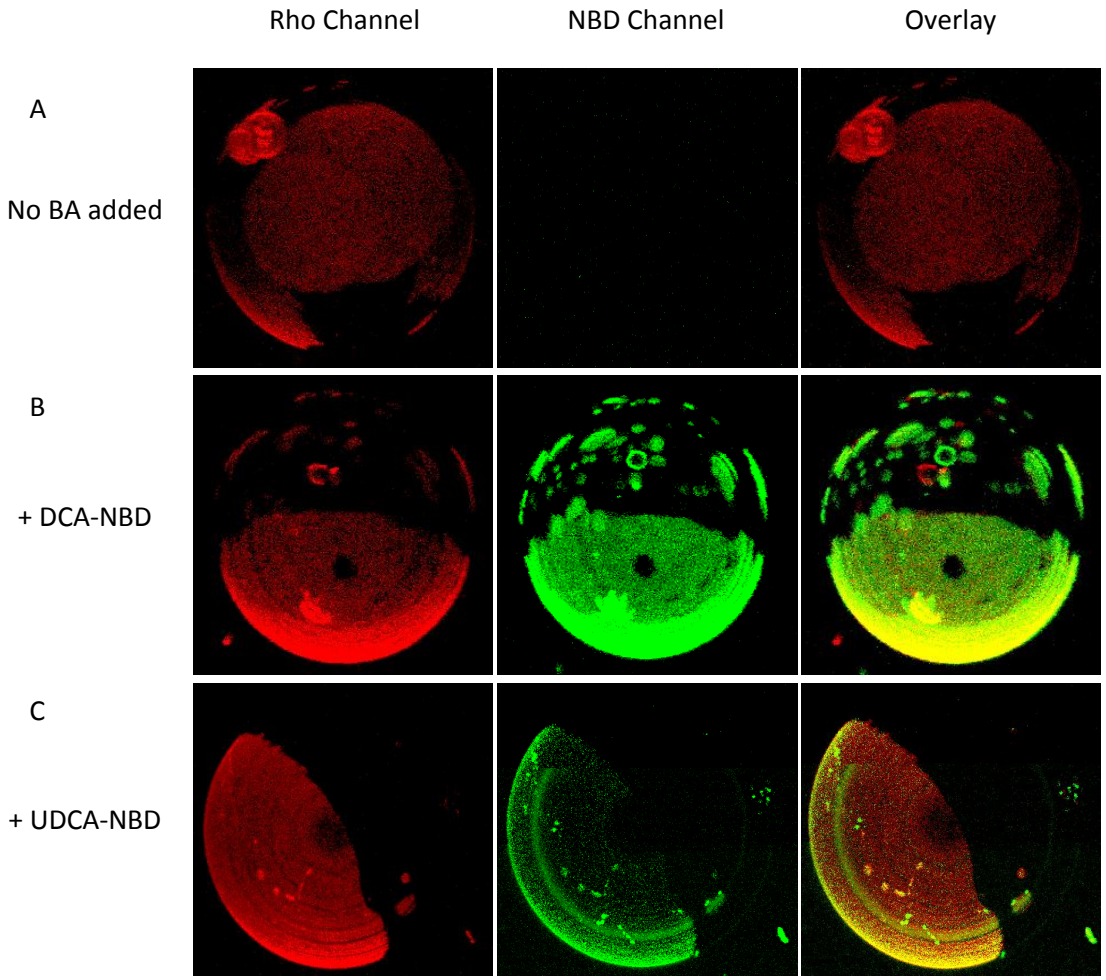

Figure 3-18 - Maximum intensity projections of Rho-DOPE labelled GUVs incubated with or without DCA-NBD or UDCA-NBD. Immobilized GUVs (composition POPC:Chol:PSM 1:1:1 (mol/mol/mol) were labelled with Rho-DOPE at a ratio of 1/500, biotinylated lipid DPPE-biotin was included at total lipid ration of $1/10^6$. Fluorescence from Rho (red) and NBD (green) channel was sequentially collected and projections for the entire GUV are shown for GUVs in the absence of labelled BAs (A) or in the presence of 20 µM of DCA-NBD (B) and UDCA-NBD (C). Overlay is simply a superimposition of the Rho and NBD channel and is meant to serve as a guide.

ITC experiments

When constructing a fluorescent derivate of a molecule, the main concern is to lessen the disturbance in the original molecule. The l_d preferable partition of labelled BA is a signal that the driving force behind partition is not the NBD group but the biliary domain of the molecule.

Isothermal titration calorimetry was thought to be able to measure the partition of both labelled and unlabelled BAs. However, BA partition to model membranes is a process that does not release a significant amount of heat. A signal could not be measured until BA concentration was raised to millimolar levels. In this regime, vesicle interaction became noticeable but the registered signal could not be related to partition. In normal ITC studies of partition, exothermic spikes are registered [66], while in this experiment, with 1 mM of DCA, endothermic spikes were observed (Figure 3-19). This is not a partition event and is most likely associated with disassembly of aggregated DCA dissolution upon membrane binding. This result is indicative that BAs bind to lipid membranes mostly through adsorption rather than incorporation in acyl-chains, since the latter is expected to be highly exothermic [66].

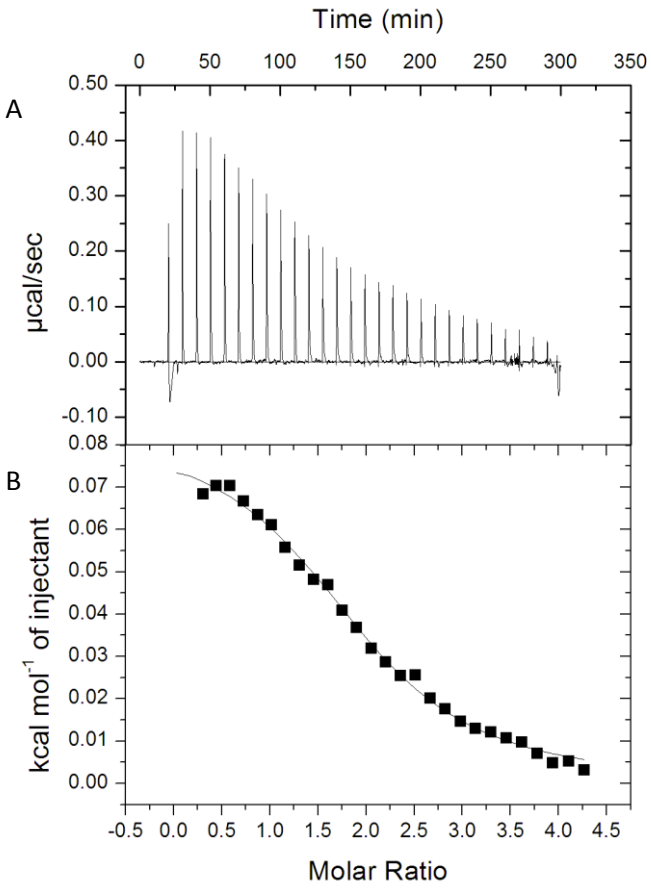

Figure 3-19 – Titration of DCA (1 mM) with LUVs composed of POPC (20 mM) in buffer. (A) Obtained thermogram was integrated to yield the heat of reaction for each injection (B). Experiment was performed by titrating 10 µL aliquots of liposomes into a BA solution in the sample cell.

Conclusions

These results show that labelled BAs efficiently interact with membranes, while both hydrophobic and hydrophilic BAs exhibited preferential partition to l_d phase in the presence of l_o domains. However, DCA-NBD partition coefficient to the l_o phase is two times larger than the K_P for UDCA-NBD. Additionally, since NBD anisotropy is practically the same in l_d and l_o, a superficial location for the fluorophore is assumed.

From the ITC experiment, it can be understood that BA partition to membranes is a *low-energy* event, possibly associated with an adsorption of BAs to the bilayer rather than insertion in the membrane interior. The differential affinity of labelled BAS to lipid membranes depending on the lipid phase would then be associated with different packing densities at the membrane surface, which could modulate BA adsorption.

The high partition coefficients determined for the labelled BAs in the liquid disordered phase reinforces the idea that BA actions could be based on membrane altering effects. In apoptotic assays, DCA concentration is typically at 100 μM. In the case of total partition of the BA to the plasma membrane, a very high density of DCA is expected at the membrane surface with possible consequences for membrane structure. This will be the subject of the studies presented in Section 3.3.

3.2.2. The effect of hydrophilic bile acid on DCA-NBD partition

One possible mechanism for the cytoprotective role of hydrophilic BAs would be the prevention of DCA partition to lipid membranes, preventing hydrophobic BA effects on membranes. To test for this effect, DCA-NBD partition to POPC vesicles was assessed after vesicles were incubated overnight with hydrophilic BAs. 2 μM of DCA-NBD were then added to the vesicles and DCA-NBD partition was assessed by fluorescence intensity, anisotropy and lifetime. Two concentrations of hydrophilic BA were used, 10 and 100 μM.

DCA-NBD partition seems to be unaffected by previous vesicle incubation with hydrophilic BAs as fluorescence lifetime partition curves obtained are independent of hydrophilic BA concentration (Figure 3-20). Although the recovered K_P values vary from the control value, these are always within error. Also, anisotropy decays obtained using the highest POPC concentration were independent of hydrophilic BA concentration.

This result clearly proves that neither UDCA nor TUDCA have an effect on DCA-NBD partition to lipid membranes.

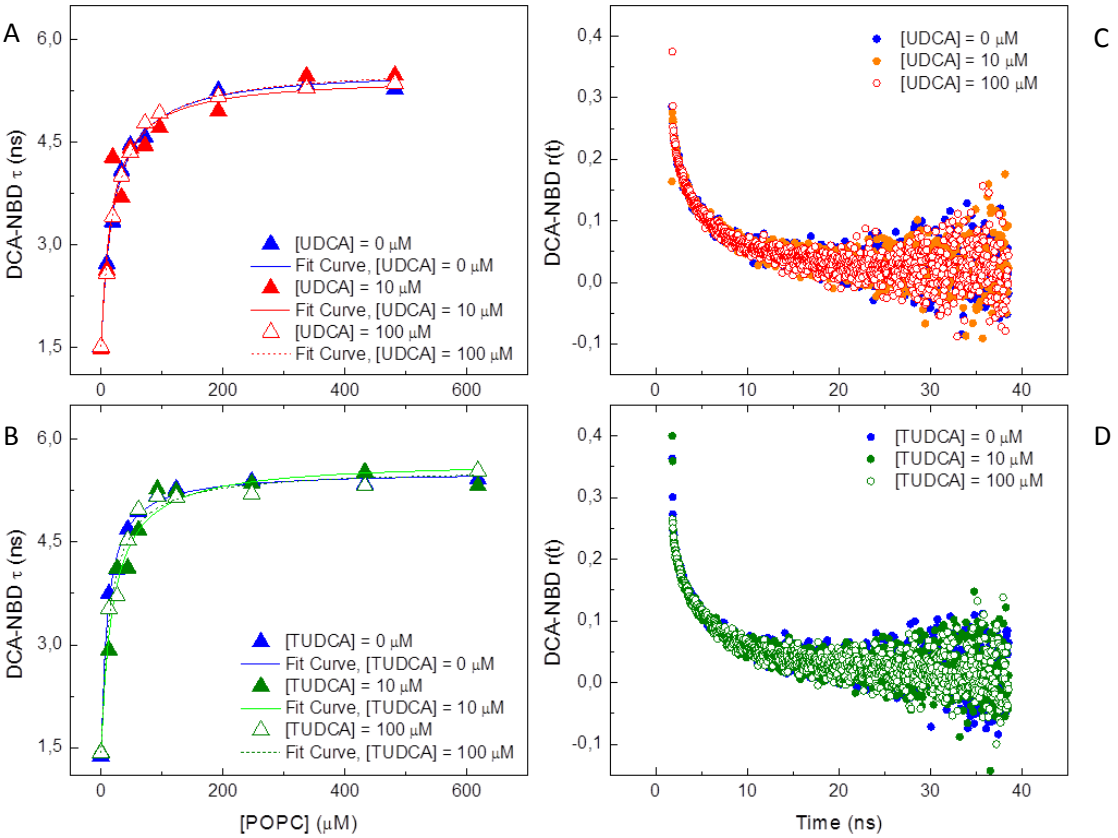

Figure 3-20 – DCA-NBD fluorescence lifetime-weighted quantum yield as a function of POPC concentration, and DCA-NBD fluorescence anisotropy decays at the highest POPC concentrations for several hydrophilic BA concentrations. (A, C) DCA-NBD fluorescence lifetime-weighted quantum yields Experimental data and fits are displayed as symbols and lines respectively. Blue line and symbols when no hydrophilic BA is added and red or green for incubation with UDCA or TUDCA, respectively. Closed and open symbols refer to incubation with 10 or 100 μM incubation with unlabelled BA, respectively. DCA-NBD was excited at 340nm and fluorescence emission decays were obtained at 540nm.

3.3.Unlabelled bile acids and labelled-liposomes

Previously, it was shown that hydrophilic BA interaction with DCA was very limited and did not affect its partition to POPC membranes. However, it is possible that both hydrophobic and hydrophilic BAs affect membrane biophysical parameters in opposing ways. One might hypothesize that besides apoptosis being triggered by a direct effect of hydrophobic BAs on the lipid bilayer, the observed cytoprotective effect of hydrophilic BAs could be associated with a direct influence on the biophysical properties of the lipid membrane. After this effect, the membrane becomes *DCA-insensitive* and apoptosis would not triggered.

In order to test for specific effects of BAs on membrane biophysical properties, several standard membrane probes will be used, each probing for one membrane biophysical parameters (Table 2-1).

3.3.1. Bile acid location on model membrane systems

Firstly, DPH and TMA-DPH were used. Both fluorescent probes are widely used to report membrane fluidity as their fluorescence anisotropy is extremely sensitive to membrane composition and order [58,68]. Three different lipid mixtures were used: only POPC; 60:40 POPC:Chol (mol/mol); and 33:33:33% POPC:PSM:Chol (mol/mol/mol) (Figure 3-13). Preformed liposomes were incubated overnight with up to 100 μM of DCA, UDCA and TUDCA. DPH and TMA-DPH anisotropy was measured as a function of BA concentration.

No fluorescence anisotropy variation is observed for both DPH and TMA-DPH (Figure 3-21). One possible explanation for the absence of membrane perturbation by unlabelled BAs would be a lower partition coefficient for these species than what was previously calculated for labelled versions (Table 3-3). Importantly, the studies with unlabelled BAs were conducted at a very high concentration (100 μM), while partition studies with labelled BAs were performed at 2 μM. These two concentrations are likely to correspond to completely different aggregation states for the molecule, and BAs, when added to liposomes at high concentrations, do not associate as monomers (as already observed from ITC data, Figure 3-19). In this case, these aggregates do not fully dissociate after association with the lipid membrane, consequently, effects on the lipid membrane will be mainly local, and a large fraction of the membrane will remain unperturbed. Alternatively, the aggregation of BAs might stabilize the fraction of BAs not associated with lipid membranes, decreasing membrane/water partition coefficients. Both of these phenomena are able to explain the absence of membrane perturbation by BAs added to preformed liposomes.

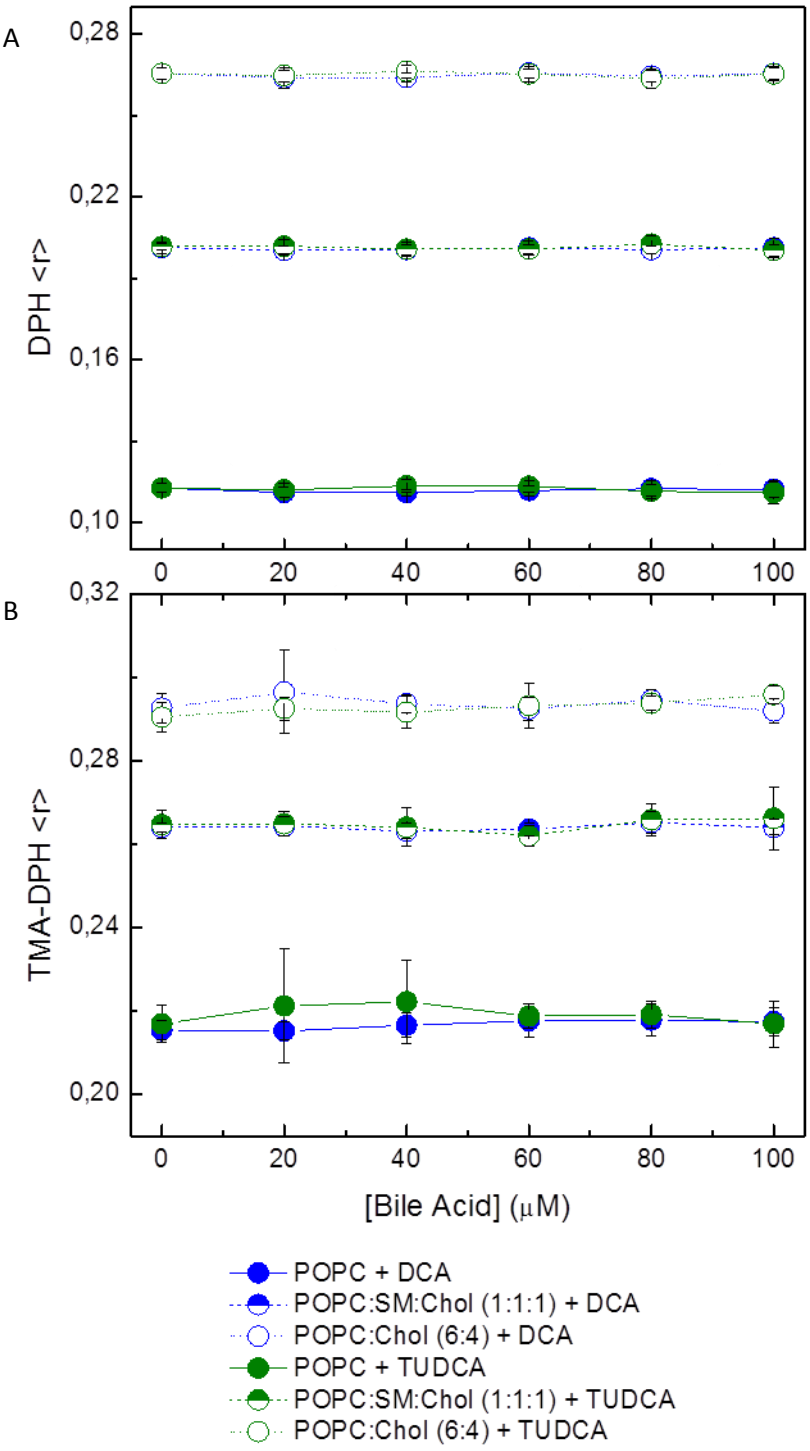

Figure 3-21 - DPH (A) and TMA-DPH (B) fluorescence anisotropy as a function of BA concentrations for various lipid compositions. 100 µM of DPH-labelled (A) or TMA-DPH-labelled (B) lipid vesicles containing either only POPC (full lines and symbols), 33:33:33 POPC:Chol:PSM (mol/mol/mol) (dashed lines and half-open symbols) or 60:40 POPC:Chol (mol/mol) (dotted line and open symbols) were incubated overnight with either DCA (blue) or TUDCA (green). Both probes were excited at 340nm and fluorescence anisotropy was measured at 430nm. Probe/lipid ratio used was 1/200.

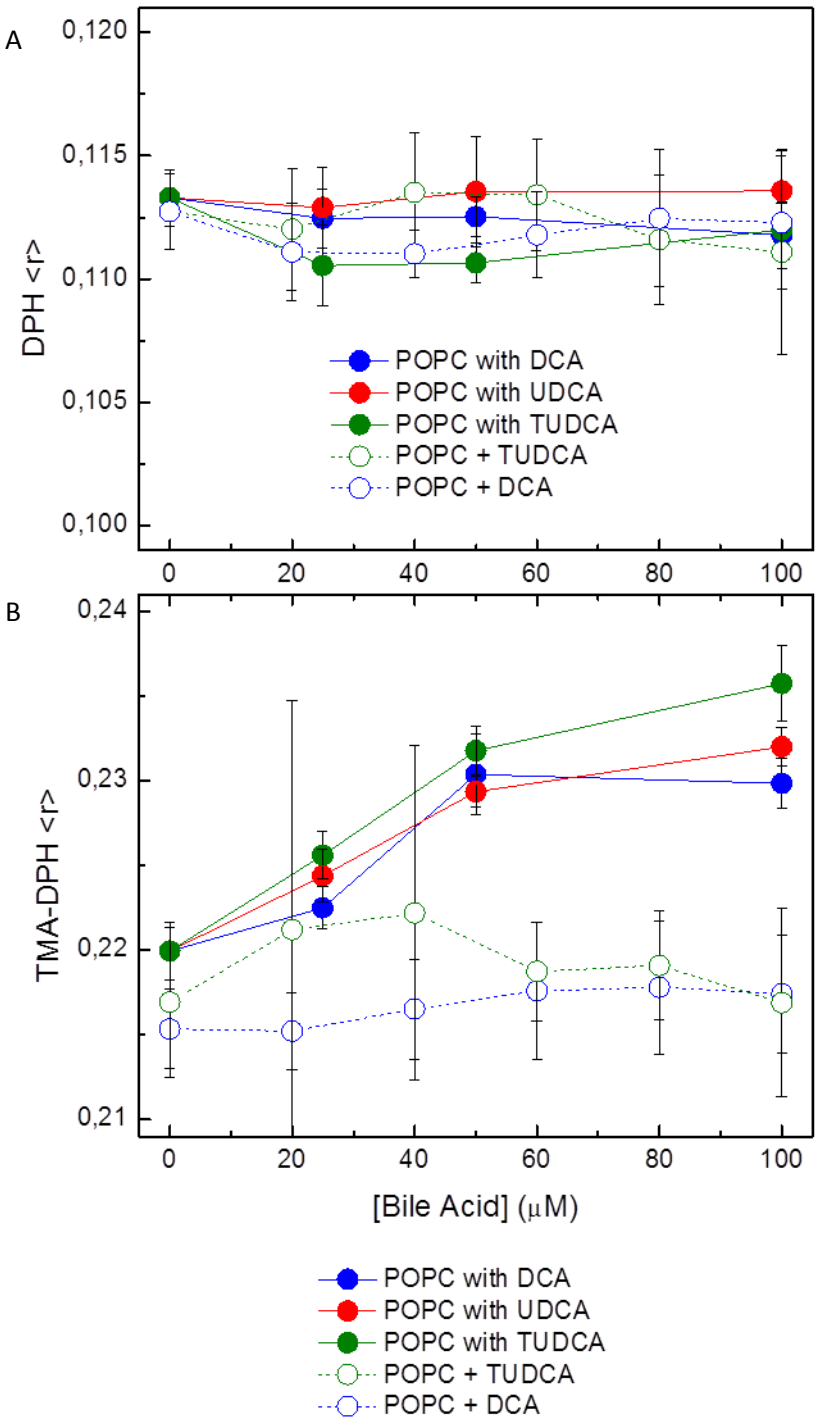

Figure 3-22 - DPH (A) and TMA-DPH (B) fluorescence anisotropy in POPC vesicles as a function of BA concentrations for various preparation methodologies. 100 μM of DPH-labelled (A) or TMA-DPH-labelled (B) lipid vesicles containing only POPC were incubated overnight with various DCA or TUDCA concentrations (dashed lines and open symbols, blue and green respectively, called "POPC with…"). 100 μM of DPH-labelled (A) or TMA-DPH-labelled (B) lipid vesicles containing only POPC were cosolubilized with various DCA, TUDCA and UDCA concentrations (full lines and closed symbols, blue, green and red respectively, called "POPC +…"). Both probes were excited at 340nm and fluorescence anisotropy was measured at 430nm. Probe/lipid ratio used was 1/200.

To confirm that the absence of membrane partition was caused by BA aggregation in solution, BAs were cosolubilized with lipids and membrane probes before liposomes formation. The advantage of cosolubilization is that added components are immediately solubilized by lipids and aggregates are not formed in solution. Using this methodology with POPC liposomes, DPH and TMA-DPH fluorescence anisotropy was measured as a function of BA concentration.

DPH anisotropy continues to be insensitive to all BAs (Figure 3-22A). However, TMA-DPH anisotropy increases significantly when BAs are cosolubilized along with the liposomes (Figure 3-22B). Insensitivity of DPH and sensitivity of TMA-DPH to cosolubilized BAs indicates that BAs are found only at the membrane surface, and acyl chain fluidity is unaltered.

To confirm a superficial location of BAs on the membrane, another membrane probe was used. Di-4-ANEPPDHQ is sensitive to membrane potential [72,73]. BAs were added to preformed ANEPPDHQ-labelled liposomes or cosolubilized with membrane components.

When BAs are added to preformed liposomes labelled with ANEPPDHQ, no fluorescence intensity variation is seen (Figure 3-23), as had been previously observed for DPH and TMA-DPH (Figure 3-21). However, when DCA is cosolubilized with the liposomes, ANEPPDHQ fluorescent intensity varies significantly (Figure 3-23).

Clearly, BAs are in fact aggregating when added to preformed liposomes. These aggregates either partition less than monomers or remain stable after membrane association, affecting the membrane surface only locally. It is highly likely, that *in vivo*, the presence of a

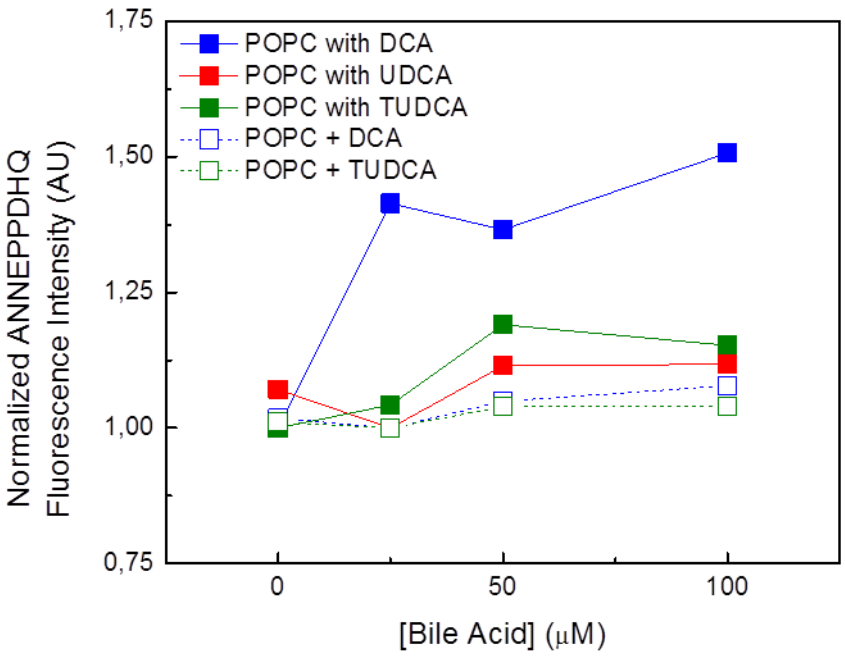

Figure 3-23 - ANEPPDHQ fluorescence intensity as a function of BA concentration, added to preformed POPC liposomes and incubated overnight (dashed lines and open symbols) or cosolubilized with liposomes (full lines and closed symbols). DCA, UDCA and TUDCA are represented as blue, red and green, respectively. ANEPPDHQ was excited at 470nm and fluorescence emission was measured at 500-800nm. Probe/lipid ratio used was 1/200.

large concentration of proteins and different membrane components contribute to the solubilisation of these aggregates, and effective partition to membranes is in this way achieved.

Since partition of BAs in vitro is limited by aggregation of the molecules before membrane interaction, higher concentrations of BAs were used to probe for modulation of membrane biophysical properties. In this way, BA concentration was raised to 500 μM while keeping lipid concentration at 200 μM. Unlabelled BAs were then added to preformed liposomes labelled with ANEPPDHQ and its lifetime was measured. However, at such high concentrations of BAs, membrane solubilisation cannot be discarded. To test for this unwanted effect, DPH-labelled liposomes were subjected to the same treatment as ANEPPDHQ liposomes.

It was observed that ANEPPDHQ lifetime increases significantly when liposomes were incubated with all BAs (Figure 3-24A). The increase was greater when DCA was added, in agreement with previous results (Figure 3-23). However, both hydrophilic BAs also increased the membrane probe fluorescence lifetime. This is a clear sign of interaction between BAs and liposomes.

Since DCA and hydrophilic BAs produced different effects on ANEPPDHQ lifetime, a co-incubation of liposomes with hydrophilic BA + DCA (500 + 500 μM) was performed. Hydrophilic BAs and DCA were added simultaneously.

When liposomes were incubated with both DCA and hydrophilic BAs, ANEPPDHQ lifetime increases in a cumulative way, so that after co-incubation, differences in fluorescence lifetimes were the sum of the effects of DCA plus the hydrophilic BA used (Figure 3-24A). When UDCA was added, fluorescence lifetime increased by 0.085 ns and when DCA is added, fluorescence lifetime increased by 0.185 ns. Incubation with both resulted in a fluorescence lifetime increase of 0.27 ns (equal to 0.085 + 0.185). In this way, hydrophilic BAs do not prevent DCA-induced changes on ANEPPDHQ fluorescence.

These results (Figure 3-24A) could potentially be explained by membrane solubilisation or intercalation by BAs at these high concentrations. Noticeably, ANEPPDHQ fluorescence anisotropy decays are insensitive to the presence of BAs (Figure 3-24B). On the other hand, DPH fluorescence anisotropy in the presence of the high BA concentration is only slightly affected and decreased by 10% (Figure 3-24C). This decrease is very small and cannot be associated with vesicle solubilisation, as DPH in micelles typically presents fluorescence anisotropy values of 0.10-0.12 [74–76]. In fact, the decrease in DPH anisotropy is at least partially associated with an increase in DPH lifetime. This would allow for a longer depolarization time, which would lower anisotropy [61].

Overall, these results clearly indicate that liposomes were still intact after BA treatment, and that both environments which ANEPPDHQ and DPH are probing remain almost dynamically unchanged in every experimental condition. Since BAs are unable to intercalate between lipids and to induce membrane solubilisation at 500 μM, the increase in fluorescence lifetime observed for ANEPPDHQ is likely associated with a decrease in membrane hydration due to high levels of BA partition.

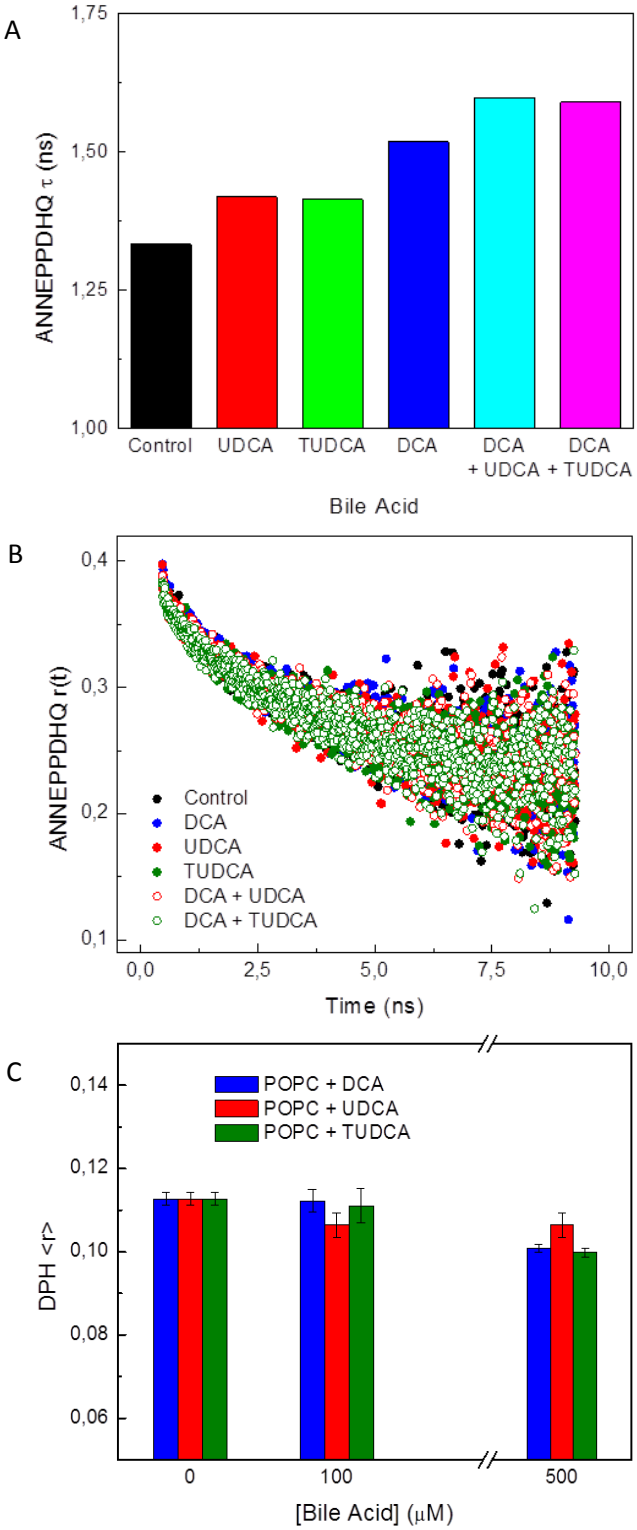

Figure 3-24 - ANEPPDHQ fluorescence lifetime-weighted quantum yield (A) and fluorescence anisotropy decay (B) and DPH anisotropy (C) in POPC liposomes after incubation with 500 µM of BA or 500 DCA + 500 µM hydrophilic BAs. (A, B) 500 µM of BAs were incubated overnight with ANEPPDHQ-labelled liposomes. No BA (black), 500 µM of DCA, UDCA or TUDCA (blue, red or green, respectively) or 500 + 500 µM of DCA plus UDCA or TUDCA (light blue and pink in (A) and open red and green in (B), respectively) were added to liposomes. ANEPPDHQ was excited at 460nm and emission was recovered at 590nm. (C) DCA, UDCA or TUDCA (blue, red, green, respectively) were added to POPC liposomes and incubated overnight. DPH was excited at 340nm and fluorescence anisotropy was recovered at 430nm. Probe/lipid ratio used was 1/200

In summary, TMA-DPH and ANEPPDHQ are clearly sensitive to cosolubilized BAs, particularly DCA. Considering that DPH is located in the membrane interior and that both TMA-DPH and ANEPPDHQ are located in the membrane surface, the putative location of BA is on the membrane surface (Figure 3-25). These results are in full agreement with data obtained for labelled BAs.

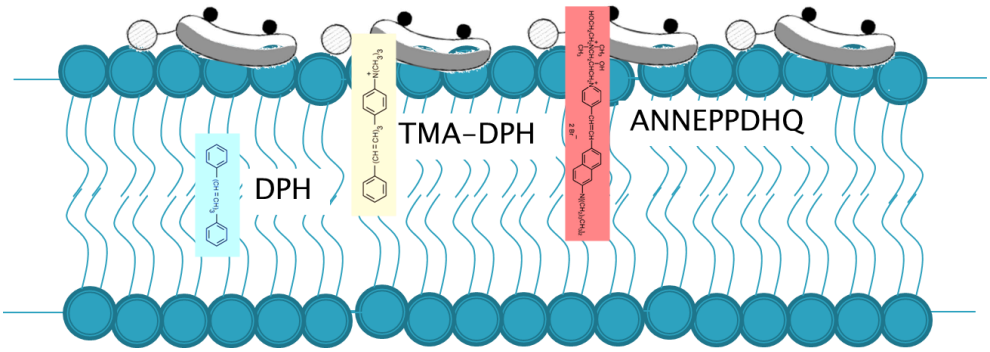

Figure 3-25 - Schematic representation of membrane probe and possible BA location in the membrane. Phospholipids in dark blue, DPH in light blue, TMA-DPH in yellow and ANEPPDHQ in red. BAs are displayed as grey/white/black molecules.

3.3.2. The effect of Chol on bile acids

Several papers have been written on the role of Chol in the interaction between BAs and vesicles. Some suggested that BAs and Chol compete for the same position in the membrane [46,47] while others showed BA depend on membrane Chol to exert their role *in vivo* [54]. Here, the effect of BAs on membrane biophysical properties was assessed using several Chol mixtures of POPC:Chol (Figure 3-26). DPH was used to label the liposomes and its steady-state anisotropy

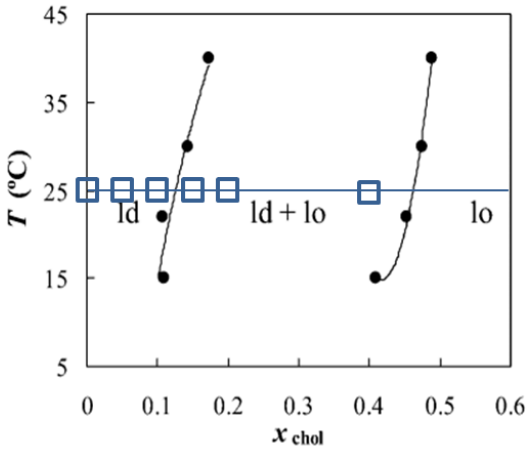

Figure 3-26 - POPC:Chol phase diagram. Mixtures with 100:0, 95:5, 90:10, 85:15, 80:20 and 60:40 POPC:Chol (mol/mol) were used. According to the lever rule, POPC:Chol mixtures are constituted by 9, 24 and 82% l_o when the fraction of Chol is 15, 20 and 40%, respectively.

was measured as a function of Chol concentration.

As Chol content is increased, DPH anisotropy values also increased, suggesting a tighter packing of the lipids in the membrane (Figure 3-27A). Liposome incubation with either UDCA or TUDCA did not induce any change in DPH anisotropy (Figure 3-27A).

However, when DCA was added, DPH anisotropy decreased significantly (Figure 3-27A). Membrane fluidity was only sensitive to DCA when Chol was present and was larger for 20%

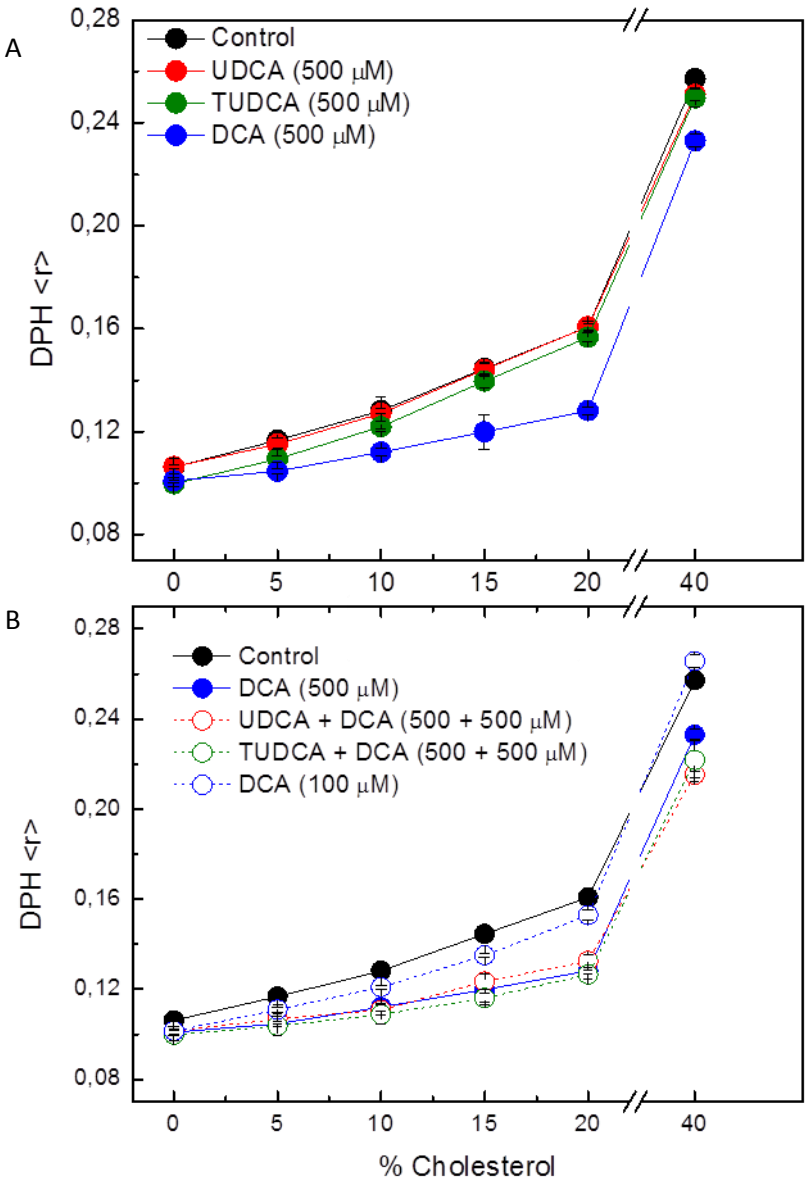

Figure 3-27 - DPH fluorescence anisotropy as a function of Chol concentration for different BA incubated overnight. DPH labelled liposomes were incubated overnight with 100 or 500 µM of DCA (open blue, closed blue symbols, respectively) or 500 µM of UDCA and TUDCA alone (closed red and green symbols, respectively) or 500 µM of UDCA or TUDCA followed 8h of 500 µM of DCA incubation (open red and green symbols, respectively). Liposomes are composed of POPC:Chol at 100:0, 95:5, 90:10, 85:15, 80:20, 60:40 (mol/mol). DPH was excited at 340nm and fluorescence emission measured at 430nm. Probe/lipid ratio used was 1/200.

Chol. When liposomes with 80:20 POPC:Chol (mol/mol) liposomes are incubated with DCA, DPH anisotropy is the equal to the value with 90:10 POPC:Chol (mol/mol) control liposomes (no BA incubation). At 40% Chol, DPH anisotropy increased, approaching values obtained for the control. In this way, considering that the latter composition of corresponds almost to 100% l_o phase, DCA is inert for l_o membranes but inhibits the rigidifying effect of Chol in l_d phases. This effect cannot be associated only by a decrease in l_o domain formation since it is observed at Chol concentrations for which the l_o phase is not formed (5 and 10% Chol, Figure 3-26).

For this effect to occur, high concentrations of DCA are needed since 100 μM of DCA produces near-control values for DPH anisotropy (Figure 3-27B). Also, co-incubation of vesicles with UDCA or TUDCA plus DCA does not prevent the effect of DCA (Figure 3-27B).

One possible explanation for this effect is that BAs remove Chol from membranes, since significant changes in membrane fluidity are only observed in the presence of Chol.

To test if membrane fluidity changes in the presence of DCA were due to Chol sequestration from the membrane, a fluorescent Chol analogue, dehydroergosterol (DHE) was used [77–79]. Unlike other fluorescent sterols [80], the behaviour of this molecule in lipid membranes has great similarity to Chol [79]. POPC-only liposomes labelled with DHE were incubated overnight with 100 μM of DCA, 500 μM of DCA, UDCA or TUDCA. Coincubations with hydrophilic BAs plus DCA were also performed. As a control, DHE (in the absence of liposomes) was also added to 500 μM of DCA to register the signal of complete DHE removal. DHE fluorescence in 500 μM of DCA (in the absence of liposomes) is nearly 10% of its value in vesicles, indicating that removal could be followed by intensity variations (Figure 3-28). However, when BAs were added to membranes, no loss in fluorescence intensity was observed. This means that no BA can remove DHE from liposomes, which indicates that DCA is not removing membrane Chol.

A decrease in DPH fluorescence anisotropy induced by DCA could be caused by an increase in the lifetime by DPH. With this in mind, both fluorescence intensity and fluorescence anisotropy decays of DPH were obtained from liposomes with 0, 20 and 40% Chol after incubation with 500 μM DCA.

Clearly, DPH lifetime were not affected by DCA incubation in the presence of Chol (Figure 3-29A). However, DCA is noticeably interfering with the rotational dynamic of DPH, affecting both the rotation cone angles [70] (Figure 3-29B) and the anisotropy decay of DPH (Figure 3-29C). The fluorescence anisotropy decay of DPH with 20% Chol and 500 μM DCA is almost identical to the decay obtained with 0% Chol in the absence of BA incubation.

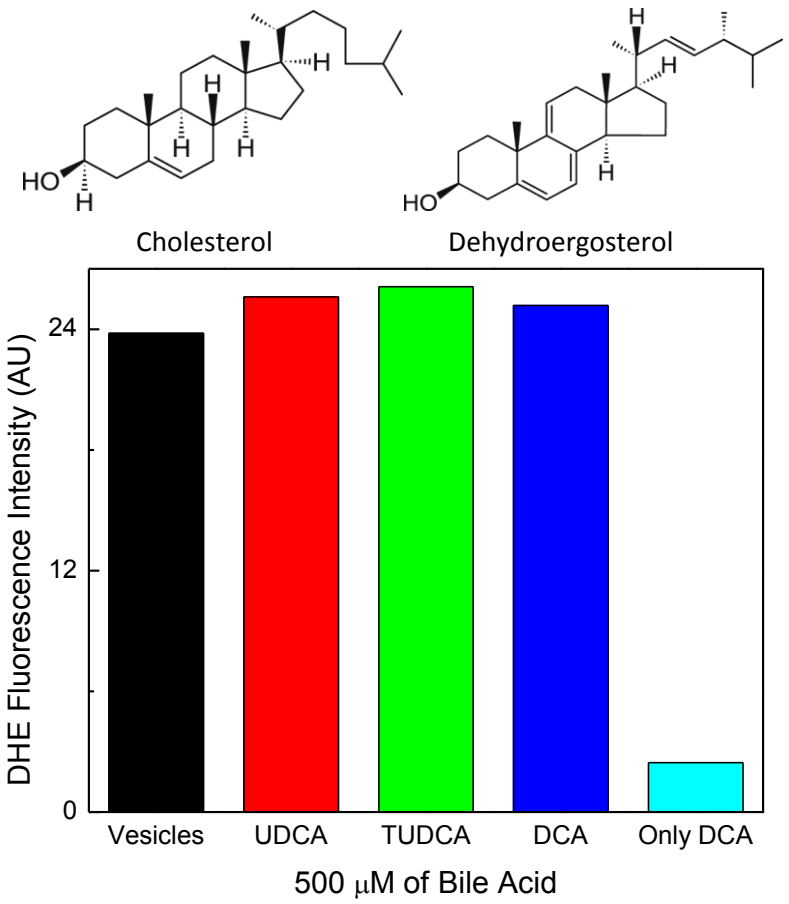

Figure 3-28 - Dehydroergosterol fluorescence intensity in liposomes incubated with and without 500 μM BA. DHE labelled liposomes were incubated with 500 μM of BA overnight. DHE was added to 500 μM solution of only DCA and incubated overnight. DHE was excited at 280nm and fluorescence intensity measured at 320nm. Probe/lipid ratio used was 1/200

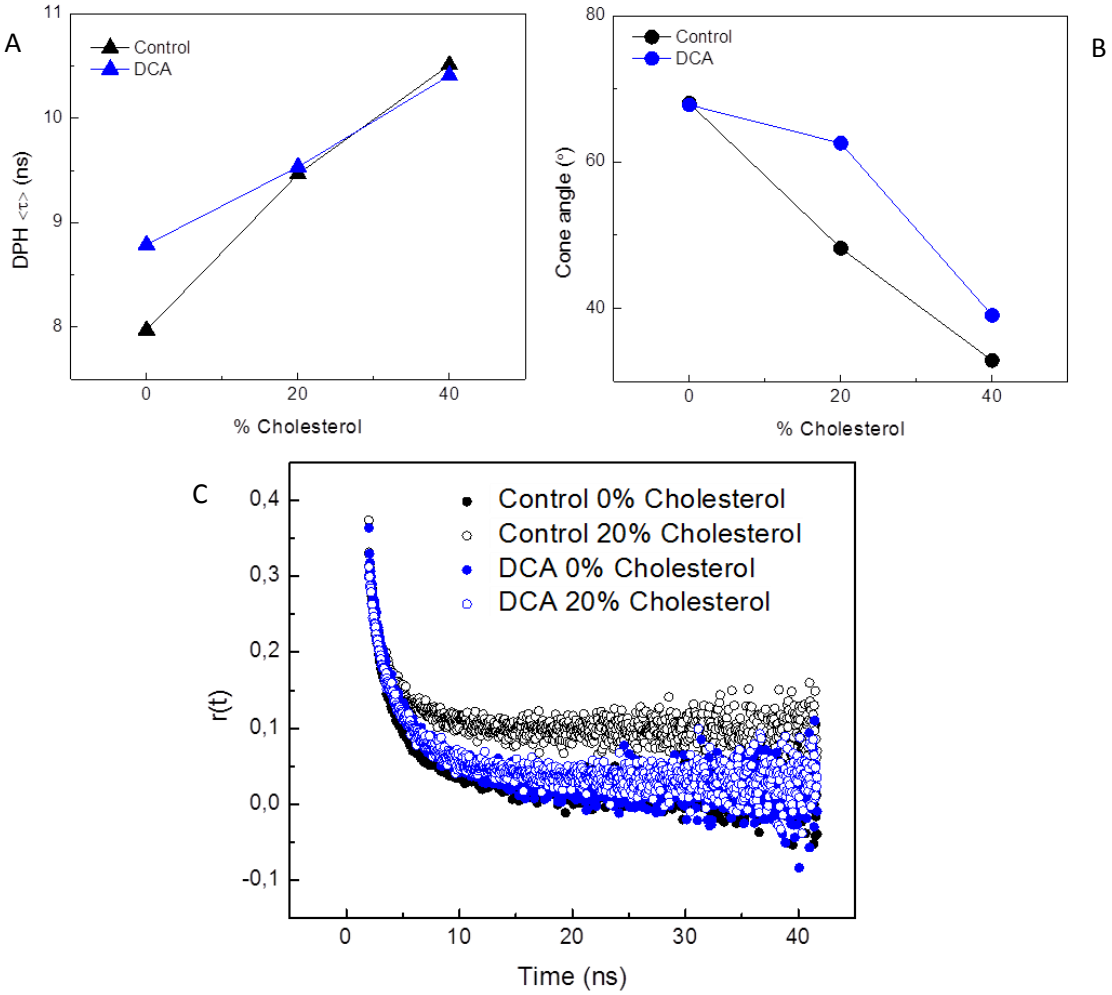

Figure 3-29 - Average lifetimes (A), cone angles according to [70] **(B) and anisotropy decays of DPH as a function of membrane Chol content in the absence or presence of 500 µM of DCA. DPH labelled liposomes were incubated overnight without any BA (control) or with 500 µM of DCA. DPH was excited at 340nm and fluorescence intensity was measured at 430nm. Probe/lipid ratio used was 1/200.**

FRET experiment

It was shown that DCA can dramatically affect the biophysical properties of Chol containing membranes. It is possible that DCA is in fact changing the phase diagram of the POPC:Chol mixture and altering the formation of l_d and l_o domains.

Firstly, a simple experiment was devised: GUVs containing 58% l_o phase were formed. An immobilized GUV was selected and imaged before and after BA addition. In this experiment, Rhodamine-DOPE (Rho-DOPE) was used to label the l_d phase within the GUVs and NBD-DPPE to label the l_o phase within the GUVs (Table 2-1). GUV z-stack images were taken to construct 2D maximum intensity projections to assess domain size and distribution.

After the addition of 500 µM of DCA no noticeable changes in domain size was observed (Figure 3-30). Noticeably, during incubation with DCA, the l_d domain, labelled red, shifted to the bottom hemisphere of the GUV and the proportion of l_d in the GUV increased from 40% in the

absence of DCA to 44% in the presence of DCA. This increase in l_d percentage is within error of the measurement. In this way, if DCA induces changes in the phase diagram of POPC:Chol:PSM they are very subtle and this methodology lacks the resolution to detect them.

To probe for domain size redistribution below the resolution limit of the confocal microscope, a FRET experiment was devised. Lipid domain sizes at the nanometer scale can be assessed through a FRET experiment. Using as FRET pairs Rho-DOPE (acceptor) and NBD-DPPE (donor), measured FRET efficiency can be related to domain size. These two labelled phospholipids exhibit completely distinct partition behaviour in lipid membranes with l_d and l_o phase coexistence. FRET between the two molecules is dramatically reduced when large domains are formed, as FRET events between NBD-molecules in the l_o phase and Rho-DOPE species in the l_d phase become irrelevant. However, for small sized domains (below 75 nm for this FRET pair), FRET events between the two lipid phases become more frequent and FRET efficiencies increase as the average domain size decreases up to 20 nm, when FRET efficiencies are undistinguishable from a homogeneous mixture [81].

Making use of the theoretical model for FRET efficiency between donor and acceptor in two planes (as the headgroup regions of each monolayer can be considered) it is possible to determine both the FRET efficiency for the case of a homogeneous distribution of donors and

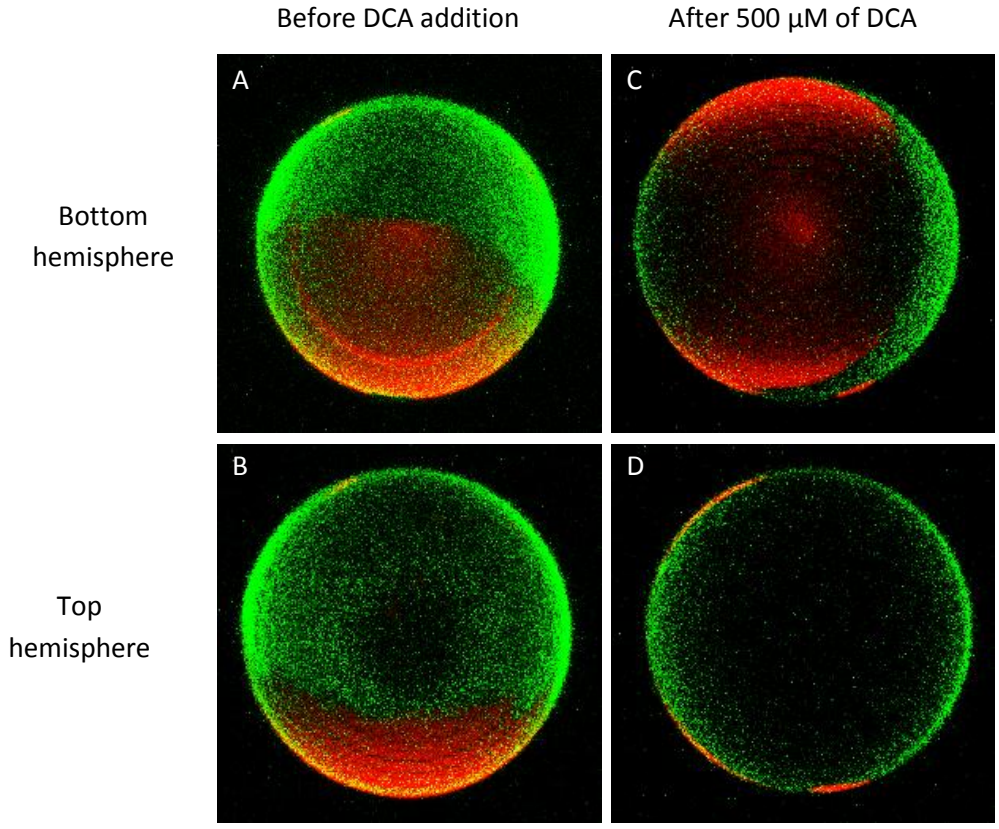

Figure 3-30 – Projections of the same GUV before (A, B) and after (C, D) 500 µM DCA incubation. GUV with POPC:Chol:PSM 45.1:25:29.9 (mol/mol/mol), 58% l_o, was labelled with Rho-DOPE and NBD-DPPE at a ratio of 1/500 and 1/200 respectively, biotinylated lipid DPPE-biotin was included at a ratio to total lipid of $1/10^6$ to achieve immobilization. Immobilized GUV was imaged before and after addition of 500 µM of DCA. Fluorescence from Rho (red) and NBD (green) channel was sequentially collected and projections for the top and bottom hemisphere of the GUV are shown for GUVs in the absence (A bottom, B top) and presence (C bottom, D top) of DCA.

acceptors (no domains or domain size < 20nm) and the case of infinite phase separation (domains > 75nm) (Eq. 18-Eq. 20). Using this methodology, de Almeida and coworkers [74], followed changes in domains sizes along a tie-line, within the l_d/l_o phase coexistence region of the phase diagram for the POPC:Chol:PSM mixture. These authors found that l_o domains are very small (< 20nm) for low l_o fractions and increased in size for higher l_o content [74].

Here, that study is reproduced with the same lipid mixture after incubation with BAs. 5 different lipid compositions were chosen so that liposomes with 0, 26, 58, 86 and 100% of l_o phase were obtained (Table 3-4). Liposomes were labelled either with NBD-DPPE (donor) or with both NBD-DPPE and Rho-DOPE (donor + acceptor). These were either incubated overnight in the absence (control) or in the presence of 500 μM DCA. Fluorescence intensity emission spectra and donor fluorescence lifetime were measured as a function of % l_o. FRET efficiencies were calculated using donor lifetime variation (Eq. 17)

The calculated FRET efficiencies are always higher for the control group than for liposomes incubated with DCA (Figure 3-31). In this system, a decrease in FRET efficiencies can be attributed to 3 possible causes: i) decrease in donor quantum yield; ii) changes in domain sizes; iii) increase in total surface area.

A decrease in donor quantum yield results in lower R_0 values (Eq. 15), and hence lower FRET efficiencies. In fact, a 10% decrease in the quantum yield of NBD-DPPE in 0% l_o is observed after DCA incubation (Table 3-4). From Eq. 15, this decrease results in a decrease of the R_0 for Rho-NBD FRET pair from 50 Å (in the absence of DCA) to 49 Å. According to Eq. 18, Eq. 19 and Eq. 20, for a random distribution of donors and acceptors, these Förster radii would lead to FRET efficiency values of 0.60 and 0.58, respectively. Additionally, quenching of NBD-DPPE is less effective for the remaining lipid compositions (Table 3-4). Clearly, the decrease in donor quantum yield, although relevant, is not responsible for the decrease in FRET efficiencies after DCA incubation.

Table 3-4 – Composition of lipid mixtures used in the FRET experiment, % l_o formed and effect of DCA on NBD-DPPE lifetime

%POPC (mol)	%Chol (mol)	%PSM (mol)	% l_o	$\bar{\tau}_{DCA}/\bar{\tau}_{Control}$ of NBD-DPPE without acceptor
71.6	5	23.3	0	0,90
59.7	14	26.3	26	0,96
45.1	25	29.9	58	0,96
34	33.3	32.7	86	0,95
25.4	39.8	34.8	100	1,01

Concerning changes in domain size, it seems unlikely the DCA has any effect. DCA reduces FRET efficiencies for every lipid mixture in the tie-line, including when no phase separation is expected to occur, 0% l_d or 100% l_o. Additionally, FRET efficiencies also decrease after DCA incubation in POPC only liposomes where phase separation does not occur (Figure 3-31).

In this way, and by elimination of alternatives, the increase in membrane surface area by BA binding to the membrane is the most likely interpretation for the FRET data. After DCA interaction with the membrane surface, it can intercalate with the headgroups of the lipids and separate them, expanding the membrane. In this way, every lipid would be further apart from each other, including acceptors, and FRET efficiency would decrease in a *non-specific* manner. A 25% increase in lipid area would justify the decrease in FRET efficiency for 0% l_o. This increase in membrane area might help explain previous observations of increase in membrane permeability after BA treatment [47,49].

The theoretical FRET efficiency expected for a homogeneous lipid mixture (0.60) is not observed at 100% l_o, a phenomena previously observed [74,75]. The likely reason for this behaviour is that Rho-DOPE, the acceptor, aggregates in the l_o phase, leading to the formation of Rho-DOPE clusters. The formation of these clusters would decrease the probability of FRET

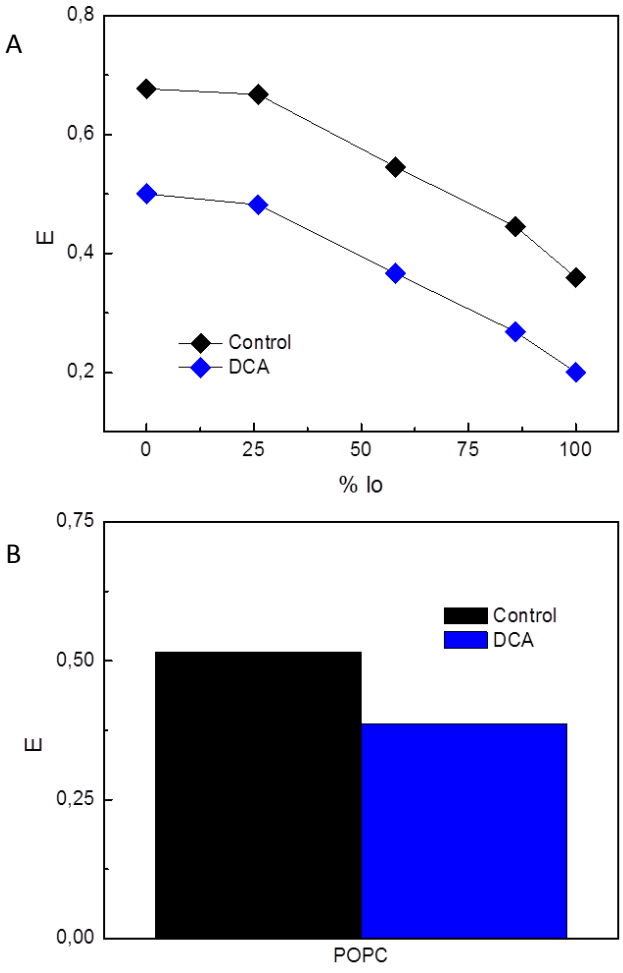

Figure 3-31 - FRET efficiencies for various l_o proportions incubated in the absence (control) or in the presence of 500 µM of DCA. Liposome composition followed a tie-line described in the ternary phase diagram for POPC:Chol:PSM (Figure 3-13, Table 3-4). NBD-DPPE or NBD-DPPE and Rho-DOPE labelled liposomes were excited at 480 and fluorescence emission was recovered at 530nm (A) or between 460-530nm (B). FRET efficiencies were calculated according to Eq. 17

events due to a decrease in the fraction of donors with an acceptor in their vicinity.

Surprisingly, a change in FRET efficiency is also observed at 100% l_o, suggesting an interaction between BAs and the membrane. However, in the l_o, phase the FRET model is no longer able to explain the data (even in the absence of BAs), as significantly larger FRET efficiencies are expected. As already discussed, Rho-DOPE is heavily clustered and acceptor densities can no longer be determined assuming a homogeneous distribution of membrane components. In these conditions, the observed effects could also be induced by acceptor extraction. Given that all data points to an absence of BA partition to the l_o phase, an artefact associated with acceptor distribution is likely to be responsible for the FRET decrease at high l_o content.

To discard an effect induced by DCA at 100% l_o, DPH anisotropy in a 100% l_o liposome was measured. The mixture was then heated to induce a change the lipid phase, from l_o to l_d. With heating, lipids in the system gain energy, the ordered phase cannot be maintained and domains of l_d phase start to form [81].

No change in DPH anisotropy at room temperature (only l_o phase formed) was measured (Figure 3-32). Additionally, when liposomes are heated to 55°C (disruption of l_o, formation of some l_d), DCA induced a decrease in the fluorescence anisotropy of DPH. This is consistent with previous results and further shows that DCA can affect l_d phases with different compositions and is inert for different l_o compositions. Liposomes were then cooled down to 35°C, to test the reversibility of the effect. DPH fluorescence anisotropy returns to values (Figure 3-32) obtained before, indicating a loss of effect, due to the formation of the l_o phase. This confirms that the phenomena observed is reversible and is an additional confirmation that the effect of DCA is not associated with a removal of Chol from the membrane, as this process would not be expected to

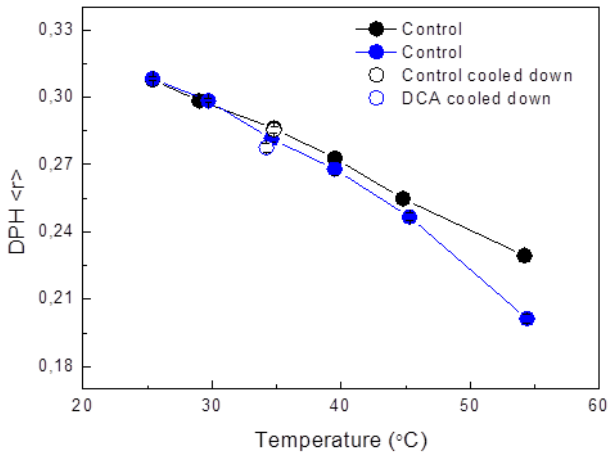

Figure 3-32 - DPH fluorescence anisotropy as a function of temperature. DPH labelled liposomes were incubated in the absence (black circles) or presence of 500 µM of DCA (blue circles). Liposomes were composed of 25.4:39.8:34.8 POPC:Chol:PSM (mol/mol/mol) so as to form only the l_o phase at room temperature. Liposomes were heated to different temperatures and fluorescence anisotropy was measured. After 55°C (closed circles), liposomes were cooled down back to 35°C (open circles). Probe/lipid ratio was 1/200.

be reversible.

To summarize, DCA appears to make l_d membranes insensitive to the presence of Chol. This effect is not mitigated by hydrophilic BAs and is not achieved through the removal of Chol from lipid membranes. Also, it is not observed for different l_o rich-membranes. This effect cannot be associated only with a decrease in l_o domain formation, since it is observed at Chol concentrations for which the l_o phase is not formed. In this way, the adsorption of DCA to l_d membranes directly inhibits the rigidification effect of Chol on the bilayer. However, upon l_o formation this inhibition is no longer observed, possibly due to a significant loss of DCA in the membrane, as determined for the fluorescent labelled BAs partition.

3.4.Bile acid effect on live HEK293 cells

To conclude this thesis, some experiments were conducted on live HEK293 cells. The only criteria for choosing this cell line was the simplicity of culture. The susceptibility of the cell line to apoptosis was secondary, and the focus was on the direct effect of BAs on the lipid membrane.

Two experiments were conducted with this cell line.

Firstly, cells were incubated with DCA-NBD and UDCA-NBD for 30min and fluorescence intensity and location was assessed under the microscope. DCA-NBD distribution was also evaluated after HEK293 cells were pre-incubated with 100 µM TUDCA for 30min.

Both DCA-NBD and UDCA-NBD fluorescence was localized almost everywhere in the cell, except for the nucleus (Figure 3-33). These labelled BA are probably traversing the membrane and partitioning to every membrane in the cell. The fluorescence distribution of DCA-NBD was unaffected by TUDCA pre-incubation (Figure 3-33).

Having seen that labelled BAs distribute equally on HEK293 cells, the effects of unlabelled BA were studied using ANEPPDHQ as a membrane probe. Cells were incubated with the membrane probe for 30min, followed by 30min incubation with either 50 or 100 µM of TUDCA or DCA. Cells incubated with 100 µM of TUDCA were incubated for another 30min with 50 µM of DCA. ANEPPDHQ lifetime was measured using FLIM.

Surprisingly ANEPPDHQ lifetime decreased when BAs were added to HEK293 cells (Figure 3-34). This is in contradiction to our previous results in model systems, when an increase in ANEPPDHQ lifetime was observed (Figure 3-24). However, previous results were obtained using only POPC liposomes. Importantly, even for the control experiment, where no BA was added, ANEPPDHQ lifetime was larger than in control experiment using POPC vesicles. When DCA was added after TUDCA, the decrease in lifetime was not so pronounced. A decrease in ANEPPDHQ lifetime would probably mean the probe is more exposed to the solvent, suggesting a higher degree of membrane hydration.

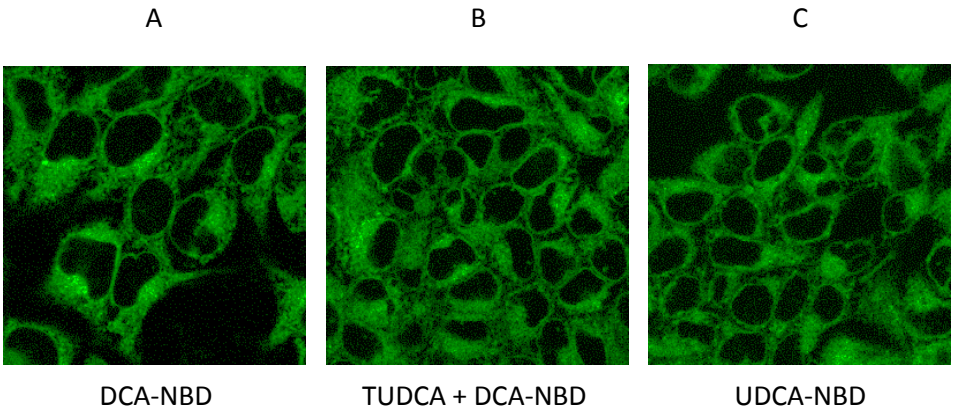

Figure 3-33 - Location of labelled BA on HEK293 cells. HEK293 cells were incubated for 30min with 10 µM of labelled BAs, followed by a 30min preincubation with 100 µM TUDCA in the case of TUDCA+DCA-NBD. Cells were imaged on confocal microscope using NBD fluorescence.

ANEPPDHQ is labelling every cellular membrane and the obtained fluorescence decay is the sum of individual decays from all the cellular membranes: plasma membrane, Golgi reticulum, nucleus, etc. Taking into account the partition behaviour observed for fluorescently labelled BAs, it is highly likely that BAs bind differently to the membrane of each organelle depending on the Chol content. In this case, the effect of BAs on membrane structure might change significantly from organelle to organelle. As such, in order to correctly interpret data from living cells, a more detailed analysis is required to quantify the effects of BAs in the membrane of each organelle individually.

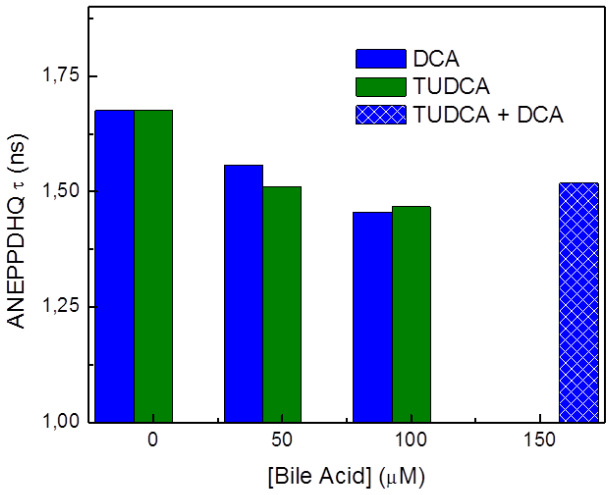

Figure 3-34 - ANEPPDHQ fluorescence lifetimes as a function of added BA. HEK293 cells labelled with 10 µM of ANEPPDHQ were incubated with 50 or 100 µM of DCA or TUDCA for 30min. Additionally, a co-incubation was performed with 100 µM TUDCA + 50 µM DCA for 30+30min. ANEPPDHQ was imaged using FLIM, to recover fluorescence decays.

4. Discussion

Firstly, labelled BAs can detect micelles formed by unlabelled BAs. CMC values recovered with BA-NBD were in range of values previously described in the literature. BA-NBD probes demonstrated high affinity for BA aggregates.

Both DCA-NBD and UDCA-NBD aggregate at submicellar concentrations, and both prefer to form homodimers but can also interact with unlabelled BAs. The recovered equilibrium constants for DCA-NBD interaction with different BAs can be considered as the upper bounds for DCA interaction with the same BAs, since unlabelled BAs experience electrostatic repulsion which is absent for DCA-NBD containing aggregates. Still, even considering these upper bounds for the efficiency of DCA interaction with hydrophilic BAs, incubation with hydrophilic BAs is not expected to change the fraction of aggregated DCA in a dramatic manner. These results allow us to discard the solubilisation of DCA as a possible mechanism through which hydrophilic BAs could exert a cytoprotective effect.

Secondly, labelled BA partition was assessed and observed to be dependent on the level of order in the membrane. The difference between membrane partition efficiencies observed for hydrophobic and hydrophilic BAs is significant and on the cholesterol-rich plasma membrane is expected to result in a different effective concentrations of these two species. It is possible that this could dictate the apoptotic potential of hydrophobic BAs and the absence of the effect with hydrophilic BAs. As discussed before, the labelling of DCA and UDCA with NBD, removing the carboxylic acid, might generate a molecule more favourable to partition to lipid membranes. For the negatively charged BAs, partition to lipid membranes at high densities might be severely hindered due to increases in membrane surface charge.

Other results also show that the cytoprotective role of hydrophilic BA is not achieved through the prevention of hydrophobic BA partition. The partition of DCA-NBD to lipid membranes was completely insensitive to UDCA incubation, and although high densities of unlabelled UDCA and TUDCA at the membrane might interfere significantly with DCA partition given the resulting increase of membrane surface charge, we observed that these hydrophilic BAs were not able to inhibit the effects of DCA on the membrane structure (as seen for membrane fluorescent probes), even at very high concentrations. Partition results for the derivatized BAs with liquid ordered membranes clearly indicate that UDCA-NBD was significantly less prone for membrane interaction when compared with DCA-NBD in such membrane environments. This lower membrane partition observed for hydrophilic BAs might help explain why UDCA and TUDCA were unable to inhibit DCA partition and ultimately could be the reason why these molecules are generally not inducers of apoptosis. As such, the hypothesis of a shield of UDCA and TUDCA over the membranes as the basis for its cytoprotective effect is rejected.

Finally, the results obtained with membrane probes clearly showed that BAs interact with lipid membranes. This interaction is superficial as ANEPPDHQ and TMA-DPH are sensitive to it, while DPH, which probes the membrane interior, is much less sensitive to the presence of BAs. In this way, BAs bind lipid membranes mostly through adsorption rather than incorporation in acyl-chains as previously suggested [47,48,51].

Another important result is that unlabelled BAs are aggregated when added to preformed liposomes, and this aggregation is likely preventing membrane partition of BAs to model membranes. As already discussed, the presence of a large concentration of proteins and different membrane components *in vivo* would contribute to solubilize these aggregates, and effective partition to membranes is in this way achieved.

Interaction of hydrophobic BAs with lipid membranes in the liquid disordered phase resulted in a significant increase in membrane surface area, indicative of significant partition of BAs to the membrane. This effect might be related to changes in membrane permeability observed after incubation of both isolated mitochondria and model membranes with hydrophobic BAs [47,48].

Surprisingly, DCA was able to disrupt to some extent the ordering of the membrane by Chol. This property was particularly strong at low Chol concentrations, corresponding to no or low fractions of l_o phase. At higher Chol content, when l_o comprises most of the membrane area, the ability of DCA to disorder the membrane was significantly reduced. Taking into account the partition behaviour of fluorescently labelled BAs, it can be concluded that the absence of effects on the l_o phase is due to an absence of membrane binding by BAs to l_o membranes. In this way, it is possible that the apoptotic effect of BAs could also be achieved through changes in membrane structure or modulation of membrane composition. As discussed before, lipid rafts are essential checkpoints for apoptotic signalling [21,26] and disturbance of this homeostasis, for example caused by Chol deprivation, can lead to apoptosis [19,45].

Also, a recent paper reported that the oligomerization of Bax in model membrane systems was dependent on its fluidity, increasing the Chol content of the membrane inhibited Bax insertion [82]. One possible mechanism of DCA-induced apoptosis can be the prevention of mitochondrial membrane rigidification, rendering it susceptible to Bax oligomerizatio and further damage.

Importantly, the effect of DCA on order of Chol containing membranes could not be countered by co-incubation with hydrophilic BAs. In fact, these molecules also induced some degree of disordering in Chol containing membranes, albeit a much smaller one than DCA. The coincubation of lipid membranes with both hydrophobic and hydrophilic BAs resulted in a cumulative effect on the membrane order. As already discussed, it is likely that the reason why hydrophilic BAs are not apoptotic in hepatocytes while DCA is strongly apoptotic, at the same concentrations, is associated with differential affinities for lipid membranes for the two classes of BAs. Conversely, the cytoprotective role of hydrophilic BAs might not be related to the direct modulation of membrane structure, and cytoprotection could be achieved through direct activation of a survival signal [28,33,83].

In summary, the mechanism through which hydrophilic BAs prevent activation of apoptosis of hydrophobic BAs is neither the formation of BA complexes in solution, prevention of hydrophobic BA partition to membranes, nor the inhibition of membrane perturbations by hydrophobic BAs. However, it is shown here that hydrophobic BAs might act by modifying

membrane structure and/or increasing permeability. Possibly, the effects of hydrophobic BAs on the plasma membrane could result in changes in membrane raft composition.

Future work devoted to this topic will pursue the effect of BAs on the mitochondrial membrane. Partition studies as well as probing for changes in mitochondrial membrane biophysical properties will be conducted in order to elucidate the effect of BAs on mitochondrial stress. Also, the effect of BAs on membranes *in vivo* will be the subject of a more in-depth study.

In Figure 4-1 a cartoon depicts DCA interacting with a lipid membrane consisting of a l_o domain in a l_d matrix. The BAs partition to the l_d phase expanding, increase the area it occupies.

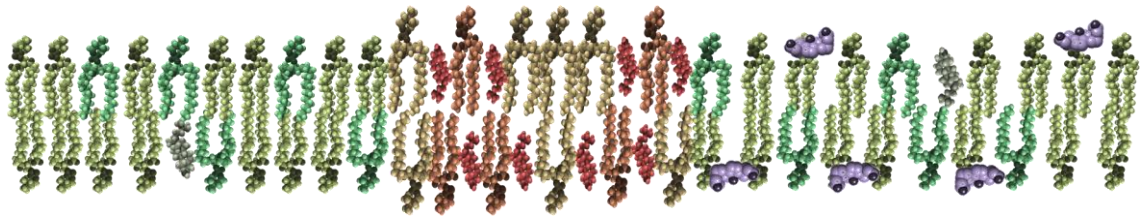

Figure 4-1 - Cartoon depicting DCA interactions with a generic lipid membrane with l_o and l_d phase coexistence. l_d and l_o phases are shown in green and red tones, respectively. DCA (purple) exhibits a superficial location in the membrane after binding and partitions preferably to the l_d phase. Additionally, the l_d phase to which DCA partitions to is expanded due to interaction with the hydrophobic BA.

5. References

[1] D.M. Heuman, Quantitative estimation of the hydrophilic-hydrophobic balance of mixed bile salt solutions, Journal of Lipid Research. 30 (1989) 719–30.

[2] A.F. Hofmann, L.R. Hagey, Bile acids: chemistry, pathochemistry, biology, pathobiology, and therapeutics, Cellular and Molecular Life Sciences. 65 (2008) 2461–2483.

[3] A.F. Hofmann, A. Roda, Physicochemical properties of bile acids and their relationship to biological properties: an overview of the problem, Journal of Lipid Research. 25 (1984) 1477–89.

[4] M.J. Monte, J.J.G. Marin, A. Antelo, J. Vazquez-Tato, Bile acids: chemistry, physiology, and pathophysiology, World Journal of Gastroenterology. 15 (2009) 804–16.

[5] L. Maillette de Buy Wenniger, U. Beuers, Bile salts and cholestasis, Digestive and Liver Disease. 42 (2010) 409–18.

[6] K. Matsuoka, M. Suzuki, C. Honda, K. Endo, Y. Moroi, Micellization of conjugated chenodeoxy- and ursodeoxycholates and solubilization of cholesterol into their micelles: comparison with other four conjugated bile salts species, Chemistry and Physics of Lipids. 139 (2006) 1–10.

[7] A. Roda, A. Minutello, M.A. Angellotti, A. Fini, Bile acid structure-activity relationship: evaluation of bile acid lipophilicity using 1-octanol/water partition coefficient and reverse phase HPLC, Journal of Lipid Research. 31 (1990) 1433–43.

[8] D. Madenci, S.U. Egelhaaf, Self-assembly in aqueous bile salt solutions, Current Opinion in Colloid & Interface Science. 15 (2010) 109–115.

[9] N. Funasaki, M. Nomura, S. Ishikawa, S. Neya, Hydrophobic self-association of sodium taurochenodeoxycholate and tauroursodeoxycholate, The Journal of Physical Chemistry B. 104 (2000) 7745–7751.

[10] K. Matsuoka, Y. Moroi, Micelle formation of sodium deoxycholate and sodium ursodeoxycholate (part 1), Biochimica Et Biophysica Acta. 1580 (2002) 189–99.

[11] S. Reis, C.G. Moutinho, C. Matos, B. de Castro, P. Gameiro, J.L.F.C. Lima, Noninvasive methods to determine the critical micelle concentration of some bile acid salts, Analytical Biochemistry. 334 (2004) 117–26.

[12] P. Garidel, A. Hildebrand, R. Neubert, A. Blume, Thermodynamic characterization of bile salt aggregation isothermal titration calorimetry, Langmuir. 16 (2000) 5267–5275.

[13] A. Roda, A.F. Hofmann, K.J. Mysels, The influence of bile salt structure on self-association in aqueous solutions, The Journal of Biological Chemistry. 258 (1983) 6362–70.

[14] N.A. Mazer, M.C. Carey, R.F. Kwasnick, G.B. Benedek, Quasielastic light scattering studies of aqueous biliary lipid systems. Size, shape, and thermodynamics of bile salt micelles, Biochemistry. 18 (1979) 3064–75.

[15] F. Lopez, J. Samseth, K. Mortensen, Micro- and macrostructural studies of sodium deoxycholate micellar complexes in aqueous solutions, Langmuir. 12 (1996) 6188–6198.

[16] A. Campanelli, S. de Sanctis, E. Giglio, N. Pavel, C. Quagliata, From crystal to micelle: a new approach to the micellar structure, Journal of Inclusion Phenomena and Molecular Recognition in Chemistry. 7 (1989) 391–400.

[17] A. Coello, F. Meijide, E.R. Núñez, J.V. Tato, Aggregation behavior of bile salts in aqueous solution, Journal of Pharmaceutical Sciences. 85 (1996) 9–15.

[18] T. Patel, S.F. Bronk, G.J. Gores, Increases of intracellular magnesium promote glycodeoxycholate-induced apoptosis in rat hepatocytes, The Journal of Clinical Investigation. 94 (1994) 2183–92.

[19] A. Garcia, X. Cayla, A. Fleischer, J. Guergnon, F. Alvarez-Franco Cañas, M.P. Rebollo, et al., Rafts: a simple way to control apoptosis by subcellular redistribution, Biochimie. 85 (2003) 727–731.

[20] J.D. Amaral, R.E. Castro, C.J. Steer, C.M.P. Rodrigues, p53 and the regulation of hepatocyte apoptosis: implications for disease pathogenesis, Trends in Molecular Medicine. 15 (2009) 531–41.

[21] K.S. George, S. Wu, Lipid raft: a floating island of death or survival, Toxicology and Applied Pharmacology. 259 (2012) 311–9.

[22] J.D. Amaral, R.J.S. Viana, R.M. Ramalho, C.J. Steer, C.M.P. Rodrigues, Bile acids: regulation of apoptosis by ursodeoxycholic acid, Journal of Lipid Research. 50 (2009) 1721–34.

[23] R.E. Castro, J.D. Amaral, S. Solá, B.T. Kren, C.J. Steer, C.M.P. Rodrigues, Differential regulation of cyclin D1 and cell death by bile acids in primary rat hepatocytes, American Journal of Physiology. Gastrointestinal and Liver Physiology. 293 (2007) G327–34.

[24] C.M.P. Rodrigues, G. Fan, X. Ma, B.T. Kren, C.J. Steer, A novel role for ursodeoxycholic acid in inhibiting apoptosis by modulating mitochondrial membrane perturbation, The Journal of Clinical Investigation. 101 (1998) 2790–9.

[25] C.M.P. Rodrigues, S. Solá, J.C. Sharpe, J.J.G. Moura, C.J. Steer, Tauroursodeoxycholic acid prevents Bax-induced membrane perturbation and cytochrome C release in isolated mitochondria, Biochemistry. 42 (2003) 3070–80.

[26] M.E. Peter, P.H. Krammer, The CD95(APO-1/Fas) DISC and beyond, Cell Death and Differentiation. 10 (2003) 26–35.

[27] M.B. Jarpe, C. Widmann, C. Knall, T.K. Schlesinger, S. Gibson, T. Yujiri, et al., Anti-apoptotic versus pro-apoptotic signal transduction: checkpoints and stop signs along the road to death, Oncogene. 17 (1998) 1475–82.

[28] C. Rust, L.M. Karnitz, C.V. Paya, J. Moscat, R.D. Simari, G.J. Gores, The bile acid taurochenodeoxycholate activates a phosphatidylinositol 3-kinase-dependent survival signaling cascade, The Journal of Biological Chemistry. 275 (2000) 20210–6.

[29] W.A. Faubion, M.E. Guicciardi, H. Miyoshi, S.F. Bronk, P.J. Roberts, P.A. Svingen, et al., Toxic bile salts induce rodent hepatocyte apoptosis via direct activation of Fas, The Journal of Clinical Investigation. 103 (1999) 137–45.

[30] C.M.P. Rodrigues, G. Fan, P.Y. Wong, B.T. Kren, C.J. Steer, Ursodeoxycholic acid may inhibit deoxycholic acid-induced apoptosis by modulating mitochondrial transmembrane potential and reactive oxygen species production, Molecular Medicine. 4 (1998) 165–78.

[31] J.D. Amaral, R.E. Castro, S. Solá, C.J. Steer, C.M.P. Rodrigues, p53 is a key molecular target of ursodeoxycholic acid in regulating apoptosis, The Journal of Biological Chemistry. 282 (2007) 34250–9.

[32] F. Azzaroli, W. Mehal, C.J. Soroka, L. Wang, J. Lee, N. Crispe, et al., Ursodeoxycholic acid diminishes Fas-ligand-induced apoptosis in mouse hepatocytes, Hepatology. 36 (2002) 49–54.

[33] M.H. Schoemaker, L. Conde de la Rosa, M. Buist-Homan, T.E. Vrenken, R. Havinga, K. Poelstra, et al., Tauroursodeoxycholic acid protects rat hepatocytes from bile acid-induced apoptosis via activation of survival pathways, Hepatology. 39 (2004) 1563–73.

[34] S. Solá, J.D. Amaral, R.E. Castro, R.M. Ramalho, P.M. Borralho, B.T. Kren, et al., Nuclear translocation of UDCA by the glucocorticoid receptor is required to reduce TGF-beta1-induced apoptosis in rat hepatocytes, Hepatology. 42 (2005) 925–34.

[35] S. Solá, R.E. Castro, B.T. Kren, C.J. Steer, C.M.P. Rodrigues, Modulation of nuclear steroid receptors by ursodeoxycholic acid inhibits TGF-b1-induced E2F-1/p53-mediated apoptosis of rat hepatocytes, Biochemistry. 43 (2004) 8429–8438.

[36] S. Solá, X. Ma, R.E. Castro, B.T. Kren, C.J. Steer, C.M.P. Rodrigues, Ursodeoxycholic acid modulates E2F-1 and p53 expression through a caspase-independent mechanism in transforming growth factor beta1-induced apoptosis of rat hepatocytes, The Journal of Biological Chemistry. 278 (2003) 48831–8.

[37] Q. Xie, V.I. Khaoustov, C.C. Chung, J. Sohn, B. Krishnan, D.E. Lewis, et al., Effect of tauroursodeoxycholic acid on endoplasmic reticulum stress-induced caspase-12 activation, Hepatology. 36 (2002) 592–601.

[38] L.J. Pike, Lipid rafts: heterogeneity on the high seas, The Biochemical Journal. 378 (2004) 281–92.

[39] A.-O. Hueber, A.-M. Bernard, Z. Herincs, A. Couzinet, H.-T. He, An essential role for membrane rafts in the initiation of Fas/CD95-triggered cell death in mouse thymocytes, EMBO Reports. 3 (2002) 190–6.

[40] H. Grassmé, A. Jekle, A. Riehle, H. Schwarz, J. Berger, K. Sandhoff, et al., CD95 signaling via ceramide-rich membrane rafts, The Journal of Biological Chemistry. 276 (2001) 20589–20596.

[41] C. Gajate, E. Del Canto-Jañez, A.U. Acuña, F. Amat-Guerri, E. Geijo, A.M. Santos-Beneit, et al., Intracellular triggering of Fas aggregation and recruitment of apoptotic molecules into Fas-enriched rafts in selective tumor cell apoptosis, The Journal of Experimental Medicine. 200 (2004) 353–65.

[42] C. Gajate, F. Gonzalez-Camacho, F. Mollinedo, Involvement of raft aggregates enriched in Fas/CD95 death-inducing signaling complex in the antileukemic action of edelfosine in Jurkat cells, PloS One. 4 (2009) e5044.

[43] E. Janas, R. Priest, J.I. Wilde, J.H. White, R. Malhotra, Rituxan (anti-CD20 antibody)-induced translocation of CD20 into lipid rafts is crucial for calcium influx and apoptosis, Clinical and Experimental Immunology. 139 (2005) 439–46.

[44] Y. Renaudineau, S. Nédellec, C. Berthou, P.M. Lydyard, P. Youinou, J.-O. Pers, Role of B-cell antigen receptor-associated molecules and lipid rafts in CD5-induced apoptosis of B CLL cells, Leukemia. 19 (2005) 223–9.

[45] R. Gniadecki, Depletion of membrane cholesterol causes ligand-independent activation of Fas and apoptosis, Biochemical and Biophysical Research Communications. 320 (2004) 165–9.

[46] D.M. Heuman, R.S. Bajaj, Q. Lin, Adsorption of mixtures of bile salt taurine conjugates to lecithin-cholesterol membranes: implications for bile salt toxicity and cytoprotection, Journal of Lipid Research. 37 (1996) 562–73.

[47] S. Güldütuna, B. Deisinger, A. Weiss, H.J. Freisleben, G. Zimmer, P. Sipos, et al., Ursodeoxycholate stabilizes phospholipid-rich membranes and mimics the effect of cholesterol: investigations on large unilamellar vesicles, Biochimica Et Biophysica Acta. 1326 (1997) 265–74.

[48] S. Güldütuna, G. Zimmer, M. Leuschner, S. Bhatti, A. Elze, B. Deisinger, et al., The effect of bile salts and calcium on isolated rat liver mitochondria, Biochimica Et Biophysica Acta. 1453 (1999) 396–406.

[49] J. Halin, P. Mattjus, Effects of bile salts on glucosylceramide containing membranes, Biochimica Et Biophysica Acta. 1808 (2011) 2886–93.

[50] A. Ben Mouaz, M. Lindheimer, J.C. Montet, J. Zajac, S. Lagerge, A study of the adsorption of bile salts onto model lecithin membranes, Colloids and Surfaces. B: Biointerfaces. 20 (2001) 119–127.

[51] F. Ollila, J.P. Slotte, A thermodynamic study of bile salt interactions with phosphatidylcholine and sphingomyelin unilamellar vesicles, Langmuir. 17 (2001) 2835–2840.

[52] G. Sugihara, T. Hirashima, S. Lee, H. Takiguchi, Y. Sasaki, The adsorption behavior of four bile salt species on cholesterol crystals in water - in connection with cholesterol solubilization, Colloids and Surfaces B: Biointerfaces. 5 (1995) 63–73.

[53] Y. Zhou, R. Doyen, L.M. Lichtenberger, The role of membrane cholesterol in determining bile acid cytotoxicity and cytoprotection of ursodeoxycholic acid., Biochimica Et Biophysica Acta. 1788 (2009) 507–13.

[54] S. Jean-Louis, S. Akare, M.A. Ali, E.A. Mash, E. Meuillet, J.D. Martinez, Deoxycholic acid induces intracellular signaling through membrane perturbations, The Journal of Biological Chemistry. 281 (2006) 14948–60.

[55] S. Akare, J.D. Martinez, Bile acid induces hydrophobicity-dependent membrane alterations, Biochimica Et Biophysical Acta. 1735 (2005) 59–67.

[56] M.J. Sarmento, M. Prieto, F. Fernandes, Reorganization of lipid domain distribution in giant unilamellar vesicles upon immobilization with different membrane tethers, Biochimica Et Biophysica Acta. 1818 (2012) 2605–2615.

[57] R.P. Haugland, Molecular Probes Handbook, a guide to fluorescent probes and labeling technologies, 11th Editi, Molecular Probes, Oregon, USA, 2010.

[58] S.N. Pinto, L.C. Silva, R.F.M. de Almeida, M. Prieto, Membrane domain formation, interdigitation, and morphological alterations induced by the very long chain asymmetric C24:1 ceramide, Biophysical Journal. 95 (2008) 2867–79.

[59] M.I. Angeloval, S. Soloéau, P. Méléard, J.E. Faucon, P. Bothorel, Preparation of giant vesicles by external AC electric fields. Kinetics and applications, Progress in Colloind and Polymer Science. 131 (1992) 127–131.

[60] C.W. McClare, An accurate and convenient organic phosphorus assay, Analytical Biochemistry. 39 (1971) 527–530.

[61] J.R. Lakowicz, Principles of Fluorescence Spectroscopy, Third Edit, Springer, New York, USA, 2006.

[62] M.M. Puchalski, M.J. Morra, R. von Wandruszka, Assessment of inner filter effect corrections in fluorimetry, Fresenius Journal of Analytical Chemistry. 340 (1991) 341–344.

[63] D.W. Marquardt, An algorithm for least-squares estimation of nonlienar parameters, Journal of the Society for Industrial and Applied Mathematics. 11 (1963) 431–441.

[64] N. Santos, M. Prieto, M.A.R.B. Castanho, Quantifying molecular partition into model systems of biomembranes: an emphasis on optical spectroscopic methods, Biochimica Et Biophysica Acta. 1612 (2003) 123–135.

[65] C. Boucheny, G.-P. Bonneau, J. Droulez, G. Thibault, S. Ploix, A perceptive evaluation of volume rendering techniques, ACM Transactions on Applied Perception. 5 (2009) 1–24.

[66] M.J. Moreno, M. Bastos, A. Velazquez-Campoy, Partition of amphiphilic molecules to lipid bilayers by isothermal titration calorimetry, Analytical Biochemistry. 399 (2010) 44–47.

[67] S. Mazères, V. Schram, J.F. Tocanne, A. Lopez, 7-nitrobenz-2-oxa-1,3-diazole-4-yl-labeled phospholipids in lipid membranes: differences in fluorescence behavior, Biophysical Journal. 71 (1996) 327–35.

[68] R.F.M. de Almeida, A. Fedorov, M. Prieto, Sphingomyelin/phosphatidylcholine/cholesterol phase diagram: boundaries and composition of lipid rafts, Biophysical Journal. 85 (2003) 2406–16.

[69] M.A.R.B. Castanho, M.X. Fernandes, Lipid membrane-induced optimization for ligand-receptor docking: recent tools and insights for the “membrane catalysis” model, European Biophysics Journal. 35 (2006) 92–103.

[70] K. Kinosita, A. Ikegami, S. Kawato, On the wobbling-in-cone analysis of fluorescence anisotropy decay, Biophysical Journal. 37 (1982) 461–4.

[71] T. Araiso, T. Koyama, Fluidity of glycerol skeletal region in phospholipid bilayers: a time-resolved fluorescence depolarization study, Japanese Journal of Physiology. 45 (1995) 187–96.

[72] L. Jin, A.C. Millard, J.P. Wuskell, X. Dong, D. Wu, H. a Clark, et al., Characterization and application of a new optical probe for membrane lipid domains, Biophysical Journal. 90 (2006) 2563–75.

[73] A.L. Obaid, L.M. Loew, J.P. Wuskell, B.M. Salzberg, Novel naphthylstyryl-pyridium potentiometric dyes offer advantages for neural network analysis, Journal of Neuroscience Methods. 134 (2004) 179–90.

[74] R.F.M. de Almeida, L.M.S. Loura, A. Fedorov, M. Prieto, Lipid rafts have different sizes depending on membrane composition: a time-resolved fluorescence resonance energy transfer study, Journal of Molecular Biology. 346 (2005) 1109–20.

[75] L.C. Silva, R.F.M. de Almeida, B.M. Castro, A. Fedorov, M. Prieto, Ceramide-domain formation and collapse in lipid rafts: membrane reorganization by an apoptotic lipid, Biophysical Journal. 92 (2007) 502–16.

[76] L. Silva, R.F.M. de Almeida, A. Fedorov, A.P.A. Matos, M. Prieto, Ceramide-platform formation and -induced biophysical changes in a fluid phospholipid membrane, Molecular Membrane Biology. 23 (2006) 137–48.

[77] D. Wüstner, Fluorescent sterols as tools in membrane biophysics and cell biology, Chemistry and Physics of Lipids. 146 (2007) 1–25.

[78] A.L. McIntosh, B.P. Atshaves, H. Huang, A.M. Gallegos, A.B. Kier, F. Schroeder, Fluorescence techniques using dehydroergosterol to study cholesterol trafficking, Lipids. 43 (2008) 1185–208.

[79] L.M. Loura, M. Prieto, Dehydroergosterol structural organization in aqueous medium and in a model system of membranes, Biophysical Journal. 72 (1997) 2226–36.

[80] L.M. Loura, A. Fedorov, M. Prieto, Exclusion of a cholesterol analog from the cholesterol-rich phase in model membranes, Biochimica Et Biophysica Acta. 1511 (2001) 236–43.

[81] R.F.M. de Almeida, M.A. Hink, J.W. Borst, M. Prieto, A.J.W.G. Visser, Lipid domains and rafts studied by time-resolved fluorescence microspectroscopy, in: A. Pramanik (Ed.), Biochemistry and Biophysics of Lipids, Transworld Reaserch Network, Kerala, India, 2006: pp. 31–62.

[82] S. Lucken-Ardjomande, S. Montessuit, J.-C. Martinou, Bax activation and stress-induced apoptosis delayed by the accumulation of cholesterol in mitochondrial membranes, Cell Death and Differentiationn. 15 (2008) 484–93.

[83] E.C. Torchia, A. Stolz, L.B. Agellon, Differential modulation of cellular death and survival pathways by conjugated bile acids, BMC Biochemistry. 2 (2001) 11–23.